SURFACE CHEMISTRY ON INTERACTION OF BIOMASS DERIVED OXYGENATES WITH HETEROGENEOUS CATALYST

A Dissertation
Presented to
The Academic Faculty

by

Jungseob So

In Partial Fulfillment
of the Requirements for the Degree
Doctor of Philosophy in the
School of Chemical & Biomolecular Engineering

Georgia Institute of Technology
May 2018

SURFACE CHEMISTRY ON INTERACTION OF BIOMASS DERIVED OXYGENATES WITH HETEROGENEOUS CATALYST

Approved by:

Dr. Carsten Sievers, Advisor
School of Chemical & Biomolecular Engineering
Georgia Institute of Technology

Dr. Yulin Deng
School of Chemical & Biomolecular Engineering
Georgia Institute of Technology

Dr. David S. Sholl, Advisor
School of Chemical & Biomolecular Engineering
Georgia Institute of Technology

Dr. Charles Liotta
[College of Chemistry and Biochemistry]
Georgia Institute of Technology

Dr. Carson Meredith
School of Chemical & Biomolecular Engineering
Georgia Institute of Technology

Date Approved: 12 14, 2017

To my mother, Hyunsook Choi

ACKNOWLEDGEMENTS

This dissertation means not only my work in the laboratory, but it is also a unique milestone in four and half years of research at Georgia Tech, specifically within the Sievers group and Sholl group. I would like to acknowledge that this work would not have been possible without the financial support from the Renewable Bioproducts Institute at the Georgia Institute of Technology for their funding through the Paper Science and Engineering. First and foremost, I must thank my advisor, Dr. Carsten Sievers, for his guidance and support throughout the time during the entire years as a graduate student. Dr. Sievers has aided me immeasurably in providing insight into my research and allowing me to grow as a research scientist, making my years here in graduate school forgettable. I also wish to express my special thanks to co-advisor, Dr. David Sholl for his intellectual support and encouragement. Under his guidance and advice, I could grow both personally and professionally. I would also like to thank my thesis committee members, Dr. Yuling Deng, Charles Liotta, and Carson Meredith. They are academically, and personally great people and always gave me fruitful advice for my research. During years at Georgia Tech, I also had the wonderful opportunity to collaborate with several renowned research group. I must thank Dr. Stavitsk at Brookhaven National lab for performing XANES experiment and intellectual contributions. I also must thank Will McDermott and Dr. Ive Hermans from the University of Wisconsin for the synthesis of material and fruitful discussion for the project of chapter 3.

Secondly, I would like to mention that the members of the Sievers and Sholl group have contributed immensely to my personal and professional time at Georgia Tech.

The group has been a source of friendships as well as good advice and collaboration. I want to give special acknowledgment to Dr. Gou Shiou Foo. He was a great mentor and friend with a sense of humor, who was an expert for many instruments so helping me through candidacy and for sharing his valuable wisdom. I also want to thank the rest of the group members for their support and encouragement. They are Chukwuemeka Okolie, Akil Syed, Sireesha Aluri, Alex Brittain, Jason Lee, and Lisa West. I must also thank an undergraduate researcher whose hard work increased the quality of the research that I was able to conduct, Yoona Chung.

Finally, I wish to recognize and thank my family for their unconditional support of all my aspirations. Especially, I thank my parents, Byunghyeok So, and Hyunsook Choi, incredible father, and mother who cultivated me based on love, hard work, and incomparable dedication. Without the love and support of my family, I would certainly not be where I am today.

Table of Contents

LIST OF TABLES

LIST OF FIGURES

LIST OF SYMBOLS AND ABBREVIATIONS

APR	aqueous phase reforming
ATR-IR	attenuated total reflectance infra-red spectroscopy
BAS	Brønsted acid site
BET	Brunauer-Emmett-Teller
BJH	Barett-Joyner-Halenda
boe	barrel of oil energy equivalent
CO_B	CO bridge bound to Pt
CO_L	CO linearly bound to Pt
DFT	density functional theory
FT-IR	Fourier transform infra-red spectroscopy
H*	dissociatively adsorbed hydrogen on Pt
HREELS	high resolution electron energy loss spectroscopy
HV	HV high vacuum
IR	IR infra-red

MAS NMR	magic angle spin nuclear magnetic resonance
MCT/A	mercury cadmium telluride antimonide
Mo BEA	dealuminated molybdenum zeolite beta
NMR	nuclear magnetic resonance
RTHV	room temperature and high vacuum
RTP	room temperature and pressure
Sn BEA	dealuminated tin zeolite beta
WGS	water-gas shift
W BEA	dealuminated tungsten zeolite beta
WGS	water-gas shift
XPS	x-ray photoelectron spectroscopy

SUMMARY

The discovery of crude oils in the 19th century and processed inexpensive fuels has contributed to the industrialization of the word and heavily lifted standard of living. However, the alarming about the finite nature and limited availability of fossil fuels has directed government, academy, and industry to focus on finding more sustainable replacements feedstock for transportation fuels and chemicals. Biomass is one of the most promising replacements as it can be grown sustainably, and when appropriately processed, energy and fuel can be produced in a carbon-neutral fashion. Heterogeneous catalysts, such as metal oxides, metals supported on metal oxides, aluminosilicates greatly contributed to oil refining and chemical production due to their high stability at harsh conditions, economic utilization relative to other chemical conversion methods. Thus, heterogeneous catalysts are also expected to be an integrated part of the catalytic upgrading of biomass in the future.

The development of effective and efficient processes in petrochemical refining is due to the design of catalyst based on an understanding of the relevant surface chemistry involved. Similarly, the discovery of catalysts for biomass upgrading should depend on an in-depth knowledge of how biomass molecules interact with heterogeneous catalyst surfaces. Investigating the interaction of biomass-derived feedstocks with heterogeneous catalysts is challenging due to their chemical compositions. As most biomass-derived molecules are highly oxygenated, they often have low vapor pressures and are soluble in polar solvents. Therefore, the process of biomass conversion into value-added products is highly likely to be conducted in the condensed phase. However, Most traditional surface

science techniques require dosing the molecule being investigated via gas phase and the use of ultra-high vacuum conditions. As a result, alternative methodologies must be developed to study the surface science of biomass-derived oxygenates on heterogeneous catalysts. The purpose of this dissertation is to understand the biomass-derived oxygenates surface chemistries using various IR spectroscopic techniques coupled with the probe molecules which has similar functionality to biomass-derived feedstocks to elucidate the reaction mechanisms and catalyst properties to be active for reactions.

First, we studied the effect of size and functionality of biomass-derived oxygenates on the formation of surface species on 5 wt% Pt/γ-Al_2O_3 in aqueous phase reforming (APR) reaction using in-situ ATR-IR spectroscopy. Specifically, kinetics of formation and conversion of linearly bound and bridging CO from glycerol, sorbitol, and glucose are studied at different temperatures. Regardless types of reactant, the formed COB from the decomposition of the reactants is more susceptible to WGS reaction, but increasing temperature from room temperature to 72 °C for APR reaction induced inactive CO_L to start to undergo oxidation via WGS reaction. Interestingly, the reforming of glucose exhibited significantly reduced conversion into CO surface species on Pt due to the steric effect in the presence of neighboring acyclic glucose. The unreacted portion of glucose readily converted into CO surface species when acyclic glucose near the Pt surface is absent. Also, compared to the fresh catalyst for reforming reaction of polyols and sugars, the second use of the catalyst when the temperature reached at high temperatures (72 °C) generated the formation of CO surface species. This phenomenon is highly likely to be related to the accumulation of unreacted portion surface intermediates decomposed from at the interface between Pt and alumina support.

The second study investigates how C2 oxygenates adsorb and reacts on heteroatom-doped zeolites in order to provide a tool (probe molecules: acetone and hydoroxyacetone) to find the characteristics of LA sites for C-C coupling of biomass-derived oxygenates and Meerwein−Ponndorf−Verley (MPV) 1,2 hydride shift for isomerization of sugars. We discovered that Sn BEA readily catalyzes acetone to form bigger oxygenates such as mesityl oxide via aldol condensation reaction. Low amount of acetone exclusively formed mesityl oxide due to the absence of neighboring acetone, which prevents mesityl oxide from further reacting with acetone to form C9 oxygenates including phorones, isophorones at low temperatures and aromatics and cokes at high temperatures. Hydroxyacetone, a carbonyl compound with an additional hydroxyl group at α-position was exclusively converted into 2-hydroxypropanal via 1, 2 hydride shift over Sn BEA without forming significant surface species, but exhibited the considerable binding strength to Sn sites up to 400 °C, resisting desorption. The presence of H_2O negatively affects the C-C coupling with H_2O. However, once the products were formed on the surface, H_2O promotes the desorption of products, preventing the deactivation of catalysts. Based on the surface studies, we propose the small amount of H_2O in alcohol solvent during C-C coupling during reforming of biomass-derived oxygenates would be beneficial for maintaining the activity of catalysts for biomass conversion. Also, the presence of H_2O promotes the formed 2-hydroxypropanal at active sites to further transform into acrolein. We also prepared Sn, Mo, and W BEA using a solid-state mixing method of the dealuminated beta zeolites to find the most influential parameter of Lewis acid sites among electro affinity, the Lewis acid hardness, and size of the metal site of the heteroatom-doped zeolites. The most prominent factor for the catalytic activity of the prepared catalysts is the size of metal

atoms, which presumably enables two functional groups of the oxygenates to bind to the active sites simultaneously.

Lastly, we studied the redox properties of α-MoO_3 in UHV conditions using acetone and acetaldehyde as probe molecule to elucidate the effect of alcohol solvent on the reaction pathway of biomass-derived oxygenates over α-MoO3. α-MoO_3 are known to have an activity for C-C bond cleavage of oxygenates via retro-aldol reactions in the condensed phase but easily tend to lose the activity for the reaction. We found that α-MoO_3 is a high activity for the decomposition of ethanol and acetaldehyde which are used as model compounds to mimic the functionalities of biomass-derived oxygenates but easily reduced by the depletion of surface O atoms of α-MoO_3 during the decomposition. IR spectroscopy and XANES revealed that the only surface of the catalysts was reduced and the reduced α-MoO_3 exhibited the different reaction path, instead of full decomposition into CO_2 due to the absence of O atoms on the surface.

Introduction

1.1 Biomass as a Sustainable Feedstock for Energy and Chemicals

Soaring demand for petroleum by developing countries, declining petroleum resources, and environmental concerns about ongoing dependency on fossil fuels have spurred efforts to create energy-efficient and sustainable processes to produce fuels and chemicals for future generations. In this respect, biomass is the only sustainable current source of organic carbon and biofuels.[1] With appropriate harvesting and processing biomass can have a nearly "closed carbon balance," thereby leaving a minimal global-warming footprint.[2] The U.S. Department of Agriculture and Oak Ridge National Laboratory reported that the USA has capacity to produce 1.3×10^9 metric tons of dry biomass per year, and this amount of biomass is equivalent of 3.8×10^9 barrels of oil by energy content.[3] The U.S. Department of Energy projected that processing 1.3 billion tons of biomass per year could replace 33% of U.S transportation fuel and 25% of all organic chemicals with non-food-interfering (lignocellulosic) biomass.[3]

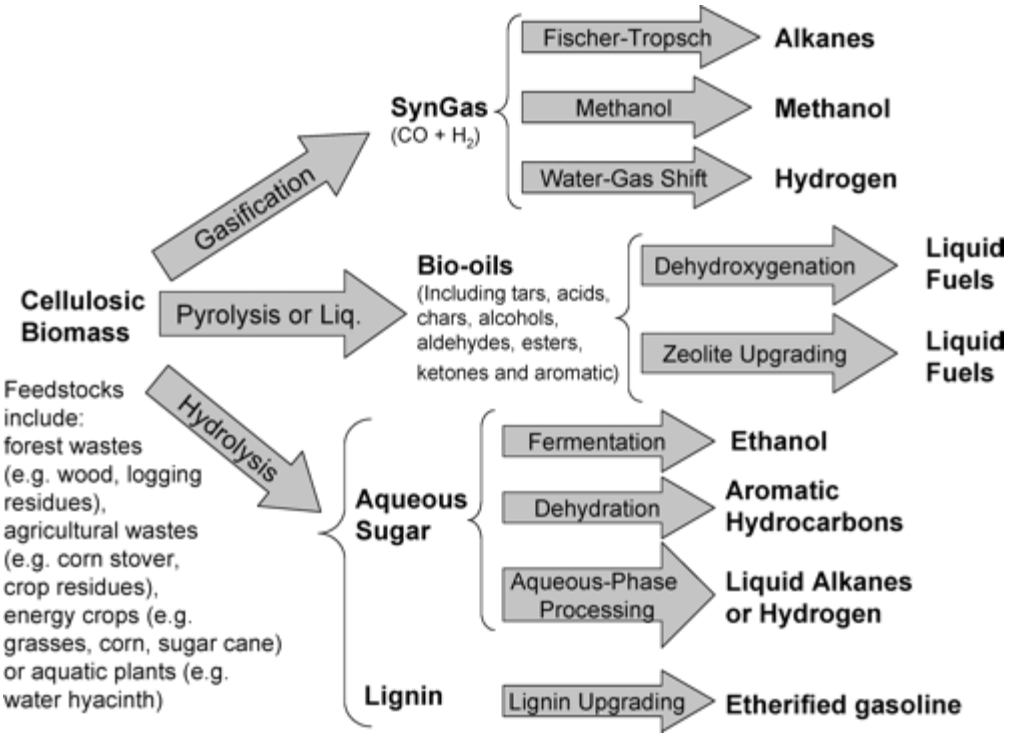

Figure 0.1. Strategies for production of fuels from lignocellulosic biomass. Figure reproduced from Huber et al.[4]

The current routes for biomass conversion to synthesize fuels and chemicals are broadly categorized into three groups shown in Figure 0.1. depending on the initial step for biomass breakdown, including syngas production by gasification, bio-oil production by pyrolysis or liquefaction, or hydrolysis of biomass to produce sugar monomer units.[1] Syngas can be further processed to alkanes via Fischer-Tropsch catalysis, methanol via methanol synthesis, or H_2 production via water gas shift reactions.[1, 5] The bio-oils from the pyrolysis can be further processed as a use of liquid fuels in HDO reaction over the zeolites.[1, 5] Also, aqueous sugar monomer units and associated lignin can be upgraded into the transportation fuels such as ethanol, diesel fuel, and gasoline.[1, 5]

Biodiesel and ethanol are currently on the market. In the U.S.A, automobiles run on fuels obtained by blending of gasoline and ethanol. Ethanol is currently produced by the process which consists of the enzymatic hydrolysis of corn starch to sugars and subsequent the fermentation of sugars by yeast to ethanol.[6] However, since the fermentation requires moderate temperature and acid conditions, the rate of ethanol production is slow. Furthermore, the distillation step following the fermentation is energy-intensive, which makes the entire process inefficient due to the high ratio of energy output to energy input. Current biodiesel production relies on the trans-esterification of waste triglyceride sources such as used cooking oils. Unfortunately, these sources are relatively limited in quantity. Vegetable oils such as coconut, palm kernel, soybean oil can be used to produce biodiesel, but this process creates ethical issues due to the competition of foodstuffs versus transportation fuels. Due to the limitations of ethanol and biodiesel for widespread utilization, lignocellulosic biomass should be considered as a source of future development of large-scale production of biofuels.

As seen in Figure 0.2, lignocellulosic biomass are polymers made up of carbohydrate monomers. Lignocellulosic biomass is the most abundant, cheapest and fast growing form of biomass and it consists of cellulose, hemicellulose and lignin[5]. Cellulose (10-25% of lignocellulose) is a crystalline polymer that consists of a linear polysaccharide with β-1,4 linkage of D-glucopyranose monomers. Hemicellulose (20-40% of lignocellulose) is amorphous and comprised of five-carbon sugars (xylose and arabinose) and six-carbon sugars (galactose, glucose, and mannose). Lignin (10-25% of lignocellulose) is a highly branched amorphous polymer, which consists of hetero-substituted aromatic monomers and exists in the cell walls of certain biomass[1]. Since this

"woody" biomass is not considered as a foodsource, many ethical issues about using crops for industrial purposes instead of agricultural use can be avoided. As a result, lignocellulosic biomass is an ideal candidate as a chemical and energy feedstock to replace the petroleum counterparts.

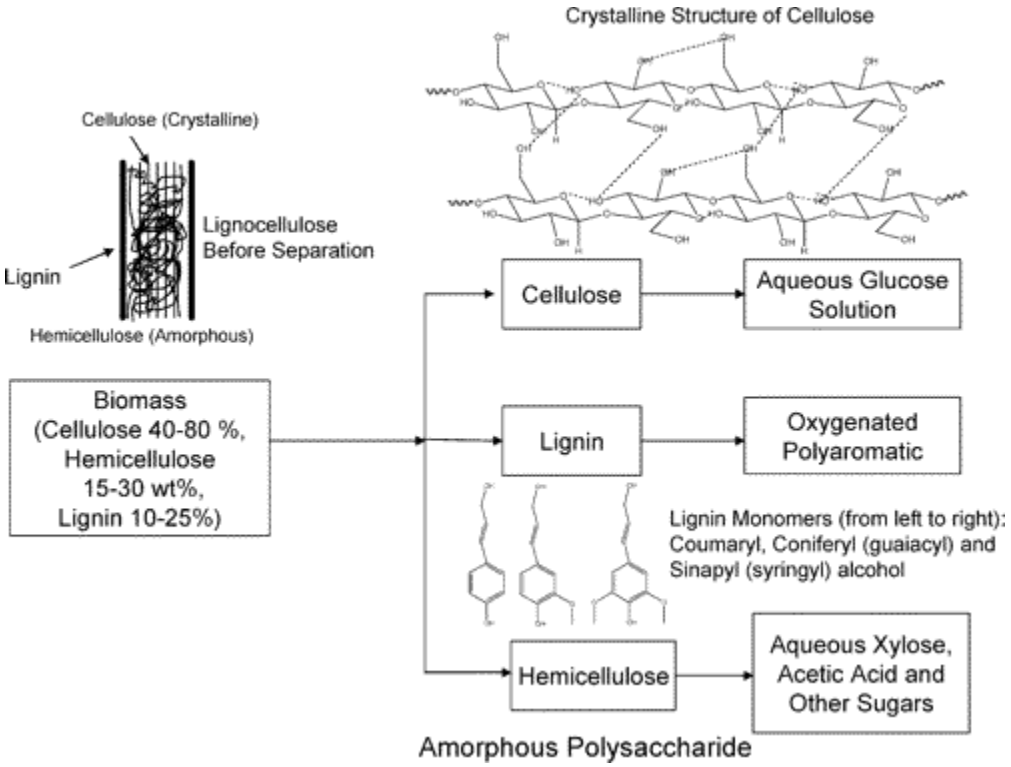

Figure 0.2. Structures of different biomass fractions (lignocellulose, cellulose, lignin, and hemicellulose) before and after reactions. Figure reproduced from Evans et al.[7]

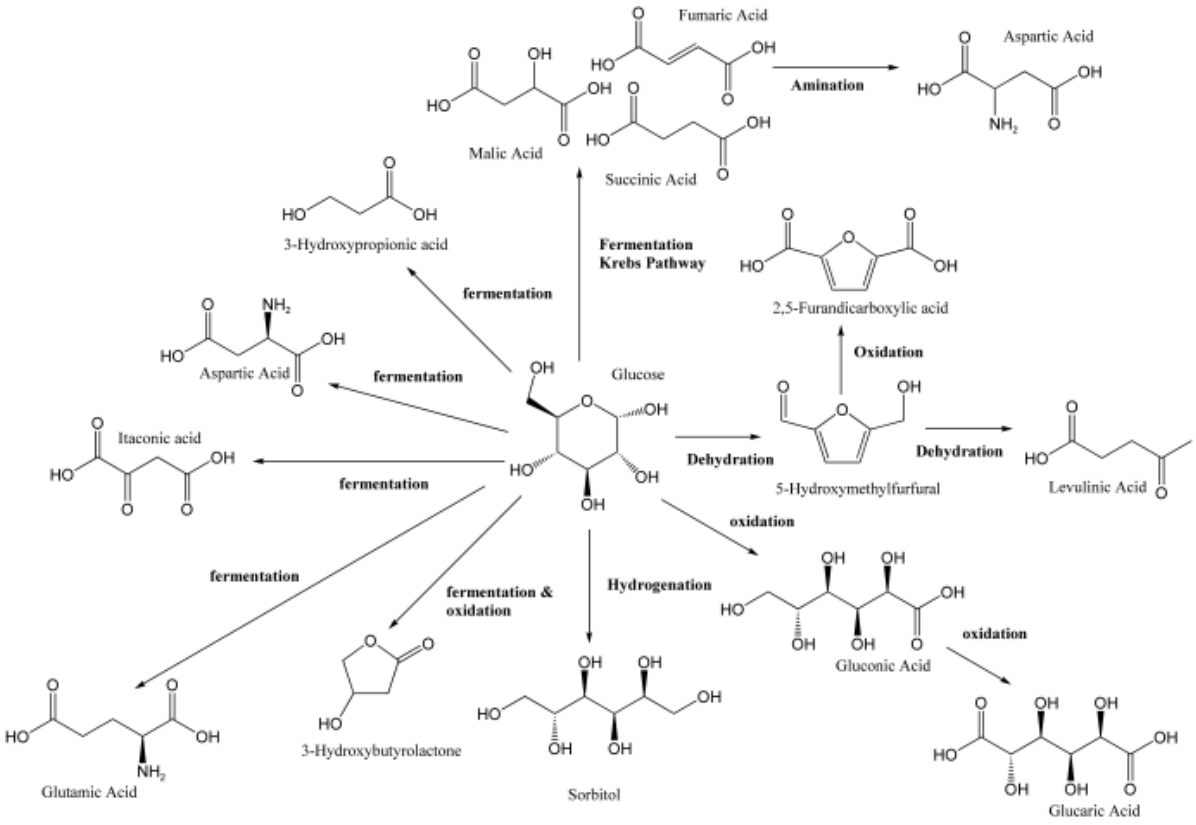

Figure 0.3 Top value-added chemicals from glucose. Figure reproduced from Chheda et al.[8]

Hydrolysis of lignocellulosic biomass can potentially produce a large variety of carbohydrates. As seen in Figure 0.3, it is plausible to produce a diverse range value-added chemicals from glucose including glutamic acid, aspartic acid, levulinic acid.[8] This flexibility as a feedstock can enables biomass-based production of chemicals to replace key building block chemicals currently derived from petroleum. For example, Hydroxymethylfurfural (HMF), which can be produced via selective dehydrogenation of hexoses, has a large potential as a replacement for terephthalic aicd, a widely used component in various polyesters, such as polyethylene terephthalate (PET) and polybutyleneterephthalate (PBT).[9] Petroleum feeds usually have a low extent of

functionality (e.g., -OH, -C=O, -COOH) which makes these feeds directly suitable for use as fuels after appropriate catalytic processing (e.g., cracking to control molecular weight, isomerization to control octane number).[8] Unlike petroleum, biomass-derived carbohydrates contain excess functionality for use as fuels and chemicals. Method needs to be developed to control the functionality in the final product from biomass. Furthermore, because of a high degree of functionality, carbohydrates have high reactivity and low volatility, and they must be typically be processed in the condensed phase.[8] The control of the high functionality of carbohydrates and consequential necessity of the development of efficient liquid phase technologies is one of the overarching challenges that must be tackled to realize biorefinery concepts in practical settings.

1.2 Critical Role of Heterogeneous Catalysis in Biomass Conversion

The primary advantage of heterogeneous catalysts is that since they are solid, they can easily be separated and recycled from the gas and liquid reactants and products.[5] In contrast, it is difficult to separate and recycle homogeneous catalysts and enzymatic catalysts. Another strength of heterogeneous catalysts is their stability to severe reaction conditions. Higher reaction temperature leads to higher reaction rate and smaller reactor size. In comparison, biological catalysts can only survive at low temperatures. These observations suggest that heterogeneous catalyst have potential to contribute in important ways to the realization of biorefineries.

The development of petroleum industry to produce chemicals and fuels largely depended on traditional heterogeneous catalyst tailored to petroleum-derived feedstocks. These catalysts can also be applied to the conversion of biomass-derived feedstocks. For

example, traditionally, the petroleum industry uses supported cobalt-molybdenum and nickel-molybdenum catalysts for hydrotreating of crude oil. These catalysts are now also used for hydrotreating biomass-derived feedstocks such as vegetable oils and bio-oils, but a limitation on yield and selectivity coupled with catalyst stability. Compared to petroleum-derived feedstocks, biomass-derived oxygenates have different functionality (i.e., organic acids, aldehydes, ketones) and impurities (i.e., amino acids, sodium, potassium). It is imperative to develop new catalysts that are specifically suited for use with biomass-derived feedstocks. The synthesis of these new catalytic materials will require a fundamental understanding of the reaction in biomass conversion at a molecular level.

At the molecular level, catalytic reactions are series of elementary reaction steps that occur on active sites.[10] In-situ spectroscopic studies (i.e., infrared, x-ray photoelectron spectroscopy, x-ray absorption spectroscopy, UV, Raman, NMR, etc.,) of interaction between reactants and intermediates and heterogeneous catalysts in the gas phase have elucidated surface species and catalytically active structures under actual reaction conditions in processes of the petrochemical industry.[10] Knowledge of these structure-activity relationships allows optimizing the performance of the catalyst, but also provides critical information to rationally design more efficient catalytic materials [11]. These in-situ spectroscopic experiments are not useful when studying the interaction between biomass and the catalyst because water, a dense medium, very strongly absorbs light in the important regions in the mid-IR range. Therefore, detailed studies on the surface interactions of biomass-derived oxygenates are rare.[12-14]

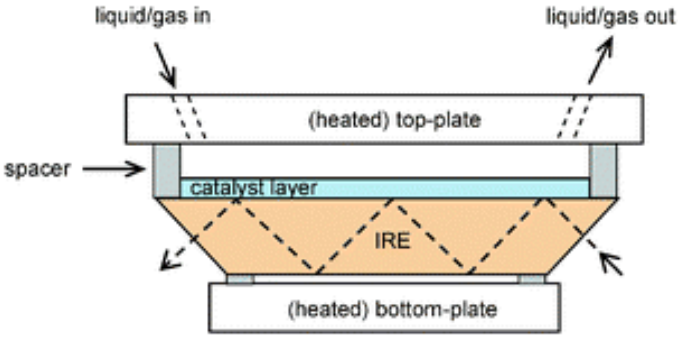

Figure 0.4. Schematic representation of ATR principle. Figure reproduced from Evans et al .[15]

Attenuated Total Reflection Infrared Spectroscopy (ATR-IR) is a good solution for studying molecular vibrations at the solid-liquid interface since the evanescent wave is restricted to the region near the interface, thereby minimizing the contribution from the liquid. A typical experimental set up for ATR-IR is shown in Figure 0.4. For example, Baiker's group resolved the nature of active sites and the corresponding reaction mechanism by studying the oxidation of benzyl alcohol over supported palladium catalysts and thin palladium films using ATR-IR spectroscopy.[16] Adsorption and oxidation of CO and decomposition of small molecules such as formaldehyde over Pt/Al_2O_3 catalysts were also studied.[17] In combination with kinetic studies, ATR-spectroscopy was adopted to investigate the water–gas shift reaction and methanol reforming over Pt/Al_2O_3, finding differences in kinetic parameters when comparing vapor phase reactions with the corresponding liquid phase.[18] Those studies have shown the potential of ATR-IR spectroscopy as a tool to elucidate the mechanism of biomass conversion in a condensed phase.

Another possible way to elucidate a condensed phase reaction mechanism is to mimic the reaction with a gas phase reaction, which enables the application of the traditional spectroscopy techniques. Probe molecules that have similar functionality to biomass-derived oxygenates and high volatility would undergo similar transformation and configuration of adsorbed surface species when interacting with the catalyst. This similar functionality of probe molecules can enable studies of surface reactions and the molecular configuration of adsorbed surface reactant and reaction intermediates on the active sites of a catalyst. For example, temperature-programmed desorption (TPD) and thermogravimetric analysis (TGA) found that acetonitrile and diethyl ether formed 1:1 complexes with Sn sites in beta zeolites and decomposed reversibly upon mild heating in vacuum.[14] In the same study, 2-methyl-2-propanol underwent dehydration to butene and water over a very narrow temperature range centered at 410 K over Sn BEA.

1.3 Objectives and Organization

The overall objective of this body of work is to investigate the surface species formed on various types of heterogeneous catalysts including supported metal, metal oxide, and zeolites for studying the interaction of biomass-derived oxygenates and heterogeneous catalyst. This knowledge will help to bridge the gap between the largely empirical knowledge of which catalysts happen to work well for certain systems and the largely unanswered question of why one catalyst behaves differently than another. Furthermore, this knowledge will be essential for the design of catalyst for biomass upgrading to realize the biorefinery. Probe molecules which have similar functionality to biomass-derived oxygenates will be utilized to mimic the catalytic system for biomass conversion since these molecules are functionally very similar to the majority of biomass-derived

carbohydrates and is highly likely to undergo the similar reaction pathway. As a result, the knowledge gained from the molecules used in the present work will be very relevant for many other biomass-derived carbohydrates of interest.

In Chapter 2, the surface interactions of glycerol, sorbitol, and glucose on Pt/γ-Al_2O_3 were studied by in-situ attenuated total reflection IR(ATR-IR) spectroscopy. With this approach, surface species on a catalyst can be probed effectively while keeping the contribution from the liquid solvent marginal to preserve many important regions of IR spectrum. This method enables us to elucidate the surface intermediates of kinetic regarding the APR of glycerol over a Ptγ-Al_2O_3 catalyst and assess the dynamics of their formation and conversion. The reaction temperature also will vary during APR reaction to investigate the dependency of types of surface species and its accumulation on temperatures.

In Chapter 3, we will characterize the Lewis active sites of Sn BEA, the most representative zeolites for biomass conversion, for aldol-condensation and isomerization of simple C3 oxygenates using Ultra-high Vacuum transmission IR spectroscopy (UHV-IR). First, we will try to observe strongly bound adsorbates that are formed from the interaction of acetone and hydroxyacetone with Sn sites. Following TPD analysis using IR spectroscopy will explore the further transformation of the formed adsorbates in response to increasing temperature. Also, H_2O, which is common solvent for the conversion of biomass-derived oxygenates, will be dosed into the IR cell to investigate the effect of H_2O on the adsorbates. Lastly, we will synthesize the different set of heteroatom-doped zeolites by doping Mo and W precursor into the zeolite topology, which will have different Lewis

acid characteristics such as electron affinity, and Lewis acid hardness, and size of metal inside the zeolites. These materials will give us insight which parameter will be the most influential for the isomerization and C-C coupling of biomass-derived oxygenates.

In chapter 4, we will elucidate the redox properties of MoO_3 for biomass conversion using probe molecules (ethanol and acetaldehyde). The simple C2 oxygenates will be dosed over MoO_3 in Ultra-High Vacuum transmission (UHV) conditions and IR spectroscopy will be used to observe the surface species formed from ethanol. To elucidate the effect of alcohol solvent on the redox property of MoO3, the MoO3 activated at UHV condition will be exposed to methanol and dosed again with ethanol and acetaldehyde. This work will be beneficial to understand the reported recent catalyst reaction of MoO_3 during the conversion of sugar in alcohol solvent.

In-situ ATR-IR study on the Mechanism of Aqueous Phase Reforming of Polyols and Sugars over Pt/γ-Al_2O_3

1.4 Background

In the 20th century, the petrochemical industry developed numerous processes for converting hydrocarbons into commodities. However, diminishing reserves of fossil feedstocks and related carbon dioxide emissions have motivated an intensive search for renewable sources of fuels and chemicals. In this context, biomass is considered as a sustainable long-term solution as a feedstock.[1, 8, 19] Aqueous Phase Reforming (APR) of biomass has gained significant attention as a promising heterogeneously-catalyzed process for converting oxygenated carbohydrates, such as sugars (e.g., glucose) and polyols (e.g., methanol, ethylene glycerol, glycerol and sorbitol), into H_2 and CO_2 at temperature near 500 K.[20-23] As such, this process can provide the hydrogen needed in many other biorefining processes, such as hydrodeoxygenation.[1]

APR has several advantages over the conventional steam reforming processes. Specifically, APR operates at relatively low reaction temperatures and elevated pressures. This eliminates the need to evaporate both water and the oxygenated hydrocarbons, leading to energy saving.[23-24] Also, a hydrogen stream with low amounts of CO is produced in a single reactor because APR reaction takes place at temperatures where the water-gas shift (WGS) equilibrium is favorable for the forward reaction.[20, 23] Moreover, APR is conducted at pressures (typically 15–50 bar) where pressure-swing adsorption and membrane technologies can efficiently separate hydrogen from the effluent.[24] In principle, aqueous

phase reforming can be performed with any polyol, but the H_2 yield decreases notably with larger molecules, such as sorbitol.[25] Even lower yields were reported for the conversion of glucose.[25] The reaction pathways of APR of biomass-derived polyols have been studied by many research group by the reasons for the strong dependence of the H_2 yield on the feedstock are not entirely understood.[25-28]

Effective catalysts for APR require high activity for C-C bond cleavage and the WGS reaction, but activity for CO hydrogenation reduces the hydrogen selectivity and results in the formation of light alkanes.[29] When acidic supports catalyze dehydration steps, various reaction products, such as alcohol, aldehydes, and alkanes, can be co-produced.[27] Among a set of monometallic catalysts (i.e., Pt, Ni, Ru, Rh, Pd, Ir.), Pt was found to have the best combination of activity for C-C bond cleavage and the WGS reaction.[22] Among the different supports (i.e., TiO_2, Al_2O_3, carbon, SiO_2, ZrO_2, CeO_2, and ZnO) investigated for Pt particles, Al_2O_3 exhibited the highest selectivity for hydrogen selectivity (>90%).[30] A large particle size of Pt is beneficial for H_2 selectivity since low index Pt surfaces favor C–C bond cleavage.[31] However, Several studies showed that CO oxidation by WGS reaction is the rate-limiting step in APR, and the reaction is strongly inhibited by adsorbed hydrogen and CO on the surface.[18, 20-21]

CO oxidation on metal surfaces is a traditional area of surface science,[32-34] and many efforts have already been made to understand this reaction at the molecular level, typically studying CO conversion on single crystal surface (i.e., Pt(111)) both in experimental and theoretical approaches in ultra-high vacuum.[35-38] Small amounts of H_2O in gas phase can convert CO to CO_2 via the WGS reaction even at low temperatures.[35, 39] In addition, DFT calculation showed that activation barrier of CO oxidation is reduced in

the presence of H_2O vapor.[39-40] These studies cannot be directly applied to the APR reaction conditions since the chemical potential of water is much higher, and water can affect reaction paths by solvating surface species and transition states.[41] Moreover, it is important to account for the presence a variety of exposed facets in supported metal catalysts.

Attenuated total reflectance infrared (ATR-IR) spectroscopy is a powerful approach to probe reactions on solid-liquid or solid-gas interfaces. A study of methanol reforming over Pt/γ-Al_2O_3 in vapor and liquid phase showed that CO is formed as intermediate on Pt and that the surface coverage by CO decreases as the partial pressure of H_2O increases.[18] In the same study, it was shown that product inhibition by adsorbed hydrogen reduces the number of surface sites that are available for activating methanol. H_2O has a positive effect on the rate of CO oxidation over Pd/Al_2O_3 and causes a red shift of the stretching vibration of CO species compared to dry conditions.[42] Similarly, a large red shift of the stretching vibration of CO adsorbed on Pt/Al_2O_3 indicated that the C-O bond is weakened by formation of an activated CO-water complex.[43] These studies provide insight into the nature of surface species on metal particles during APR. However, few studies directly investigate the rates of formation and conversion of surface bound CO. Recently, our group reported that Pt/Al_2O_3 readily converts glycerol to adsorbed CO at room temperature once metal sites are cleaned by exposing them to hydrogen and oxygen saturated water in an alternating order and that bridging CO can be converted by water gas shift even at room temperature.[13]

In addition to the formation and oxidation of CO by the WGS reaction, it is important to understand how APR is affected by the presence of additional surface species that can be formed from biomass-derived oxygenates containing multiple functional

groups. Various surface intermediates (e.g., acetate, carbonate, crotoaldehyde, acetyl, acetone, and adsorbed linearly bound and bridging CO) were identified in spectroscopic studies of ethanol conversion over supported metal catalysts, such as Pt/Al_2O_3 and Rh/Al_2O_3.[44-48] The key difference between surface intermediates on single crystal metal surfaces and metal-oxide-supported metal particles is the possible presence of oxygenated surface species at the interface between metal particles and on the support. Glycerol adsorbs strongly on Lewis acidic metal oxides by forming a cyclic species, which involves a bridging alkoxy bond between a primary alcohol group and the Lewis acid site as well as a non-dissociative interaction of the other primary alcohol group with the same site.[49-50] Under conditions similar to the operating conditions of APR (i.e., 463 - 498 K), ketones or aldehydes can also form on the surface of Pt/Al_3O_3,[27] and ketones can strongly adsorb on supported metal particles under similar conditions.[51]

Here, we report the effect of size and functionality of oxygenate molecules on the formation of surface species on 5 wt% $Pt/\gamma\text{-}Al_2O_3$ in aqueous phase using in-situ ATR-IR spectroscopy. Specifically, kinetics of formation and conversion of linearly bound and bridging CO from glycerol, sorbitol, and glucose are studied at different temperatures, and the presence of co-adsorbed surface species is discussed.

1.5 Experimental Method

1.5.1 Materials

Glycerol, sorbitol, and glucose (99%) and 5 wt% Pt on $\gamma\text{-}Al_2O_3$ were used as received from Sigma Aldrich. A Barnstead NANO pure ultrapure water was used to further

purify deionized water up to 18.2 MΩ/cm. All H_2, O_2, and He gases were purchased from Airgas with ultra-high purity grade (UHP, grade 5).

1.5.2 Characterization

X-ray diffraction (XRD) patterns of 5 wt% Pt on γ-Al_2O_3 were obtained with a Philips X'pert diffractometer using a X'celerator module using Cu Kα radiation. Diffractograms were collected at incident angles from $2\theta = 5°$ to 70° with a step size of 0.0167°. Nitrogen physisorption measurements were taken using a Micromeritics ASAP 2020 Physisorption Analyzer. Samples were degassed under vacuum at 250 °C for 4 h prior to analysis. The surface area of the sample was calculated from the adsorption isotherm in the region $0.05 < P/P_0 < 0.3$, based on the BET method[52]. The BJH method[53] was also adopted to calculate average pore diameters of the sample in the region $0.05 < P/P_0 < 0.99$. Pyridine adsorption followed by IR spectroscopy was performed using a Thermo-Nicolet 8700 FT-IR spectrometer with an MCT/A detector. For every spectrum, 64 scans were accumulated at a resolution of 4 cm^{-1}. The sample was pressed into the self-supported wafer and then mounted into a custom-built vacuum chamber with ZnSe window. The activation of the catalyst wafer was conducted at 500 °C at $< 10^{-6}$ mbar for 12 h, and a background spectrum was taken after lowering the temperature to 150 °C. Pyridine was introduced into the chamber at a partial pressure of 0.1 mbar for 30 min. The spectrum for pyridine adsorption were taken after the chamber was evacuated for 30 min. After the experiment, the density of the catalyst wafer was determined by weighing a cutout of the wafer with a diameter of 6.35 mm (1/4 inch). The concentration of Lewis and Brønsted acid sites was determined by the integrated area of the peaks of chemisorbed pyridine and pyridinium

ions around 1445 and 1540 cm^{-1}, respectively, the calculated density of the wafer, and the molar extinction coefficient of the catalyst. The molar extinction coefficients were taken from Datka et al..[54] ^{27}Al MAS-NMR experiments were conducted with a Bruker DSX 400 spectrometer, which uses 4 mm zirconia at spinning rate of 12 kHz. The resonance frequency for ^{27}Al was 104.2 MHz. A $\pi/12$ pulse was used, and the recycling delay was 250 msec. Each spectrum consisted of a minimum of 2400 scans. Aqueous $Al(NO_3)_3$ was used as a reference compound (δ = 0 ppm). Transmission electron microscopy (TEM) images were performed with a JEOL 100CX microscope using a 100 kV acceleration voltage. The samples were prepared by applying a slurry of the catalyst in ethanol on a graphene coated, 200 mesh copper grid. The slurry was sonicated for 15 min prior to applying to the sample grid. The Pt particle size distribution was determined based on these micrographs.

1.5.3 In-situ ATR IR spectroscopy

All spectra were acquired again using a Thermo-Nicolet 8700 FT-IR spectrometer with a MCT/A detector. Each spectrum was collected with a resolution of 4 cm^{-1} and 32 scans. The heated flow-through ATR cell containing an Internal Reflectance Element (IRE) crystal (ZnSe, 45°, 80 x 10 x 3 mm, Pike Technologies) was purchased from Pike Technologies. During the experiments, a spectrum was collected every 30 s. A suspension of 12.5 mg of catalyst in 10 mL of ultrapure water was prepared and sonicated for 30 min. The catalyst was deposited onto the ZnSe crystal in layers. After each deposition step, the water in the layer was allowed to evaporate at 60 °C in an oven. The process was repeated until all of the suspension was deposited on the crystal. For each experiment, 4 different

feeds were prepared in separate bottles: ultrapure water degassed with He, aqueous solution of 1 wt% of reactant (i.e. glycerol, sorbitol, and glucose) degassed with He, ultra-pure water saturated with O_2 gas, and ultrapure water saturated with H_2 gas. These feeds are henceforth referred to as H_2O, reactant (i.e. glycerol, sorbitol, and glucose), $O_2(H_2O)$, and $H_2(H_2O)$, respectively. The solutions were saturated with the respective gasses for at least 4 h prior to the start of each experiment. The feed solutions were pumped into through the ATR-IR cell with an Agilent 1200, quaternary HPLC pump at a flow rate of 5.0 mL/min. The catalyst bed in the ATR cell was stabilized in a flow of degassed ultrapure water (5.0 mL/min) for 3 h prior to the start of an experiment until the system reached a mechanically stable state of the catalyst bed (usually less than 1 hour, as observed by reaching an unchanging absorbance spectrum). To remove adsorbed carbonaceous contaminants from the catalyst, H_2O, $O_2(H_2O)$, and $H_2(H_2O)$ was flowed through the ATR IR cell for 30 minutes each.[13] This cleaning procedure was repeated two times. The background was collected during the last minute of the cleaning procedure prior to the start of the experiment. During the experiments, different feed solutions flowed through the cell. A typical experiment consisted of 30 min of reactant solution, followed by H_2O, and $O_2(H_2O)$. This sequence was repeated to investigate the activity of the catalysts in the second use during APR. Before the second flow period of the reactant solution, H_2O was flowed through the cell for 10 min to remove any dissolved O_2 from the pores of the catalyst. Separate experiments were performed with glycerol, sorbitol, and glucose solutions as reactants at temperatures of 24, 50, and 72 °C.

Thermo Fisher Scientific Inc. GRAMS 9.1 was used to analyze and integrate the peaks in the spectra. The peak of linearly bound CO was integrated from ca. 2125 to 2015 cm^{-1}, and the one bridging CO on Pt peak was integrated from ca. 1870 to 1734 cm^{-1}.

1.6 Result

1.6.1 Catalyst characterization

The results from N_2 physisorption analysis are summarized in Table 1. The x-ray diffractogram in Fig. S1 shows two main peaks at $2\theta = 44.6°$ and 66.7° that represent the (4 0 0) and (4 4 0) planes of the defective spinel structure of the γ-Al_2O_3 support.[55] The ^{27}Al MAS NMR spectrum contained two peaks at 7 and 63 ppm (Fig. S2), which are attributed to octahedrally and tetrahedrally coordinated Al atoms. The integrals of these peaks showed that the sample contained 77% octahedrally coordinated Al and 23% tetrahedrally coordinated Al species, which is typical for γ-Al_2O_3.[56] An average Pt size of 3 nm was determined by measuring 177 Pt particles in TEM micrographs. IR spectra of adsorbed pyridine (Fig. S3) exhibited peaks from the ν_{19b} mode at 1448 cm^{-1} and the ν_{8a} mode at 1613 cm^{-1} that are attributed to pyridine coordinated to Lewis acid sites. The concentration of Lewis acid sites was quantified at 18 μmol/g (Table 0.1). However, the ν19b mode of pyridine coordinated to Brønsted acid sites (i.e., pyridinium ions), which is commonly observed at ca. 1540 cm^{-1}, was absent.[57]

Table 0.1. Results from N_2 physisorption, TEM micrographs and the measurement of acid concentration of the catalyst (5 wt% Pt/γ-Al_2O_3).

BET surface area	96 (m^2/g)
BJH adsorption surface area of pores	101 (m^2/g)
BJH desorption surface area of pores	119 (m^2/g)
BJH adsorption surface area of pores	0.24 (m^2/g)
BJH desorption surface area of pores	0.22 (m^2/g)
Adsorption average pore width	9.8 (nm)
Average particle size of the Pt/γ-Al_2O_3	62.7 (nm)
Concentration of Lewis acid sites	18 (μmol/g)

2.3.2 Identification of surface species formed during APR of polyol and sugar

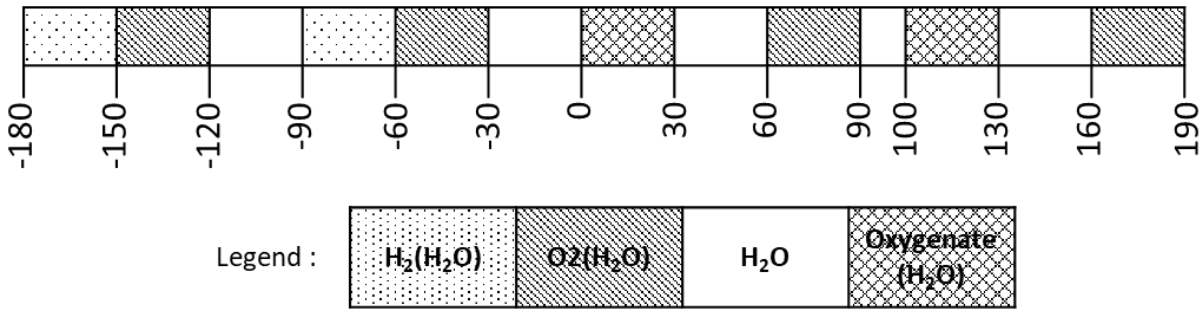

Figure 0.1. Flow period used during the cleaning cycle experiment (minuses time scale) and flowing reaction (plus timescale)

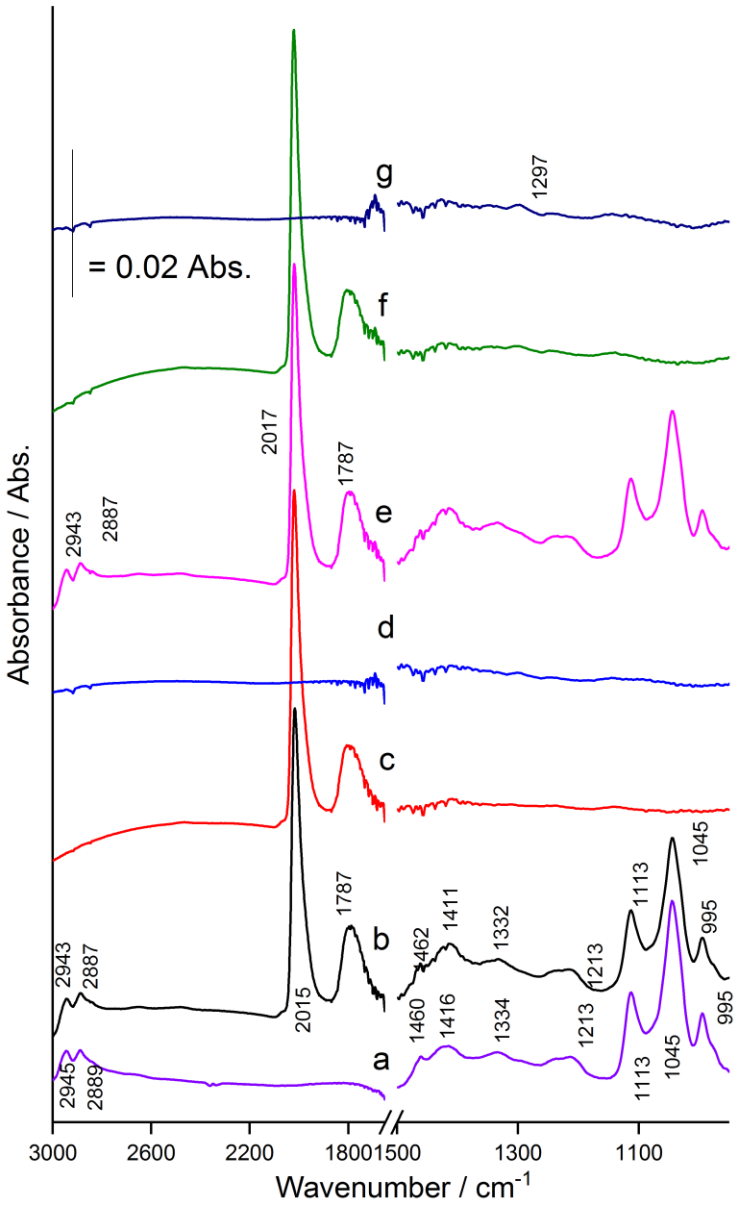

Figure 0.2. ATR-IR spectra of Pt/γ-Al_2O_3 catalyst layer during aqueous glycerol reforming after the sequential cleaning pretreatment. All of the spectra were taken after 10 min of their respective flow period. a). 1 wt% aqueous glycerol flow without catalyst b). 1st 1 wt% glycerol flow c). 1st H_2O flow d). 1st O2 flow e). 2nd 1 wt% glycerol flow f). 2nd H_2O flow g). 2nd O_2 flow.

When Pt/γ-Al_2O_3 coated on a ZnSe crystal was placed in an in-situ ATR-IR cell and exposed to an aqueous glycerol solution (1 wt%), the resulting IR spectra contained two strong peaks at 2009 and 1782 cm^{-1}, which are attributed to the stretching vibrations of linearly bound CO (CO_L) and bridging CO (CO_B) on the Pt surface, respectively (Figure 0.2b).[13, 27, 58] Over the course of the aqueous glycerol flow (i.e., 30 min), these peaks gradually shifted to 2015 and 1787 cm^{-1}, respectively, due to increasing dipole-dipole interactions with increasing coverage.[43] The other peaks observed in these spectra are all attributed to various modes of glycerol according to Colthup et al. (Table 0.2).[59] Any significant peak which can be attributed to hydroxyacetone and glyceraldehyde was not on the spectrum in any flow period. When comparing the peaks attributed to glycerol during aqueous glycerol flow over Pt/γ-Al_2O_3 (Figure 0.2a) to the spectrum of aqueous glycerol solution in the absence of a catalyst layer (Figure 0.2b), the changes in positions and shapes of the peaks were marginal. This indicates that most of the intensity of the glycerol peaks in the range from 900 to 1600 cm^{-1} comes from the liquid phase and that the peaks from glycerol in water may obscure smaller peaks of other surface species that might be present on Pt/γ-Al_2O_3.

Table 0.2. Vibrational modes of reactant solution over the empty ZnSe crystal and aqueous reactant solution interacting with the catalyst layer

	1 wt% Glycerol in H_2O / cm-1	0.1 M Glycerol over Pt/γ-Al_2O_3 / cm^{-1}	Δ/ cm^{-1}	1 wt% Sorbitol in H_2O / cm-1	0.1 M Sorbitol over Pt/γ-Al_2O_3 / cm^{-1}	Δ/ cm^{-1}	1 wt% Glucose in H_2O / cm-1	0.1 M Glucose over Pt/γ-Al_2O_3 / cm^{-1}	Δ/ cm^{-1}
$\nu_{asym}CH_2$	2945	2943	2	2940	2943	2	2917	2913	4
$\nu_{sym}CH_2$	2889	2887	2	2889	2890	4	2887	2881	6
δCH_2	1462	1460	2	1462	1462	4		1460	
δOH	1416	1411	5	1414	1411	-2	1432	1415	17
δCH	1334	1332	2	1334	1315	2	1315	1321	-6
CH_2 wag	1213	1213	0	1213	1216	1	1201	1203	-2
νCO 2°	1113	1113	0	1084	1084	0	1082	1080	2
νCO 1°	1045	1045	0	1047	1046	1	1035	1036	-1
CH_2 Rock	995	995	0	1008	1006	2	993	993	0

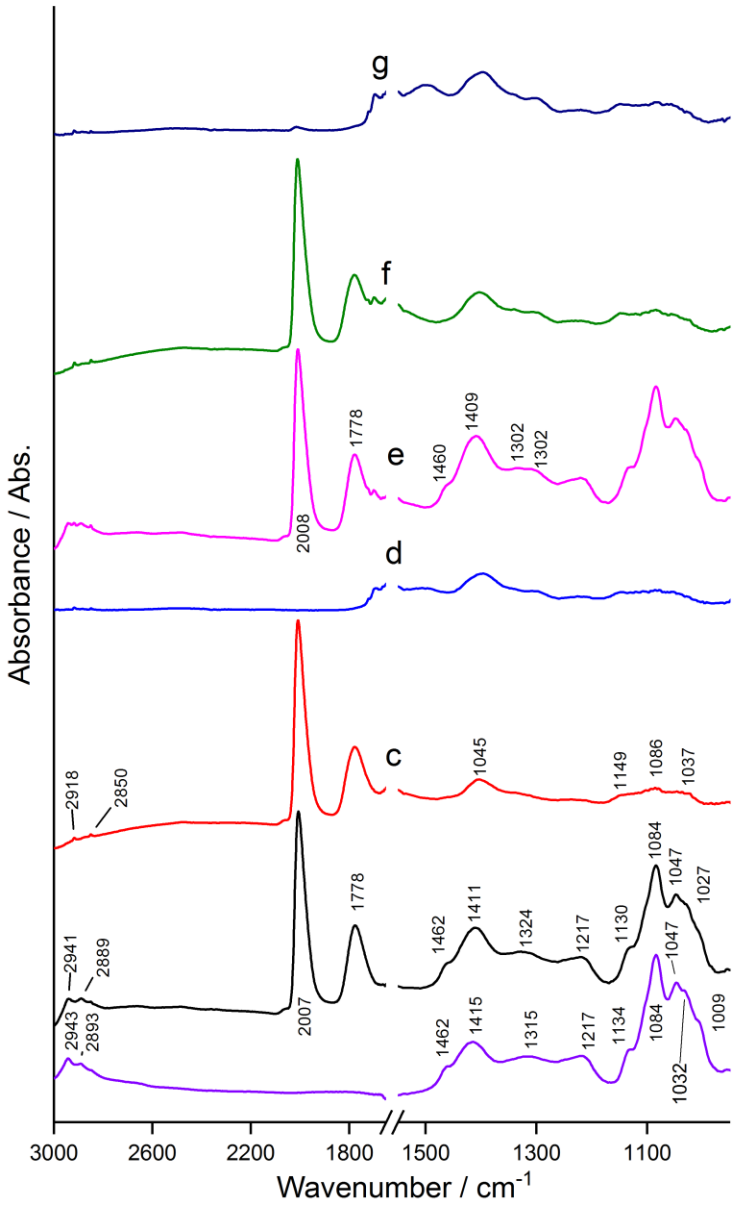

Figure 0.3. ATR-IR spectra of Pt/γ-Al_2O_3 catalyst layer during aqueous sorbitol reforming after the sequential cleaning pretreatment. All of the spectra were taken after 10 min of their respective flow period. a). 1 wt% aqueous sorbitol b). 1st 1 wt% sorbitol l flow c). 1st H_2O flow d). 1st O2 flow e). 2nd 1 wt% sorbitol flow f). 2nd H_2O flow g). 2nd O_2 flow

As soon as the aqueous sorbitol feed was flowed into the cell, CO_L and CO_B were observed again as dominant surface species (Figure 0.3b). The maximum of the CO_L peak

shifted from 1998 cm^{-1} to 2007 cm^{-1} during the sorbitol flow period, while that of CO_B shifted from 1772 to 1778 cm^{-1}.

Peaks located between 950 and 1550 cm^{-1} are attributed to both adsorbed sorbitol and sorbitol in the aqueous phase. (Figure 0.3b). In contrast to the aqueous glycerol feed (Figure 0.2b), which exhibited two distinct νC-O 2° and νC-O 1° modes at 1113 and 1045 cm^{-1}, the νC-O modes of sorbitol gave rise to several peaks at 1130, 1084, 1047 and 1027 cm^{-1}, which might be due to diverse ways for primary and secondary alcohol of sorbitol to interact with H_2O (Figure 0.3b). The differences of peak positions in the absence and presence of the catalyst bed were larger in the experiment with sorbitol compared to glycerol. After 30 min of pure water flow, peaks of the δOH, νCO 2° and νCO 1° modes of sorbitol-derived surface species remained at 1404, 1086, and 1037 cm^{-1}, respectively. Additional peaks remained at 2918, 2850, and 1149 cm^{-1} and are attributed to the $_{asym}CH_2$, $_{sym}CH_2$, and νCO modes of surface alkoxy species on the Al_2O_3 support.[49] During the subsequent $O_2(H_2O)$ flow, CO_L and CO_B surface species were converted into carbonates, as indicated by the peaks at 1698, 1498, and 1393 cm^{-1}(). Also, the remaining δOH and νCO peaks at the end of this flow period (Figure 0.3d) indicated that certain irreversibly adsorbed surface species could not be entirely removed by O_2. The reintroduction of the aqueous sorbitol feed produced a spectrum (Figure 0.3e), which contained the same peaks like the one after the first 30 min of feeding the aqueous sorbitol solution. During the second H_2O flow period (Figure 0.3g), the intensity of the peaks decreased sharply again, but the residual intensities of the modes of $_{asym}CH_2$, $_{sym}CH_2$, ωCH_2, and νCO were slightly higher compared to first H_2O flow period. This observation indicates that some of the

surface species accumulated on the catalyst surface even though the catalyst was subject to the pretreatment of oxygen-saturated water before the re-entering of the reactant.

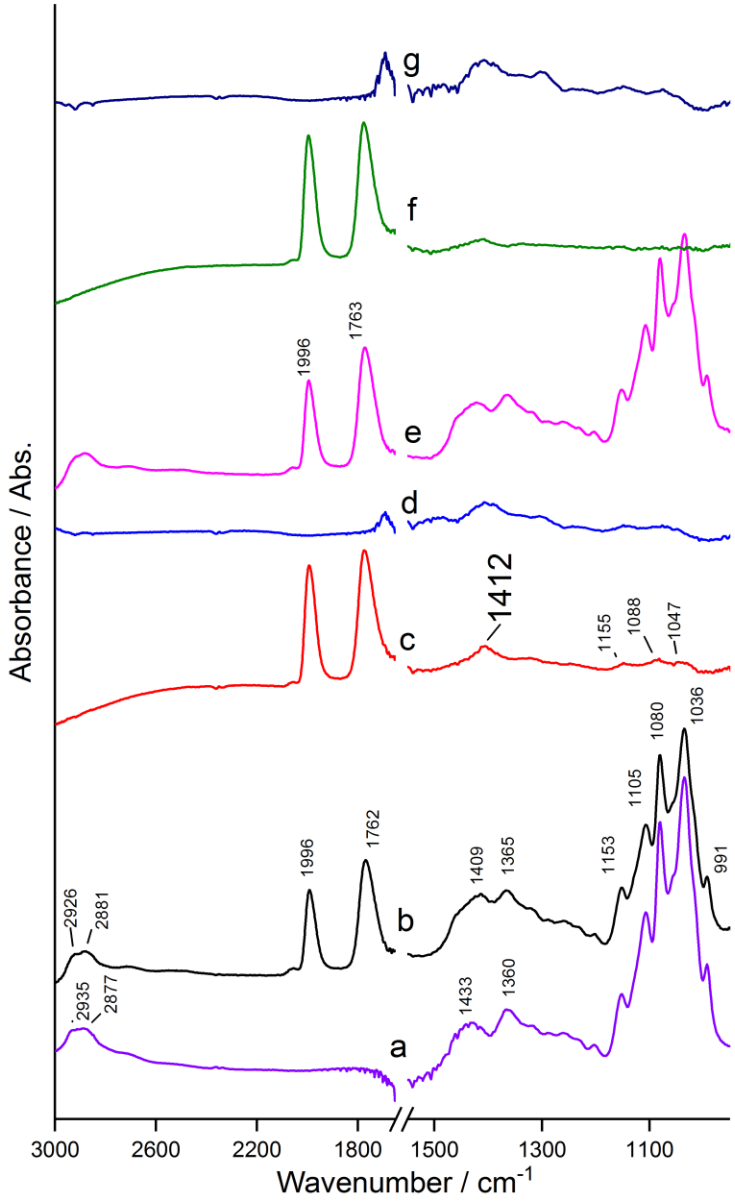

Figure 0.4. ATR-IR spectra of Pt/γ-Al_2O_3 catalyst layer during aqueous glucose reforming after the sequential cleaning pretreatment. All of the spectra were taken after 10 min of their respective flow period a). 1 wt% aqueous glucose b). 1st 1 wt% glucose l flow c). 1st H_2O flow d). 1st O2 flow e). 2nd 1 wt% glucose flow f). 2nd H_2O flow g). 2nd O_2 flow

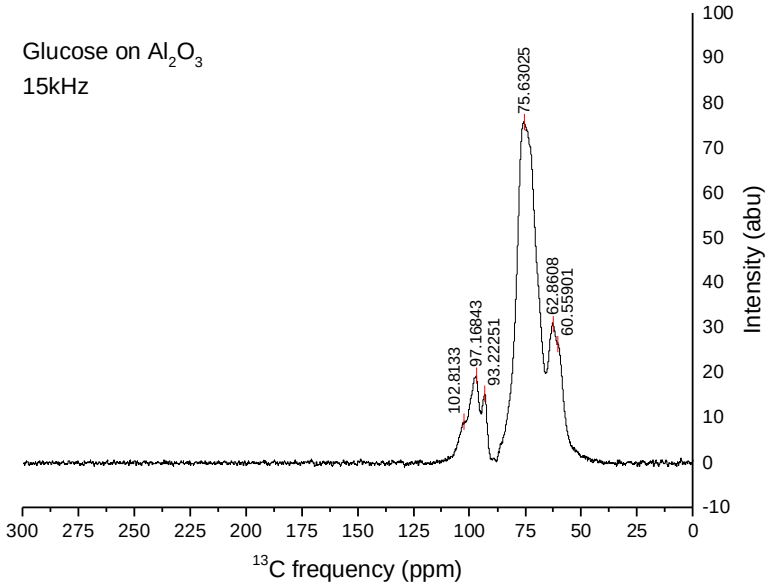

Figure 0.5. 13C NMR spectra of [C13] glucose impregnated on γ-Al_2O_3

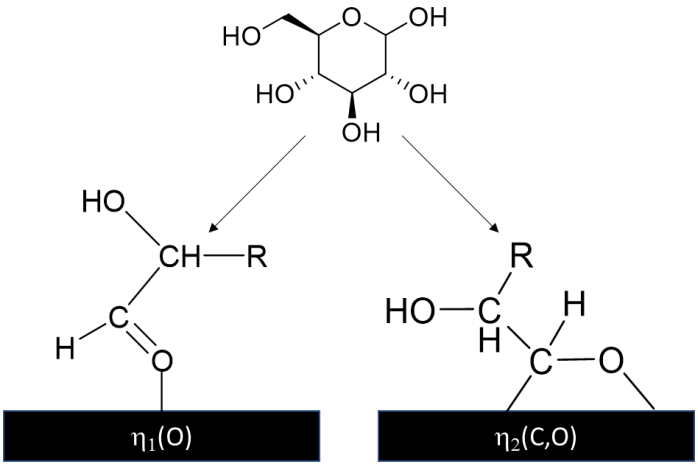

Scheme 0.1. Possible adsorption structure of glucose on Pt surface

When the aqueous glucose solution was passed over Pt/γ-Al_2O_3, the modes of CO_L and CO_B gave rise to peaks at 1982 and 1744 cm^{-1}, respectively (Figure 0.4b) and the CO_L and CO_B blue-shifted to 2007 and 1770 cm^{-1} due to the dipole-dipole coupling in a similar way as we observed in the case of glycerol and sorbitol. However, these peaks were significantly less intense than the those of the same species during the conversion of aqueous glycerol and sorbitol feeds. The spectrum of 1 wt% glucose in aqueous solution exhibited strong bands in the 1160–1000 cm^{-1} region involving νCO modes of COH and COC groups and multiple medium bands in the 1460-1200 cm^{-1} region attributed to CH_2 deformation (δCH_2), and CH_2 wagging, and OH in-plane deformation (δOH) ((Figure 0.4a). Interestingly, the interaction of glucose with the catalyst (Figure 0.4b) produced a peak at 1409 cm^{-1}, which can be attributed to νCO of the η_2 configuration of glucose (Scheme 1).[60] The unexpected νCO vibration indicates that glucose has a different structure on the surface of the catalyst compared to glucose in pure H_2O and this structure change might be mostly related to the ring opening of glucose. The absence of a peak corresponding to a carbonyl group (190 – 205 ppm) in the ^{13}C MAS NMR spectrum of glucose on γ-Al_2O_3 showed that ring-opening does not occur when glucose adsorbs on γ-Al_2O_3 (Figure 0.5). The exclusive existence of cyclic glucose in γ-Al_2O_3 indicates that the Pt particles induced ring-opening of glucose. However, the η_1 configuration of adsorbed glucose which existed at 230 K at a different study in high vacuum[60] was not observed in our current study. After 30 min of pure water flow, peaks of the νOH, νCO 2° and νCO 1° modes of sorbitol-derived surface species remained at 1404, 1088, and 1047 cm-1, respectively. An additional peak at 1149 cm^{-1} is attributed to νCO modes of surface alkoxy species on the Al_2O_3 support. During the subsequent $O_2(H_2O)$ flow, CO_L and CO_B surface

species were converted into carbonates, as indicated by the peaks at 1698, 1498, and 1393 cm-1(Figure A. 5).

1.6.2 Evolution of surface species formed in response to change in temperature

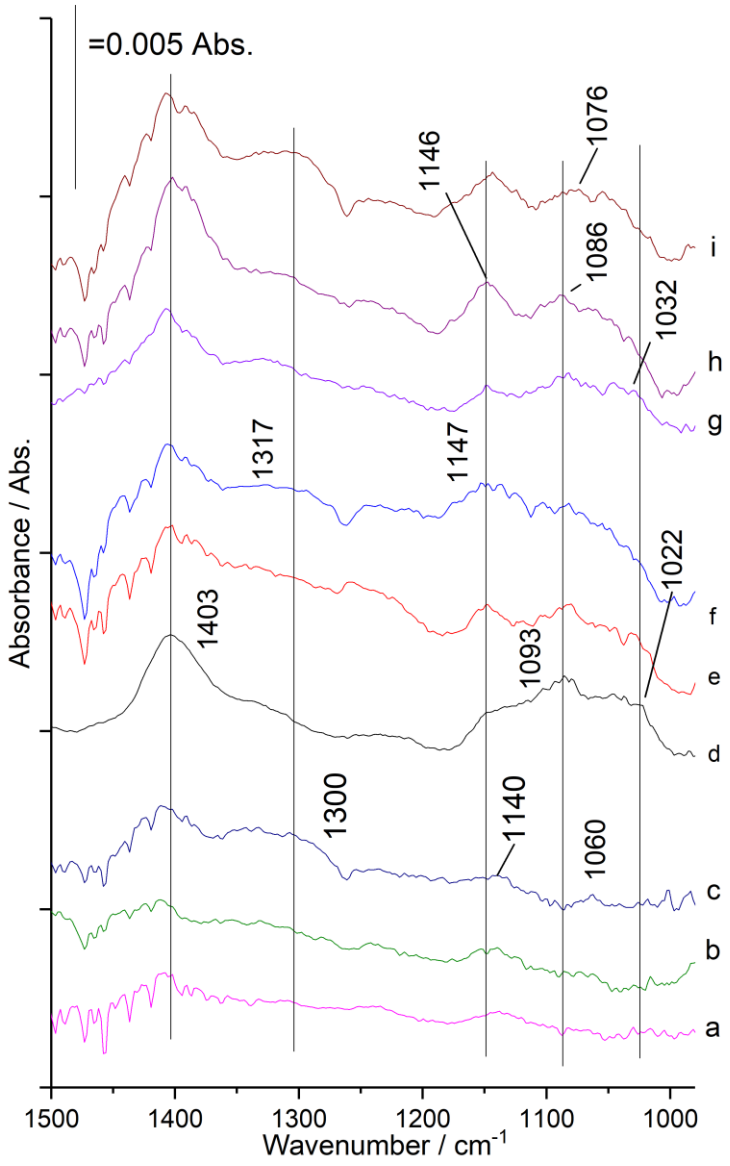

Figure 0.6. ATR-IR spectra during first H_2O flow period. All of the spectra were taken after 10 min of their H_2O flow period. 1 wt% aqueous glycerol flow at 24 °C (a), 50 °C (b), 72 °C (c), 1 wt% aqueous sorbitol flow at 24 °C (d), 50 °C (e), and 72 °C (f)

The influence of the reaction temperature on the formation of surface intermediates from glycerol, sorbitol, and glucose was investigated by comparison of the IR spectra obtained after feeding the aqueous oxygenate solution for 30 min, followed by 10 min of pure H_2O flow at 24, 50 and 72 °C (Figure 0.6). This approach was taken to reduce the spectral contribution from oxygenates in the aqueous phase. The reforming of glycerol mostly did not generate strongly bound surface intermediates compared to sorbitol and glucose (Figure 0.6 a, b, and c) at 24, and 50 °C. However, the existence of the small peak of δOH and νCO at 1140 and 1060 cm^{-1} indicates that alkoxy was present on the γ-Al_2O_3 support. Increasing temperature up to 72 °C produced in the broad peak around 1300, and 1060 cm^{-1} which can be attributed to the combination of δCH_2 and δCH_3, and νCO of 1 or 2-hydroxypropanal via dehydration of glycerol on the γ-Al_2O_3 support due to the increased temperature.[27]

Several prominent surface species were formed from the interaction of sorbitol with the catalyst at all temperature studied (Figure 0.6d, e, f). Specifically, the broad peaks of νCO modes existed between 1000 and 1200 cm^{-1}, and the δOH peak at 1403 cm^{-1} was observed due to the existence of diverse alcohol groups after the decomposition of sorbitol via C-C bond cleavage. The broad peaks in this region indicate that many types of alcohol-derived surface species are present. Increase in temperature to 72 °C (Figure 5d, e, and f) produced a broad peak around 1300, which can be attributed to the combination of δCH_2 and δCH_3, and 1147 cm^{-1} attributed to νCO of alkoxy surface species. We observed that the intensity of νCO 1° of surface intermediates from sorbitol at 72 °C noticeably decreased compared to 24, and 50 °C, which might indicate that primary alcohol groups of surface species near the metal-support interface are dehydrogenated. Therefore, the not fully

decomposed portions of sorbitol may reside on the metal-support interface due to more degree of dehydrogenation at high temperature.

Interestingly, glucose formed similar surface species as sorbitol with peaks of δOH, νCO 2°, and two νCO 1° at 1403, 1144, 1076 and 1057 cm^{-1}. Again, the spectrum at 72 °C (Fig. 5g) exhibited that νCO 1° at 1016 cm^{-1} became significantly reduced compared to the spectrum at 24 and 50 °C (Fig. 4h and 4i). The most prominent difference at 72 °C is noticeably broader δCH_2 and δCH_3 regions around 1300 cm^{-1}.

1.6.3 Kinetics of APR of glycerol, sorbitol, and glucose

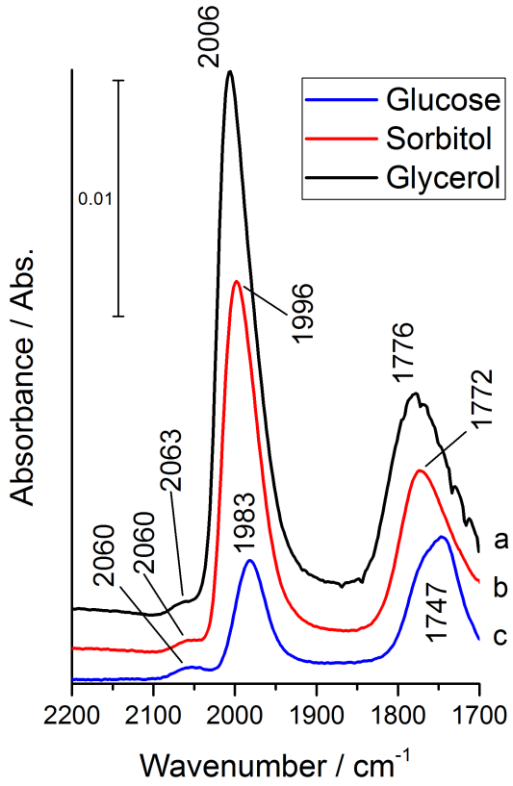

Figure 0.7. Spectrum take after 1 min of exposure of a). glycerol b). sorbitol c). glucose

The spectral region of adsorbed CO species after 1 min of exposure to aqueous glycerol, sorbitol, glucose feeds is plotted in Figure 0.7. Increasing CO coverage on the Pt particles led to increasing dipole-dipole interactions, which caused a blue-shift of the CO modes.[43] A spectrum taken after 1 min exposure exhibited that the frequency of νCO modes in the order of glycerol, sorbitol and glucose. Interestingly, the νCO_B modes at 1747 cm^{-1} decomposed from glucose was able to be deconvoluted into peaks at 1776 and 1743 cm^{-1}, possibly due to the hindered dipole-dipole interactions (Figure 0.7c).

Figure 0.8. Integrated peak area of the νCOL mode as a function of time and types of reactants at 24 °C

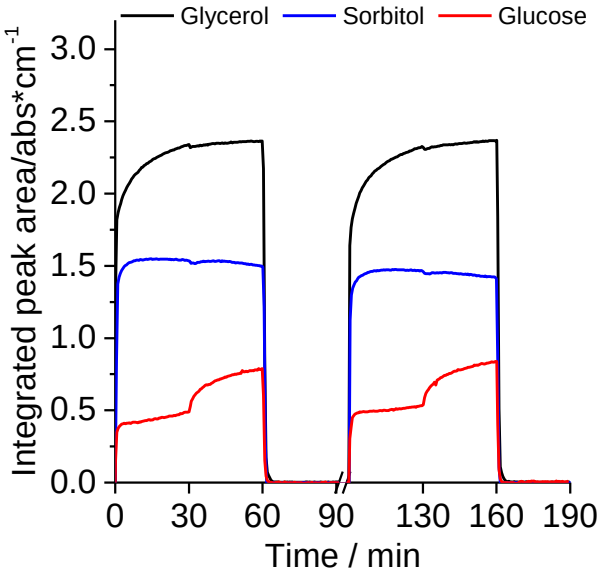

Figure 0.8. Integrated peak area of the νCO_L mode as a function of time and types of reactants at 24 °C

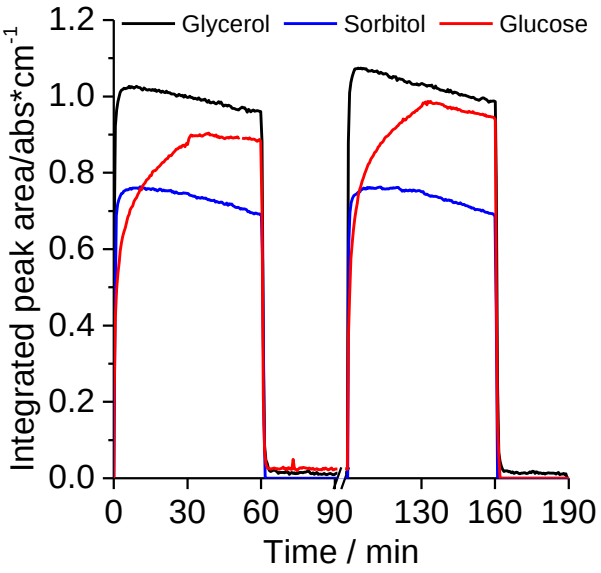

Figure 0.9. Integrated peak area of the νCO_B mode as a function of time and types of reactants at 24 °C

The integration of CO_L and CO_B surface species as observed in Figure 0.7 continuously changed during 1st and 2nd aqueous reforming of glycerol, sorbitol, and glucose. The rates of formation and conversion of CO_L and CO_B as well as the abundance of these species in different experiments were investigated based on the integrals of the respective peaks (Figure 0.9-13). During the conversion of all reactants at all temperatures studied here, CO_L and CO_B were formed when the aqueous oxygenate solution was flowed through the cell for 30 min. The conversion of glycerol at room temperature resulted in the largest integrated area of the CO_L, which was 1.5 and 4.7 times higher than the integrated area of CO_L from sorbitol and glucose, respectively (Figure 0.8). Figure 0.9 shows that the highest area for CO_B was reached after 6 min and 9 min during glycerol and sorbitol flow period, respectively and was followed by a gradual and linear decrease throughout the period in which glycerol or sorbitol were fed and the following H_2O flow period. The

intensity of the CO_L peaks formed from glycerol and sorbitol remained approximately constant during the H_2O flow period.

Figure 0.9 shows that CO_B formed during glucose flow exhibited the saturation behavior up to the end aqueous glucose flow period, which is similar to the trend of CO_L. This saturation behavior led to the 15 % higher coverage of CO_B compared to the maximum coverage of CO_B formed from sorbitol (Figure 0.9). Without a continued supply of reactant during the H_2O flow period, CO_B produced from glucose exhibited a gradual and approximately linear decrease the same as glycerol and sorbitol with a lower rate. Surprisingly, in case of glucose, the intensity of the CO_L band continuously increased in the absence of reactants in the feed during H_2O flow period. After 30 min of H_2O flow, it had increased by 40 % compared to the CO_L band after the aqueous glucose flow (Figure 0.9). Figure A. 5 shows that the increase in the intensity of the CO_L band coincided with a decrease of the peaks corresponding to the νCO mode of adsorbed glucose, which indicates that a reduction in the density of glucose on the surface allows for the production of additional CO_L. The ratios of the integral of the CO_L to CO_B peaks from glycerol and sorbitol was approximately 2 at the end of the period in which the oxygenate solution was provided. In contrast, a much smaller CO_L/CO_B ratio of 0.57 was observed after 30 min of aqueous glucose flow.

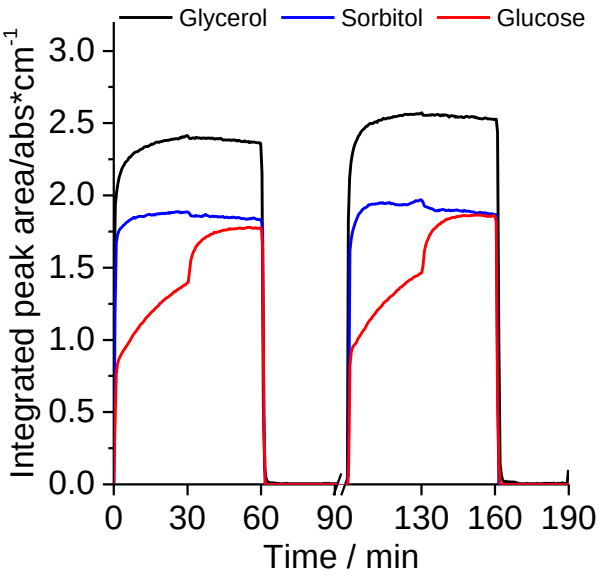

Figure 0.10. Integrated peak area of the νCO_L mode as a function of time and types of reactants at 50 °C

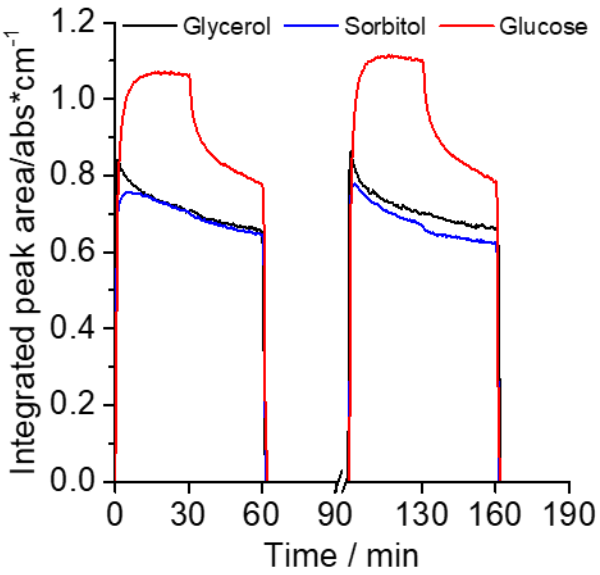

Figure 0.11. Integrated peak area of the νCO_B mode as a function of time and types of reactants at 50 °C

The evolution of the integrated regions of CO_L and CO_B during APR at 50 °C during the two sequences of aqueous reactant, H_2O, and O_2 (H_2O) flow showed similar trends compared to the experiments at 24 °C (Figure 0.10 and Figure 0.11). The increased reaction temperature led to an increase in the maximum coverage of CO_L during the conversion of all reactants sorbitol and glucose (Figure 0.11). Likewise, the maximum CO_B coverage from glucose increased (Figure 0.11). The maximum coverage of CO_B was observed after 6.2 and 6.7 min during the conversion of glycerol and sorbitol, respectively, followed by a gradual and almost linear decline that extended throughout aqueous reactant flow until the end of the H_2O flow period. Interestingly, glucose produced the most CO_B, with integrated peak areas that were 27% and 45% larger than for the CO_B peaks during the conversion of glycerol and sorbitol. In contrast, the conversion of glycerol and sorbitol, the peak area of CO_B from glucose exhibited saturation behavior while the aqueous glucose solution was fed and a sharp decrease at the beginning of the H_2O flow period. Then, the area of the CO_B peak showed the similar gradual decline as observed in the corresponding pure H_2O flow period after conversion of glycerol and sorbitol.

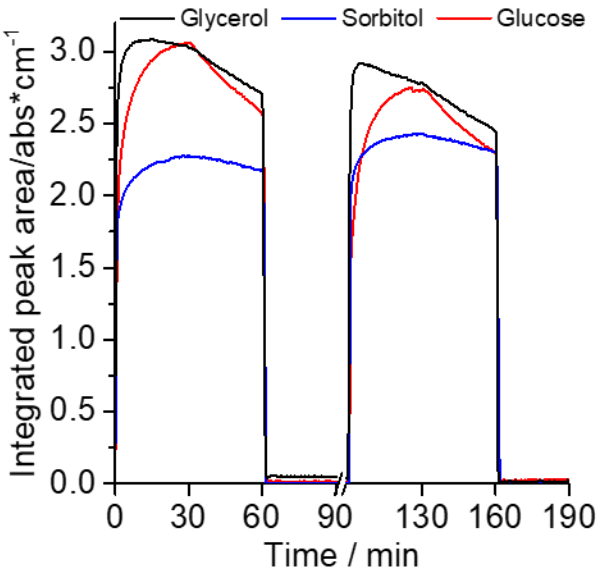

Figure 0.12 Integrated peak area of the νCO_L mode as a function of time and types of reactants at 72 °C

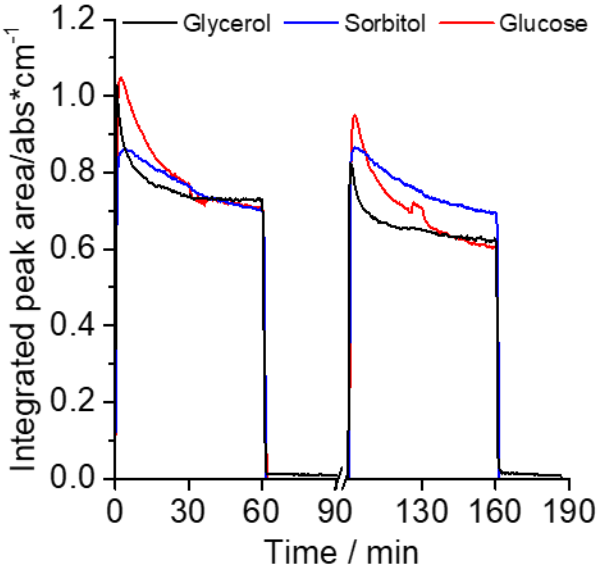

Figure 0.13 Integrated peak area of the νCO_B mode as a function of time and types of reactants at 72 °C

At a reaction temperature of 72 °C, the maximum peak area of CO_L was higher than at 50 °C, and the peak area of CO_L decreased during the water flow period (Figure 0.12). The area of the CO_B peak surface species exhibited a similar behavior for all the reactants with maxima after 0.6, 2.5, and 4.5 minutes for glycerol, sorbitol, and glucose, respectively (Figure 0.13). Then, it decreased sharply even in the presence of the reactants. During the H_2O flow period, the observed rate of CO_B conversion became slower. In case of CO_B from glycerol, sorbitol and glucose, the rate of conversion at this stage was even slower than at 24 and 50 °C.

Up to 24 and 50 °C, during the second use of the catalyst for the decomposition of glycerol, sorbitol, glucose, the coverage of CO_L and CO_B did not change compared to the first use of the catalyst. Also, during the second use of the catalyst for the decomposition of sorbitol, the coverage of CO_L and CO_B did not change compared to the first use of the catalyst. However, at a reaction temperature of 72 °C, Figure 0.13 shows the coverage of CO_L and CO_B for the second use decreased by 8 and 10 % compared to the first use of the catalyst.

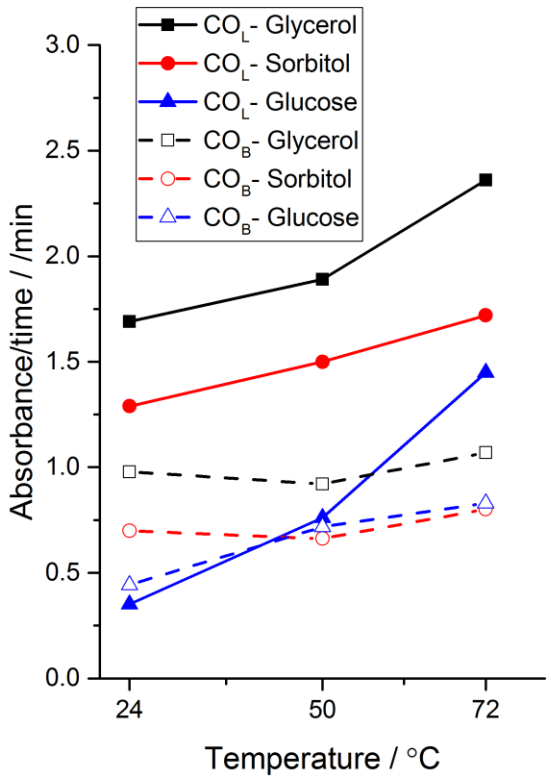

Figure 0.14 The initial rate of formation of CO_L by Integrated peak area of the νCO_L mode after 1 min of exposure of reactants as a function of temperature.

To investigate the rate of formation of CO_L and CO_B at the initial contact of reactants on the catalyst, the rate of the increase in the integrated area for CO_L and CO_B from glycerol, sorbitol, and glucose is plotted in Figure 0.14 as a function. The initial rates of formation of both CO_L and CO_B were fastest during the conversion of glycerol over Pt/γ-Al_2O_3, compared to sorbitol and glucose. The rates of CO_L formation from all reactants increased to a similar extent with increasing temperature. The only exception was a sharp increase in the initial rate of formation of CO_L from glucose at 72 °C (Figure 0.7). The initial rate of CO_B formation changed less as the temperature increased. During the conversion of glycerol and sorbitol, it decreased slightly as the temperature increased from

24 to 50 °C, and then increased when the temperature increased further to 72 °C. The initial rate of CO_B formation from glucose showed a continuous increase, starting from a very low value at room temperature.

1.7 Discussion

1.7.1 Surface species during APR of glycerol, sorbitol, and glucose

It is well-known that polyols can be converted to CO_2 and H_2 in the reforming process in the condensed phase.[4, 13, 18, 27, 61-62] The decomposition of glycerol in aqueous environment produced metal carbonyls (CO) as dominant surface species.[13, 18] In addition, the decomposition of glycerol in APR over Pt/γ-Al_2O_3 produced keto or aldehyde group within the oxygenate by observing a mode of νC=O mode at 1720 cm^{-1} using ATR-IR spectroscopy.[27] Lercher group suggested that the dehydrogenation of hydroxyl groups at primary carbon atoms of polyols is followed by decarbonylation and subsequent water gas shift as the main reaction pathway to produce H_2 and CO in APR process over Pt/γ-Al_2O_3.[27] Therefore, many surface studies observed CO_L, CO_B, and H atoms as dominant surface species on Pt metals.

A study of methanol reforming over Pt/γ-Al_2O_3 in vapor and liquid phase using ATR-IR spectroscopy exhibited that CO surface species were observed as dominant surface species at 373 and 423 K.[18] In the study, the surface coverage by adsorbed CO increased as the methanol feed concentration increased due to a decrease in the number of vacant sites available for methanol to adsorb and decompose poisoned by adsorbed CO. Also, it was found that adsorbed hydrogen reduces the number of surface sites that are available

for activating methanol. Copeland et al. also found that exhibited that the decomposition of glycerol in aqueous phase over Pt/γ-Al_2O_3 produced two types of CO surface species which consist of linear CO (CO_L) and bridge CO (CO_B) on the surface at room temperature.[13]

Dumesic et al. proposed the reaction pathways[20] for APR of polyols, but the observation of surface species in addition to metal carbonyl (CO) will elucidate the complex reaction network. The reforming of ethylene glycol at 723 K and 50 bar produced methanol, ethanol, and acetic acid as by-products and IR spectrum of the spent catalyst showed adsorbed acetic acid, which was proposed as a precursor to cokes, leading to the deactivation of catalyst. a study on electrochemical glycerol oxidation in acidic media revealed that on the Pt (111) glyceraldehyde, glyceric acid, and dihydroxyacetone are products, but the only glyceraldehyde is a sole product on Pt(100). In the same study, IR spectra showed that carbonyl compounds, like aldehydes, ketones, and carboxylic acid, are formed as intermediates of the glycerol oxidation by observing a peak at 1740, 1420, and 1250 cm^{-1}.

To form metal carbonyl (C=O), the C-C bond cleavage mainly takes place on the metal sites through dehydrogenation and decarbonylation. On the other hand, dehydration primarily occurs at acidic metal oxides, leading to the C-O bond cleavage, which requires higher activation energy than C-C bond cleavage.[28, 63] Also, ethylene glycol over crystal Pt and alumina supported Pt only forms syngas via the full decomposition both at vacuum and in aqueous conditions at room temperature. Also, instead of bond breaking, glycerol on γ-Al_2O_3 in aqueous environment at room temperature is reported to form a bridging

alkoxy bond through a primary alcohol group to two coordinately unsaturated metal atoms on diverse metal oxides including Al_2O_3.[50] In our study, all oxygenates considered produced CO_L and CO_B as dominant surface species. It is well-known that the size of Pt particle mainly controls the distribution of CO_L and CO_B due to the different affinity of CO surface species to the defect and terrace sites on Pt surface.[64-65]. Since experiments were conducted with the same of the size of Pt particle supported on γ- Al_2O_3, it is highly unlikely that the different feedstocks significantly change the size of the particle during the APR at the room temperature. Therefore, any change in the coverages of CO species should be due to the types of reactants and their inhibiting effects on active sites for the formation of CO. Increase in chain-length from glycerol to sorbitol produced less formation of CO_L on Pt surface at the same temperatures, leading to the low ratio of CO_L to CO_B. Also, glucose which undergoes ring-opening before C-C bond cleavage produced less CO coverage than sorbitol. Therefore, three different oxygenates led to the different ratio of CO_L to CO_B on the same catalyst, which indicates the types of reactants also affect the types of CO surface species formed on Pt during APR.

At the lower coverage, both CO_L and CO_B occupy at Pt (335) edge sites with lower coordination number, and at the high coverage, the CO_L and CO_B start to occupy the terrace sites with high coordination number.[66] Therefore, the peak frequencies of CO_L and CO_B migrated from low to high frequency as the surface coverage of CO on Pt increase.[66] In our study, all the CO_L and CO_B formed at the lower frequency and migrated into high frequency (Table A. 1), which indicates that all of the oxygenates are decomposed on Pt surface with lower coordination number, and CO saturated the Pt surface with high coordination number at the end of aqueous oxygenate flow period. The consistent peak migration of CO_L and

CO_B frequencies regardless types of oxygenates indirectly indicates diols and sugars are more easily decomposed on Pt edge sites with low coordination number. This interpretation can be further strengthened by a DFT studies in which Pt (211) surface was calculated to have a higher activity for decomposition of ethylene glycol than Pt (111) surface.[28]

Figure 0.7 shows that immediate contact of glucose with the catalyst bed generated convoluted CO_B neighboring unreacted glucose, the gradual increase in the coverage of CO_L was observed. This observation indicates that the removal of neighboring glucose which adsorbs in a cyclic form promotes the ring opening of glucose near Pt surface to form CO on the surface via decarbonylation at the C1 position, instead of desorbing immediately by water. The correlation between the integrated area of CO_L and peak height of stretching C-O mode of the secondary carbon (2°) of glucose in the in-situ spectrum during H_2O flow period also further supports the steric effect of neighboring cyclic glucose on the formation of CO. The effect of the configurations of adsorbed glucose on the transformation of cyclic to acyclic glucose on Pt surface has not been studied so far. However, From the DFT studies, it is proposed that the ring opening of glucose is predicted to take place at C1 position mainly,[67] which indicates that glucose should approach the active sites of Pt in a favorable orientation for ring-opening. Therefore, it is plausible that steric effect of the presence of neighboring cyclic glucose prevents glucose from opening a ring structure, leading to the significantly reduced coverage of CO on Pt surface. In response to increases in temperature, the coverage of CO_L increased, which indicates that some of the sites become more available for the formation of CO at high temperatures. At lower temperatures, the decomposition of glucose produced by Pt produced much less coverage of CO_L compared to glycerol and sorbitol due to the steric effect from unopened

cyclic glucose as discussed previously. Interestingly, the steric effect which prevents glucose from opening itself and forming CO was not observed at high temperatures, leading to slightly higher coverage of CO_L than sorbitol. This result indicates the steric effect due to the neighboring glucose on Pt becomes negligible for glucose decomposition. Recent study investigated the difference activity of alcohol and aldehyde group on metal surface using glycolaldehyde as a probe molecule and found that the decomposition of glycolaldehyde on Pt(111) does not require the C-H scission step, leading to higher activity than ethylene glycol for the formation of CO.[68] At the same study, it was found the presence of C=O functionality does not significantly affect the decomposition pathways of C2 oxygenates, leading to the same product distribution as in ethylene glycol.[69] Even though glucose has more alcohol groups than glycoaldehyde, the presence of aldehyde group at C1 in glucose which would only require decarbonylation for the formation of CO is highly likely to positively affect the CO coverage at high temperatures in the absence of steric effect from the ring-opening step of glucose.

CO_L and CO_B tend to exhibit different activities for the formation and conversion into CO_2 by oxidation. In our study, CO_L and CO_B exhibited the different activity for WGS reaction in a way that only the integrated area of CO_B decreased with the same rate of disappearance regardless the types of reactants in H_2O flow period at low temperatures. This observation agrees well with the previous study where Copeland revealed that CO_B formed during APR of glycerol is only active for WGS reaction on Pt even at room temperature and the binding sites for CO_B seem to be Pt sites that H atoms preferentially also bind, leading to the competitive adsorption between CO_B and H.[13, 18] The trend observed for CO_B formed during glycerol and sorbitol flow period showed the gradual and

linear decrease both in the aqueous reactant and subsequent H_2O flow period since adsorbed hydrogen atoms from decomposition of glycerol and sorbitol prevent glycerol or sorbitol from further forming CO_B at the sites where CO_B is first oxidized via WGS reaction. However, glucose period exhibited the saturation behavior which indicates adsorbed hydrogen atoms which competitively occupy active Pt sites with CO_B less inhibited, which makes sites more available for CO_B species. The most probable source of hydrogen atoms on Pt surface is from the decomposition of glucose since the water splitting by Pt is very slow in an aqueous environment at room temperatures.[70] Hydrogen atoms should be generated at the Pt sites and need to move onto the terrace sites to preferentially block CO_B sites. The cyclic glucose on the metal support interface which preferentially consists of kinks and edge sites is relatively hard to open ring structure due to the steric effect, resulting in the decreased coverage of CO_L and relatively small effect on the coverage of CO_B. This relatively weak steric effect on terrace sites compared to the edge and kink sites near the metal-support make terrace sites more available for CO_B binding compared to the linearly-structured polyols.

The temperature increase from 50 to 72 °C significantly changed the kinetics of CO surface species in respect of oxidation of CO surface species via WGS reaction. Distinctly, the disappearance rate of CO_L after reaching noticeable high coverage from glycerol and glucose became sharper than the oxidation of CO_B in the absence of reactant during H_2O flow period. However, in our results, CO_B preferentially bound to terrace sites seemed to exhibit the reduced disappearance rate at high temperatures compared to the trend of CO_B in the H_2O period at low temperatures. This result may indicate that the activation energy barrier of CO_L was reduced at high temperatures. There are many studies on changes in

activation energy for CO oxidation depending on the coverage. For example, at high coverage, the coverage of CO on Pt surface affects the rate of oxidation of CO since the CO-CO interactions within closely packed adsorbates often cause the ordering and oscillatory behavior of Pt single crystals, leading to a significant drop in activation energy for CO oxidation.[71] Also, recent studies show that intrinsic non-uniformity of Pt crystals cause minor catalytic consequences when the surface is fully saturated with CO.[72] However, increase in temperature is not allowed to preferentially increase the oxidation rate of CO_L with high activation energy and at the same time, decrease the oxidation rate of CO_B with low activation energy. Therefore, this coverage-dependent activation energy for CO species cannot be directly applied to interpret the current observation. Therefore, instead of the direct oxidation of CO_L to CO_2 via WGS, we propose the transformation of CO_L into CO_B as an initial step, and then CO_B undergoes WGS reactions. The rate of disappearance of CO_B was much sharper at 72 than 24 and 50 °C, but the rate decreased sharply when aqueous reactant flow changed to pure H_2O flow period. It is reported that strong CO_L is significantly unstable at high converges due to the dipole-dipole coupling of CO_L.[71]. It is known that water can induce the interchange between CO_B and CO_L.[73] Therefore, the sharp drop of CO_L coverage coupled with almost constant coverage of CO_B during H_2O flow period may be a consequence of the two-step oxidation of CO_L to CO_2 by water. Although this interpretation agrees well the observations, further experiment is required to confirm the two-step mechanism of WGS reaction on CO surface species on Pt particles.

Our study indicates that a shorter-chain length polyol is efficient in forming CO on metal particles. However, this efficiency cannot be directly applied to reaction yield since

it must deal with CO poisoning during the reaction, which requires high operation temperature in the reactor for the oxidation of CO via WGS reaction. However, it is reasonable assumption that the reduced coverage when using the polyols with a high number of carbons in the backbone affects the yield and selectivity and H_2 production when considering WGS reaction as a rate-limiting step during APR reaction.

1.8 Conclusion

We studied the effect of size and functionality of biomass-derived oxygenates on the formation of surface species on 5 wt% Pt/γ-Al_2O_3 in aqueous phase reforming (APR) reaction using in-situ ATR-IR spectroscopy. Specifically, kinetics of formation and conversion of linearly bound and bridging CO from glycerol, sorbitol, and glucose are studied at different temperatures. Regardless types of reactant, the formed CO_B from the decomposition of the reactants is more susceptible to WGS reaction, but increasing temperature from room temperature to 72 °C for APR reaction induced inactive CO_L to start to undergo oxidation via WGS reaction. Interestingly, the reforming of glucose exhibited significantly reduced conversion into CO surface species on Pt due to the steric effect in the presence of neighboring acyclic glucose. The unreacted portion of glucose readily converted into CO surface species when acyclic glucose near the Pt surface is absent. Also, compared to the fresh catalyst for reforming reaction of polyols and sugars, the second use of the catalyst when the temperature reached at high temperatures (72 °C) generated the formation of CO surface species. This phenomenon is highly likely to be related to the accumulation of unreacted portion surface intermediates decomposed from at the interface between Pt and alumina support.

Investigate Adsorption of C3 Oxygenates on Heteroatom (Sn, Mo, and W) doped Beta Zeolites and the Effect of Water using Infrared Spectroscopy

1.9 Introduction

Biomass conversion over heterogeneous catalysts is a candidate to build economical and energy-efficient processes for the sustainable production of fuels and chemicals since they are more easily recovered than homogeneous catalysts. In contrast to petroleum feedstocks, biomass-derived oxygenates contain a high extent of functionality (e.g., -OH, -C=O, -COOH). Therefore, the development of solid catalysts to selectively convert the biomass-derived oxygenates with having a high degree of functionality into value-added products in the condensed phase is thereof of considerable interest. In this respect, recently, metal centers incorporated into the framework of zeolites have been studied as solid Lewis acid catalysts such as TS-1 and Sn-grafted MCM-41 due to their ability to activate carbonyl functional groups in oxygenates.[74-75]

Beta zeolites, which incorporate metals such as Ti, Hf, Zr, Nb, Ta, and Sn as framework atoms, have exhibited high activity for the inter- and intramolecular Meer-wein−Ponndorf−Verley (MPV) reduction of aldehydes and ketones,[76-78] the Baeyer−Villiger oxidation of ketones to lactones,[79-81] the isomerization/epimerization of glucose,[82-86] C-C coupling,[87-92] and hydrogen transfer reactions.[93-95] It has been reported that there are two types of framework Sn sites, one consisting of $Sn(-Si-O-)_4$ (closed sites)

and the other one having one of the Sn−O−Si bonds hydrolyzed to generate a (−Si−O−)-$_3$Sn−OH site (open sites). The open sites have been suggested to be more active than the closed sites for the Baeyer−Villiger and Meerwein−Ponndorf−Verley reactions.[96-97] Despite these increasing number of applications of Lewis acid zeolites, there still exist many open questions about these materials dues to the lack of fundamental understanding of the nature of their active sites.

A significant advance in the characterization of Brønsted sites associated with framework Al in silica zeolites came when observing that many adsorbates form distinct surface complexes with the acid sites.[98-99] Spectroscopic techniques to investigate the reactivity of various complexes were useful for understanding reactions at the acid sites and for predicting the chemistry of other molecules.[98-99] Therefore, the proper choice of probe molecules that have similar functionality to biomass-derived oxygenates can enable studies of surface reactions to contribute the understanding the molecular configuration of adsorbed surface reactant and formed intermediates surface on the active sites. However, only a few studies probed the active sites of beta zeolites with probe molecules to understand the chemistry taking place in solid Lewis acid catalyst. In one of a few studies, IR spectra of pyridine adsorption was used to correlate the frequencies of adsorbed pyridine on different Lewis acid sites (i.e., Ti, Zr, Nb, Ta, Sn, Ga, and Al-beta) with the Lewis acid strength, but exhibited the limited reliability due to a narrow range of peak frequencies from 1445 to 1454 cm^{-1}.[100-102] Another study used temperature-programmed desorption (TPD) and thermogravimetric analysis (TGA) and found that acetonitrile and diethyl ether formed 1:1 complexes with Sn sites in beta zeolites and decomposed reversibly upon mild heating in vacuum.[14] In the same study, 2-methyl-2-propanol underwent dehydration to

butene and water over a very narrow temperature range centered at 410 K over Sn BEA. These studies were helpful to predict the characteristics of Lewis acidic beta zeolites using simple oxygenates.

The configuration of adsorbed species and its reactivity of oxygenates depends on the type of heteroatoms incorporated into beta zeolites, leading to the possibility that we can tune the strength and size of Lewis acid sites by the identity of heteroatoms into the beta zeolite topology.[103] The catalytic activity of a Lewis acid for oxidation relies on its ability to form acid-base adducts with the substrate. This indicates that effective electron transfer from Lewis base to the Lewis acid, which is proportional to the energy difference and degree of overlap between the occupied orbitals of the base and the empty orbitals of the acid, is important for the activity.[104] Another factor to consider the acid-base interaction for Lewis acid chemistry is the HSAB (hard–soft acid–base) principle where hard acids coordinate preferentially to hard bases and soft acids with soft bases.[105] Also, the size of metal incorporated into beta zeolites was reported to play a role in the isomerization of glucose. Many metal chlorides as homogeneous catalysts catalyze the isomerization of glucose into mannose through competing pathways including 1,2 hydride transfer and the Bilik reaction.[106] Angyal suggested that $Ca(OH)_2$ and $La(OH)_3$ is highly active for glucose epimerization, since Ca^{2+} and La^{3+} have an ionic radius (0.99 and 1.05 Å, respectively) that was optimum to form a stable complex with the sugar substrate, while the inactive metal hydroxides, which have either too small or too big are inactivity.[107] When considering a possibility of tuning the properties of Lewis acidic zeolites by incorporating metals into the zeolite topology,[103] systematic approach toward finding a correlation of the properties of Lewis acid center such as electronegativity, hardness of Lewis acid, and size of metal

with the types of adsorbates and its configuration will contribute to the understanding of Lewis-acid catalyzed biomass conversion. Furthermore, this information will be quickly transformed into database to predict chemistry in biomass upgrading using various Lewis acidic micro- and mesoporous materials.

Transformation of biomass often operates at a low temperature in the liquid phase where complex solute-solvent-catalyst reaction networks exist.[41] Sn BEA was reported to undergo a structural change of Sn active sites from tetrahedral to octahedral coordination in the presence of water when two H_2O molecules are coordinated with Sn sites.[91] The hydrophobicity of defective Sn beta prepared in a hydrothermal method often exhibited much higher yield and selectivity than Sn beta prepared using the post-synthetic method with abundant of silanol nest, which indicates that water inside pore of zeolites negatively affects the activity of Sn sites.[108] In addition to suppressing reactivity, solvent can also catalyze reactants to take a different reaction path over the same metal sites. For example, Sn-BEA catalyzes glucose−fructose isomerization via a 1-2 intramolecular hydride shift in water and glucose−mannose epimerization via a 1,2 intramolecular carbon shift in methanol.[84] These observations motivate to examine the configuration of adsorbed surface species in the presence of water and methanol as prototypical solvents.

In this work, we incorporate group VI (Mo and W) and XIV (Sn) metal atoms into the framework of beta zeolite. These metals have different electronegativities, Lewis acid hardness, and ionic radii. We investigate the properties of the Lewis acid sites in the three solid acid catalysts with model oxygenates (acetone, and hydroxyacetone) using high vacuum transmission FT-IR spectroscopy. These results allow us to deduce the dominant properties of active metal sites that control the activity of aldol-condensation and 1-2

hydride shift in these materials. Lastly, we address the effect of types of solvent on the configuration of adsorbed species from acetone and hydroxyacetone to provide insight into the choice of solvent for this class of catalysts.

1.10 Experimental Methods

1.10.1 Material Synthesis

Ammonium BEA, obtained from Zeolyst (CP814E*, Si/Al = 25) was calcined at 550 °C (ramp 3 °C/min, hold 6 h) to obtain HBEA. Then, 15 g of HBEA was dealuminated by refluxing in 13 M HNO_3 (20 mL acid/g of HBEA, prepared using 70 wt% nitric acid from Sigma Aldrich and 18.2 MOhm water) for 20 h. The mixture was then diluted to 1 L with 18.2 MOhm water, and then vacuum filtered and washed with 18.2 MOhm water until the filtrate was neutral. Then, the deAlBEA was dried overnight at 110 °C, collected, and once again dealuminated/filtered/dried using the same procedure.

To synthesize Sn, Mo, and W incorporated into BEA, 2 g of the deAlBEA was dried under vacuum at 150 °C overnight, brought into the glovebox under vacuum, and then physically mixed and ground in an agate mortar for 15 min with the appropriate precursor to produce the desired wt% of Sn, Mo, or W supported on BEA. $Sn(OAc)_2$ from Sigma Aldrich, $Mo_2(OAc)_4$ from Strem Chemicals, and $WOCl_4$ from Sigma Aldrich were used as the precursors.

The mixture was then loaded into a quartz tube with a two-neck adapter and taken out of the glovebox still under N_2. Then, the mixtures were heated either to 500 °C (Mo, W) or 550 °C (Sn) (2 K/min, hold at temp for 12 h) under 150 mL/min flowing Argon

(UHP, Airgas). After these 12 h, the flow was then changed to 150 mL O_2 (UHP, Airgas), and the materials were calcined for 3 h. After this, the materials were exposed to air for the first time and packed into vials for sending.

1.10.2 Catalyst Characterization

X-ray diffraction (XRD) patterns of 5 wt% Pt on γ-Al_2O_3 were obtained with a Philips X'pert diffractometer using an X'celerator module using Cu Kα radiation. Diffractograms were collected at incident angles from $2\theta = 5°$ to 70° with a step size of 0.0167°. Nitrogen physisorption measurements were taken using a Micromeritics ASAP 2020 Physisorption Analyzer. Samples were degassed under vacuum at 250 °C for 4 h prior to analysis. The surface area of the sample was calculated from the adsorption isotherm in the region $0.05 < P/P_0 < 0.3$, based on the BET method[52]. The BJH method[53] was also adopted to calculate average pore diameters of the sample in the region $0.05 < P/P_0 < 0.99$. Pyridine adsorption followed by IR spectroscopy was performed using a Thermo-Nicolet 8700 FT-IR spectrometer with an MCT/A detector. For every spectrum, 64 scans were accumulated at a resolution of 4 cm^{-1}. The sample was pressed into the self-supported wafer and then mounted into a custom-built vacuum chamber with ZnSe window. The activation of the catalyst wafer was conducted at 500 °C at $< 10^{-6}$ mbar for 12 h, and a background spectrum was taken after lowering the temperature to 150 °C. Pyridine was introduced into the chamber at a partial pressure of 0.1 mbar for 30 min. The spectrum for pyridine adsorption were taken after the chamber was evacuated for 30 min. After the experiment, the density of the catalyst wafer was determined by weighing a cutout of the wafer with a diameter of 6.35 mm (1/4 inch). The concentration of Lewis and Brønsted acid sites was

determined by integrated area of the peaks of chemisorbed pyridine and pyridinium ions around 1445 and 1540 cm^{-1}, respectively, the calculated density of the wafer, and the molar extinction coefficient of the catalyst. The molar extinction coefficients were taken from Datka et al.[54]

1.10.3 FT-IR spectroscopy

Each zeolite sample was pressed into a self-supported wafer and loaded into a transmission vacuum chamber. The sample was activated at 450 °C for 1 h under high vacuum conditions and was cooled down to 50 °C. A background spectrum was collected. Acetone or hydroxyacetone was introduced into the chamber as vapors at 0.1 mbar through a leak valve for 30 min. Afterward, the cell was evacuated for 1 h, and a spectrum was collected. The sample was then heated at 80, 120, 350 and 450 °C for 1 h, and a spectrum was collected at 50 °C.

All spectra were collected using a Nicolet 8700 FTIR spectrometer with an MCT/A detector. For each spectrum, 64 scans were recorded at a resolution of 4 cm^{-1}. All spectra were collected using a Nicolet 8700 FTIR spectrometer with an MCT/A detector. Thermo Fischer Scientific Inc. Grams 9.1 software was used to process the collected spectra

1.11 Results

1.11.1 Characterization

Inductively coupled plasma atomic emission spectroscopy (ICP-AES) analysis showed that the dealuminated BEA had a minimal Al content ($SiO_2/Al_2O_3 > 1000$), which indicates that that extra-framework aluminum does not exist in the sample which is used

to prepare Sn, Mo, W BEA. The synthesized Sn, Mo, W BEA contained 2.09, 2.17, and 1.41 wt. % of the substituted metals based on ICP-AES analysis.

Based on pyridine adsorption at 150 °C followed by IR spectroscopy, Sn, Mo, and W BEA exhibited Lewis acid site (LAS) concentrations of 195, 181, and 152 mol/g, respectively (Figure 0.1). We designate acid sites that can retain pyridine at 450 °C as strong acid sites. The concentration of strong acid sites followed the order Sn BEA > Mo BEA > W BEA. The concentrations of Brønsted acid sites (BAS) in the samples were negligible compared to the concentrations of LAS (Figure 0.1). The dealuminated beta zeolites, which was used to prepare Sn, Mo, and W BEA using the post-synthetic method, did not exhibit any measurable LAS or BAS sites even at 150 °C.

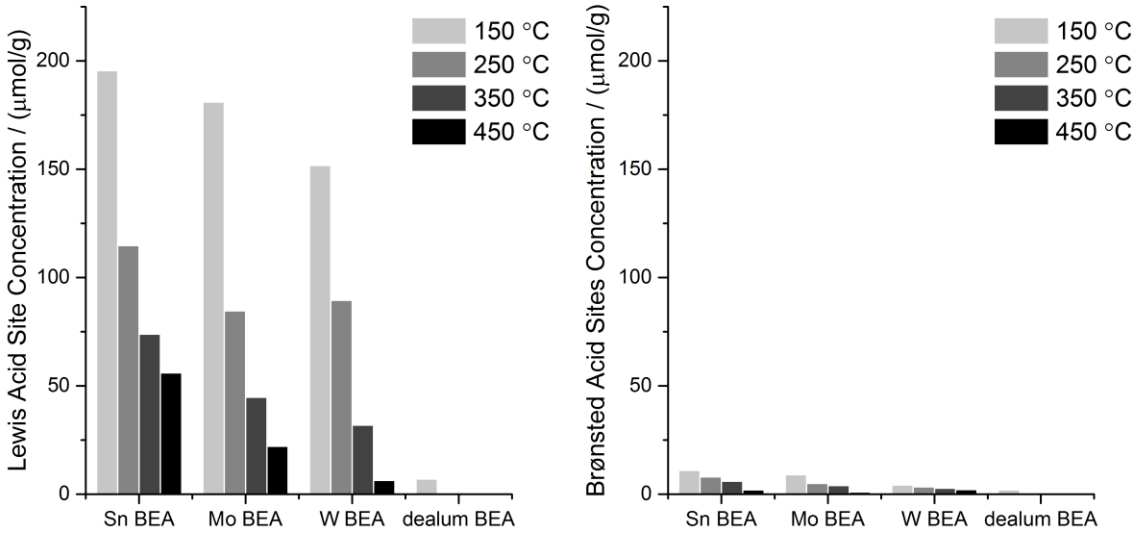

Figure 0.1. Lewis acid site concentrations of the beta zeolites measured by pyridine adsorption followed by IR spectroscopy.

Previous studies characterized the strength of Lewis acid sites by adsorption of acetonitrile-*d*3 followed by FT-IR spectroscopy.[14, 109] Unlike Sn in the zeolite framework, acetonitrile-*d*3 interacting with extra-framework Sn sites does not produce any υ(C−N) peaks in the spectral region between 2200 and 2400 cm^{-1} since due to the weak interaction acetonitrile with acid sites of SnO_x.[14] The spectra of Sn, and Mo BEA contained distinct υ(C−N) peaks at 2310 and 2303 cm^{-1} that are attributed to acetonitrile-*d*3 interacting with the LAS of the zeolites (Figure 0.2a and b).[14, 110] The signal at 2275 cm^{-1} is due to acetonitrile interacting with silanol groups.[14, 110] Interestingly, Figure 0.2c shows that υ(C−N) peak from acetonitrile-*d*3 on LAS of W BEA was not observed due to the weak interaction of acetonitrile-*d*3 with W sites in beta zeolites. During the desorption of acetonitrile under dynamic vacuum conditions (Figure B.2), acetonitrile is more easily removed from Mo BEA than from Sn BEA, but acetonitrile adsorbed on Sn and Mo BEA was not removed completely within 150 min. The peak intensity of acetonitrile adsorbed on W BEA was significantly reduced within 30 min due to the low strength of the LAS.

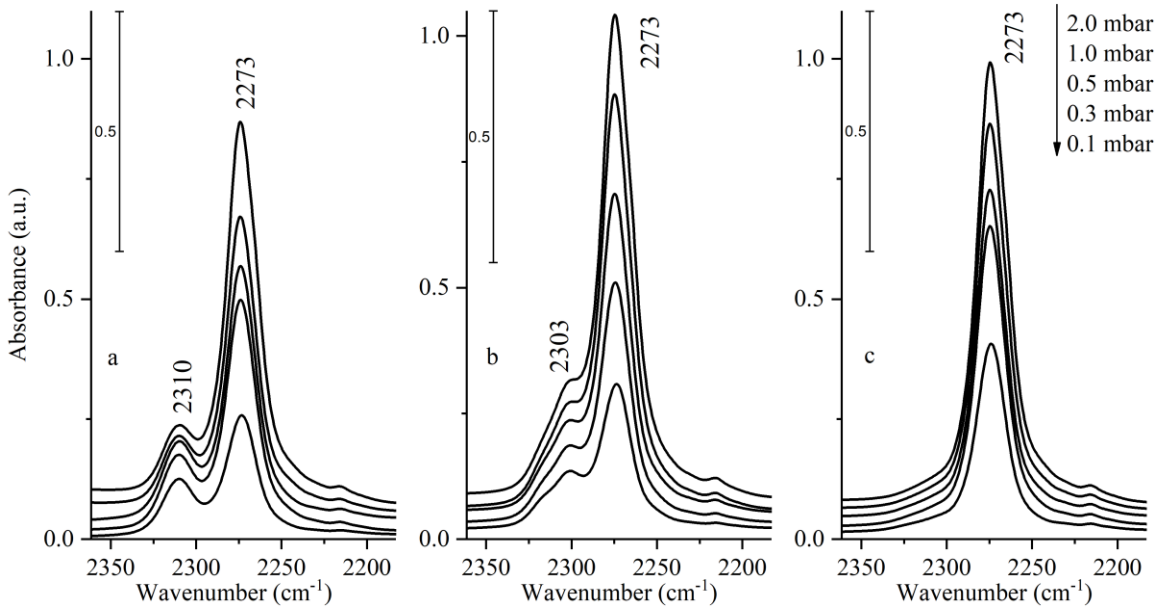

Figure 0.2. FT-IR spectra of deuterated acetonitrile a) Sn BEA, b) Mo BEA, and c) W BEA at increasing acetonitrile coverage.

1.11.2 Adsorption of acetone and hydroxyacetone on Snβ and followed by TPD

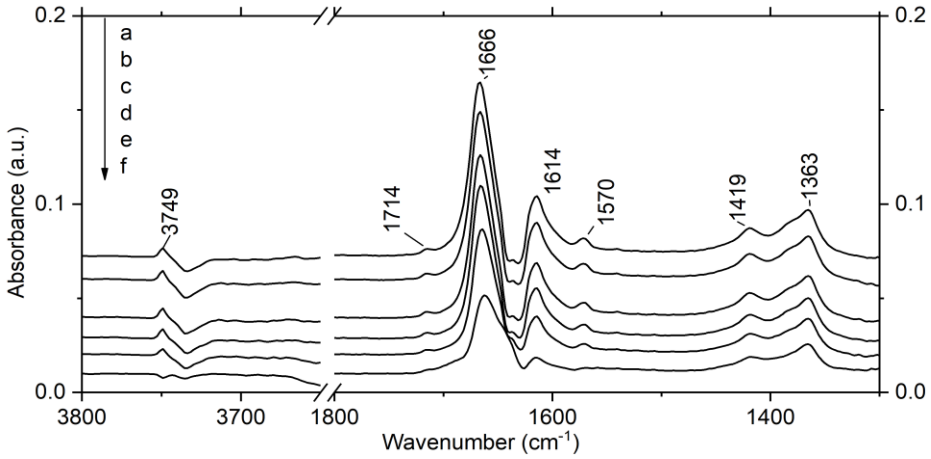

Figure 0.3. FT-IR spectra of surface species formed acetone (<10^{-2} mbar) on Sn BEA at (a) 50 °C HV (b) 80 °C (c) 120 °C HV (d) 200 °C HV (e) 300 °C HV (f) 400 °C HV.

Figure 0.3 shows the IR spectra obtained by dosing a low amount of acetone (<10^{-2} mbar) onto Sn BEA. The spectrum of acetone on Sn BEA did not contain characteristic mode for physisorbed acetone and acetone associated with silanol groups that were observed at 1707 and 1689 cm^{-1} for acetone on dealuminated BEA (Figure B. 3). This shows that small amounts of acetone are quantitatively chemisorbed on the Sn sites. It is well established that acetone formed MO and phorone through self-aldol condensation reaction and can form mesitylene and isophorone via subsequent dehydration and dehydrogenation over various types of catalyst including metal oxides and zeolites.[46, 111-117] In particular, the adsorption of mesityl oxide (MO) on Lewis acidic solid catalysts, such as nano-sized alumina and zeolites (USY), produced peaks of υC=O vibrations at 1673 and

υC=C vibrations at 1603 cm^{-1}.[112] Figure 0.3 shows that the most pronounced modes in the range of characteristic carbonyl and CC double bond stretching bands were observed at 1666 cm^{-1} and 1614 cm^{-1} when acetone interacted with Sn BEA. Therefore, those modes can be attributed to υC=O and υC=C vibrations of mesityl oxide formed from acetone. Also, a mode 1570 cm^{-1} is assigned to the enolate of acetone on the surface.[111, 115-116, 118-119] The peak at 3749 cm^{-1} is due to the formation of a Si-OH group from α-abstraction of acetone by an O atom bound to a Sn atom.[120] In the spectrum taken during TPD of the spectrum (Figure 0.3), no additional surface species were formed on the Sn sites. Mesityl oxide was firmly bound to Sn sites, and the corresponding peaks remained up to 400 °C.

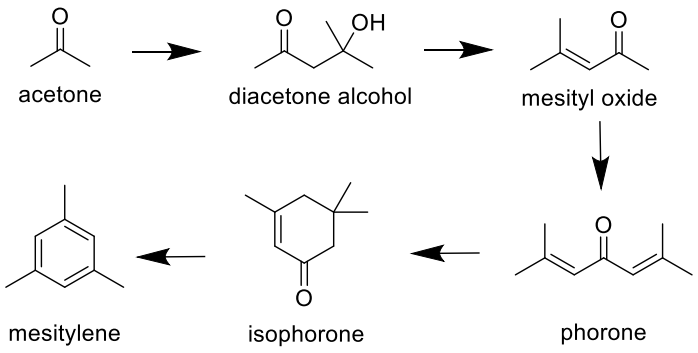

Scheme 0.1. General feature for the aldol condensation reaction for acetone.

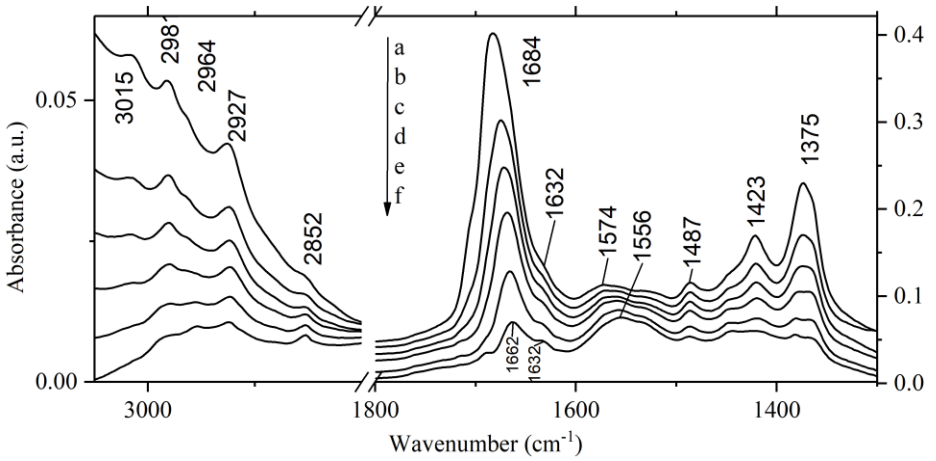

Figure 0.4. FT -IR spectra of surface species formed acetone (0.1 mbar) on Sn BEA at (a) 50 °C HV (b) 80 °C (c) 120 °C HV (d) 200 °C HV (e) 300 °C HV (f) 400 °C HV.

When the partial pressure of pressure of acetone was increased to 0.1 mbar, adsorbed acetone, as well as various other adsorbed species formed on Sn BEA (Figure 0.4). The asymmetric and symmetric υCH_3 bands of acetone were observed at 3015 and 2927 cm^{-1} as well as modes of 1421 and 1375 cm^{-1} due to $\delta_{as}CH_3$ and δ_sCH_3.[46, 121] By comparing the spectra of acetone on Sn BEA in Figure 0.4 and spectra of acetone on dealuminated BEA in Figure B. 3, we were able to locate various stretching modes of the carbonyl groups of physisorbed acetone, acetone bound to the silanol group, and mesityl oxide. Figure 0.4 exhibited a strong band at 1684 cm^{-1}, which can be attributed to the convolution of multiple bands acetones and generated adsorbates formed from acetone at 50 °C. Based on the deconvolution method, the $\upsilon C=O$ region was deconvoluted into peaks at 1705, 1682, and 1663 cm^{-1}, which are attributed to physisorbed acetone, acetone which interacts with silanol groups, and a carbonyl group of mesityl oxide formed on Sn sites.[112] The enol form of acetone, an intermediate surface species to form mesityl oxide, was

observed based on its υC=C mode at 1576 cm^{-1}.[111, 115-116, 118-119] Also, asymmetric and symmetric νCH_2 vibrations of the enol were observed at 2981 and 2852 cm^{-1}.[115-116]

During TPD following the exposure of the catalyst wafer to 0.1 mbar of acetone, the stretching vibration of C=C double bond became more pronounced, while the frequency of the peak decreased (Figure 0.4). At the same time, a carbonyl stretching vibration red-shifted from 1683 to 1662 cm^{-1} as temperature increased. At 120 °C, a carbonyl stretching vibration was observed at 1672 cm^{-1} due to the increasing coverage of mesityl oxide coupled with decreasing coverage of acetone. Mesityl oxide is known to be reactive towards aldol condensation,[113] such as the reaction with acetone to form phorone, which is reactive precursor for the formation of isophorone, and mesitylene as seen Scheme 1.[112] Thus, the increasing intensity of C=C double bond can be attributed to the formation of these highly conjugated oxygenates.[122] Figure B. 4 shows that acetone was depleted over Sn BEA around 120 °C. Once mesityl oxide formed from acetone at low temperatures, the peak for mesityl oxide kept decreasing due to the conversion into bigger molecules, possibly phorones, isophorones, and aromatics, and cokes at high temperatures.[112]

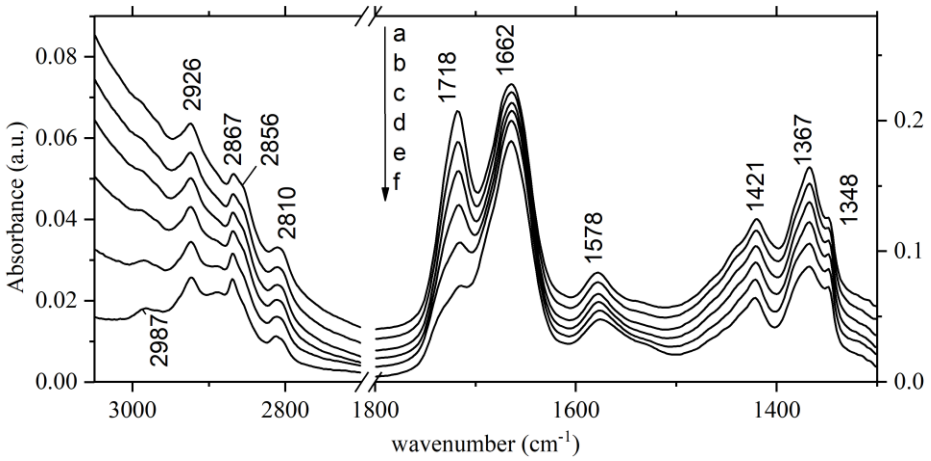

Figure 0.5. FT-IR spectra of adsorbed hydroxyacetone (0.1 mbar) over Sn BEA at (a) 50 °C HV (b) 80 °C (c) 120 °C HV (d) 200 °C HV (e) 300 °C HV (f) 400 °C HV.

The spectrum of adsorbed species formed from hydroxyacetone on Sn BEA at 50 °C exhibited $\nu_{asym}CH_3$ and $\nu_{sym}CH_3$ peaks at 2926 and 2867 cm^{-1} as well as a νC=O mode at 1718 cm^{-1} (Figure 0.5a). To identify a band at 1662 cm^{-1}, 1-propanol was adsorbed on Sn BEA and a band at 1662 cm^{-1} was observed, which is attributed to the νC=O of propionaldehyde which is formed on Sn sites by dehydrogenation of 1-propanol (Figure B. 6). The combination of the characteristic peak of the C-H stretching vibration of the aldehyde at 2810 cm^{-1} an the νC=O mode of the aldehyde at 1662 cm^{-1} indicate that 1-hydroxypropanal was formed.[59] A νC=C mode was also observed at 1578 cm^{-1} due to the formation of an enol, which is likely propene-1,2-diol.[12] The enol was formed by tautomerization. The corresponding peak maintained its intensity up to 400 °C.

Increasing temperature during the TPD of adsorbed hydroxyacetone did not produce any distinct adsorbates in response to increasing temperature, which indicates that the surface species formed from hydroxyacetone on Sn site are stable, but νO-H peaks of

free silanol groups were observed at 3700 and 3740 cm^{-1}. Therefore, in contrast to the acetone adsorption, νC=O vibration of hydroxyacetone and 2-hydroxypropanal hold the peak positions at 1718 and 1662 cm^{-1} during increasing temperature up to 400 °C. However, the intensity of the νC=O mode of 2-hydroxypropanal decreased only by 15%, but the intensity of the νC=O mode of the hydroxyacetone interacting with silanol group at 1718 cm^{-1} showed a significant decrease of 43% (Figure B. 7).

1.11.3 Adsorption of acetone on Sn BEA in the presence of water

To investigate the effect of water on the adsorbed products from acetone, H_2O vapor was dosed into the cell at 1 mbar after Sn BEA was saturated with 0.1 mbar of acetone at 1 h. Although the CH stretching region of the spectrum was obscured by the broad peak of hydrogen bonding OH groups including H_2O, Figure 0.6 shows that the modes of acetone and mesityl oxide at 1687 and 1668 cm^{-1} did not change by the introduction of water except a mode of δOH at 1620 cm^{-1} from H_2O due to the adsorbed water. However, in contrast to the further reaction of adsorbates in the absence of H_2O vapor during TPD (Figure 0.4), Figure 0.6 shows that increasing temperature did not produce any broad peak between 1575 and 1500 $cm^{-1}$where vibrations of conjugated C=C bonds of products from acetone adsorption at high temperatures were observed during the reaction of acetone on Sn BEA (Figure 0.4).[123]

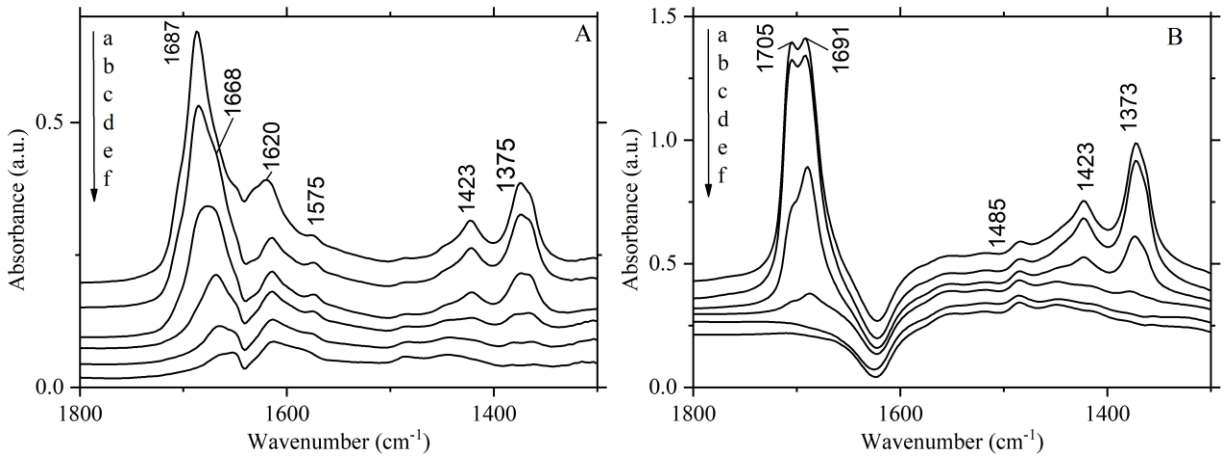

Figure 0.6. FT-IR spectra of (A) adsorbed acetone and subsequent saturation at 1 mbar of H_2O over Sn BEA (B) adsorbed acetone over hydrated Sn BEA at (a) 50 °C (b) 80 °C (c) 120 °C (d) 200 °C (e) 300 °C (f) 400 °C.

To investigate the effect of hydrolyzed Sn sites on the adsorption of acetone as an initial step for the interaction between acetone and Sn sites, Sn BEA was saturated at 1 mbar of H_2O for 1 h and subsequently, 0.1 mbar of acetone was dosed. IR spectra in Figure 0.6B exhibited two bands of νC=O modes at 1705 and 1693 cm^{-1}, which can be attributed to physisorbed acetone on Sn BEA and acetone interacting with silanol groups (Si-OH), respectively. This observation indicates that H_2O competes with acetone for Sn sites. Noticeably, the υC=C mode of the corresponding enol was not present in the spectrum of acetone on hydrolyzed Sn BEA, which indicates that the presence of water also suppresses the tautomerization of acetone.

1.11.4 Adsorption of hydroxyacetone in the presence of water

Adsorbates formed from hydroxyacetone on Sn BEA were affected by the presence of water. Figure 0.7A shows a band at 1667 cm^{-1} that was assigned to the νC=O mode of

the aldehyde group in 2-hydroxypropanal, which interacts with Sn sites. It red-shifted to 1653 cm^{-1}. The peak at 1689 cm^{-1} was present when hydroxyacetone was adsorbed on dealuminated BEA (Figure B. 5), so this peak can be attributed to νC=O of an unreacted chemisorbed hydroxyacetone to silanol groups.[12] The band at 1578 cm^{-1} is attributed to the νC=C vibration of 1,2 propenediol and did not shift in the presence of water, but the intensity of the peak was reduced compared to the spectrum in the absence of water (Figure 0.5). A noticeable effect of water during the TPD is that the various peaks of hydoxyacetone were absent on Sn BEA, which indicates that water significantly reduced the affinity between hydroxyacetone adsorbates and Sn metal sites (Figure 0.7A). Also, the peak intensity of hydroxyacetone bound to silanol group (-Si-OH) at 1689 cm^{-1} rapidly decreased in the presence of water.

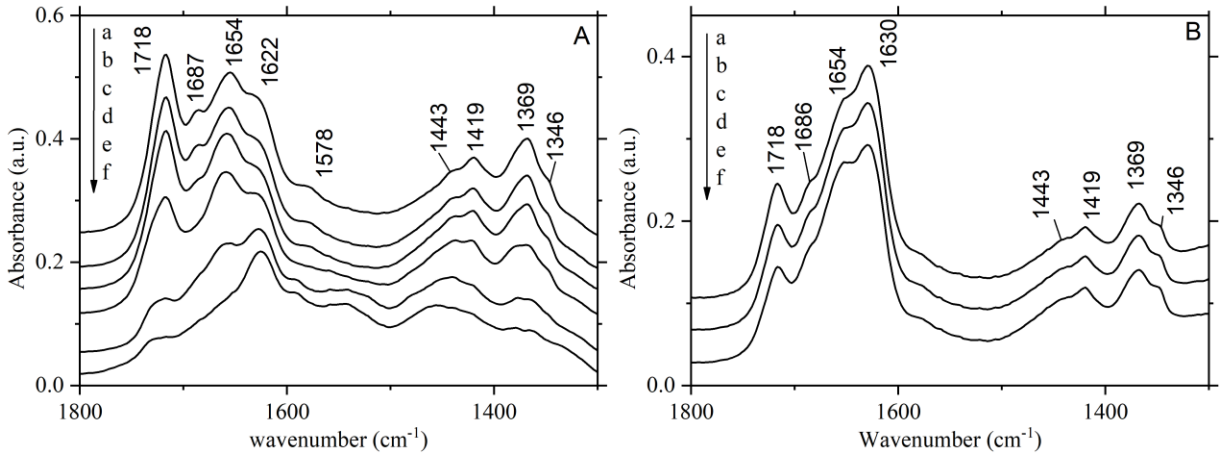

Figure 0.7. IR spectra of (A) adsorbed hydroxyacetone and subsequent saturation at 1 mbar of H_2O over Sn BEA (B) adsorbed hydroxyacetone over hydrated Sn BEA at (a) 50 °C (b) 80 °C (c) 120 °C (d) 200 °C (e) 300 °C (f) 400 °C.

To investigate the effect of hydrolyzed Sn sites on the adsorption of hydroxyacetone as an initial step, hydrated Sn BEA was prepared and similar surface species were observed as for hydroxyacetone on dry Sn BEA (Figure 0.7B). However, the C=C stretching vibration of the enol was not observed.

1.11.5 Adsorption of acetone and hydroxyacetone on Mo BEA and W BEA

Figure 0.8 shows the IR spectra obtained after adsorption of 0.1 mbar of acetone on W BEA followed by TPD. The υC=O mode of acetone exhibited a small red-shift from 1689 to 1687 cm^{-1} when compared to corresponding mode of acetone on the silanol groups on dealuminated BEA (Figure B. 4). The small shift indicates a weak interaction between the carbonyl group and the W active site. Spectra (Figure B. 5) taken after the catalyst was saturated with acetone for 1 h before desorption of the catalyst at dynamic vacuum contained a peak 1585 cm^{-1}, which is attributed to C=C of 2-propenol formed by tautomerization of acetone. However, the immediate desorption of this enol species from W BEA was observed upon evacuation, which indicates that the bond of the enol to the W active site is also weaker than that to a Sn site as seen in Figure 0.5.

Figure 0.9 shows that spectra of adsorbed species from acetone on Mo BEA exhibited only chemisorbed acetone on Lewis acidic sites which is a similar trend as in the case of W BEA, but the C=C vibration of the enol remained under dynamic vacuum at temperatures up to 80 °C. However, this peak readily disappeared at high temperatures.

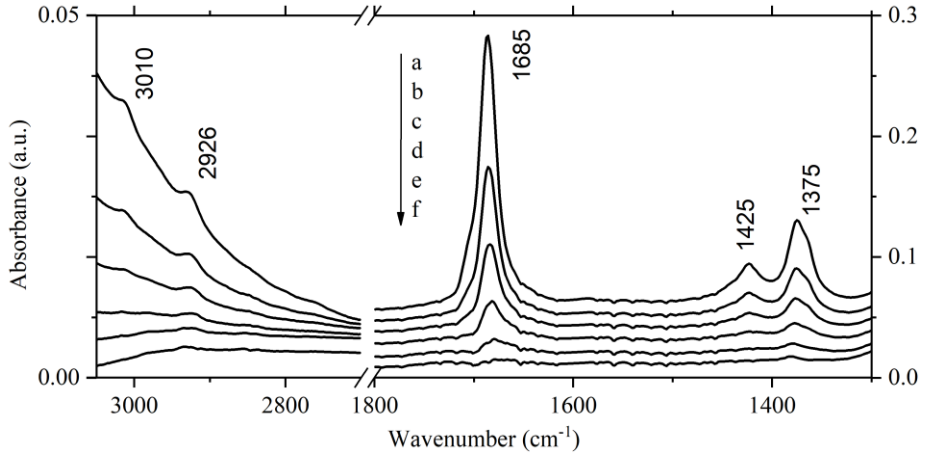

Figure 0.8. FT-IR spectra of surface species formed acetone (0.1 mbar) on W BEA at (a) 50 °C HV (b) 80 °C (c) 120 °C HV (d) 200 °C HV (e) 300 °C HV (f) 400 °C HV.

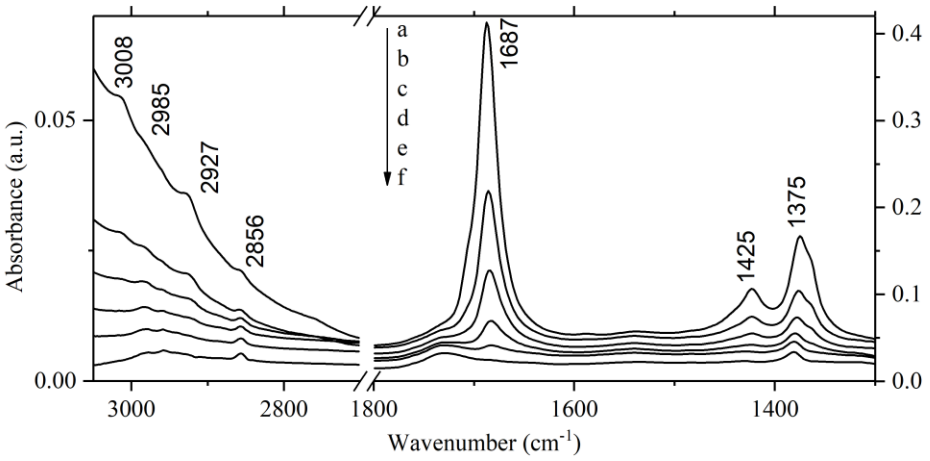

Figure 0.9. FT-IR spectra of surface species formed acetone (0.1 mbar) on Mo BEA at (a) 50 °C HV (b) 80 °C (c) 120 °C HV (d) 200 °C HV (e) 300 °C HV (f) 400 °C HV.

Figure 0.10 shows that the adsorption of hydroxyacetone on W BEA resulted in $\delta_{asym}CH_3$, ωCH_3, $\delta_{asym}CH_3$, and δOH vibrations at 1442, 1410, 1368, and 1290 cm^{-1}, respectively, as well as a $\upsilon C{=}O$ mode at 1715 cm^{-1}. A comparison with the $\upsilon C{=}O$ vibration

of hydroxyacetone on dealuminated BEA at 1716 cm^{-1} indicates that hydroxyacetone did not interact with W sites in a strong enough way to polarize the carbonyl group. In agreement with this, an increase of the temperature to 400 °C resulted in desorption of the adsorbed hydroxyacetone without the formation of any noticeable species in the process.

The spectrum of surface species (Figure 0.11) form hydroxyacetone on Mo BEA contained a νC=O peak at 1706 cm^{-1} that is the keto group interacting with the acidic Mo site (Figure 14).[124] A shoulder at 1676 cm^{-1} is assigned to the aldehyde group of hydroxypropanal that was formed via 1-2 hydride shift. This peak assignment was further supported by the observation of a νC=O band at 1682 cm^{-1} when 1-pronanol was adsorbed on Mo BEA (Figure B. 11) and produced 1-propanal via dehydrogenation.

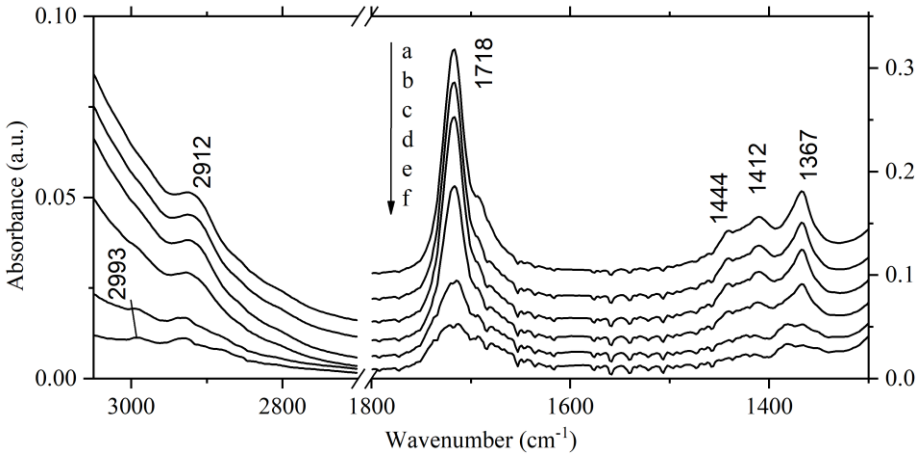

Figure 0.10. spectra of surface species formed hydroxyacetone (0.1 mbar) on W BEA at (a) 50 °C HV (b) 80 °C (c) 120 °C HV (d) 200 °C HV (e) 300 °C HV (f) 400 °C HV.

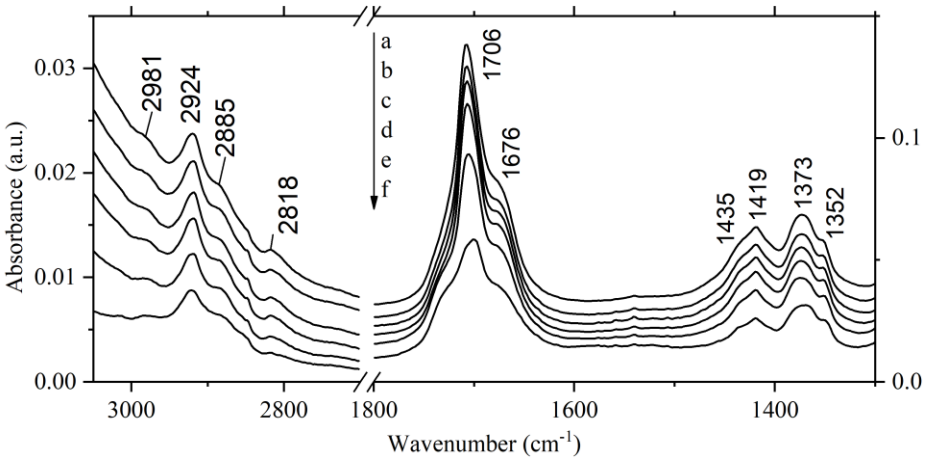

Figure 0.11. spectra of surface species formed hydroxyacetone (0.1 mbar) on Mo BEA at (a) 50 °C HV (b) 80 °C (c) 120 °C HV (d) 200 °C HV (e) 300 °C HV (f) 400 °C HV.

1.12 Discussion

1.12.1 Surface species derived from acetone via aldol condensation

In recent a few years, it is found that heteroatom-doped zeolites such as Sn BEA catalyze biomass-derived oxygenates to undergo C-C bond formation. For example, Sn BEA exhibits activity for catalyzing the self-aldol condensation of glycolaldehyde, leading to the formation of methyl vinyl glycolate and methyl lactate at 160 °C and methyl 2-hydroxy-4-methoxy butanoate as the major product at low temperatures.[95] In another study, the C-C coupling between 1,3-dihydroxyacetone and formaldehyde into α-hydroxy-γ-butyrolactone was reported to take place over Sn BEA by soft enolization of DHA followed by aldol addition of formaldehyde to the Sn-enolate intermediate, generating erythrulose as an intermediate species.[87] In the following study, it was demonstrated that Hf BEA, Sn BEA, and Zr BEA are active solid catalysts to promote the cross-aldol condensation reaction of aromatic aldehydes with acetone under mild reaction

conditions.[125] Also, isotopic labeling studies suggested that acid-base pairs (Sn and neighboring oxygen) in the framework of beta topology activate acetone by abstracting an α-proton to the zeolite lattice to promote keto-enol tautomerization for cross-aldol condensation with aromatic aldehydes.[125] These observations leads to the conclusion direct aldol condensation reaction over hydrophobic zeolites with isolated framework metal sites provides the potential for these catalyst to produce valuable liquid fuels and chemicals. However, no infrared spectroscopic studies do exist to investigate the properties of Sn sites to investigate the characteristics for aldol condensation reaction, intermediate adsorbed surface species, their affinities, and catalysts deactivation to understand Lewis-acidic catalyzed reaction over Sn BEA. Detailed kinetic, theoretical, and spectroscopical studies revealed reaction intermediates, their affinities and deactivation process for aldol condensation reaction of acetone over Bronsted acidic aluminosilicate using acetone as model compounds.[126] It can be postulated that acetone, simple C3 oxygenates, can effectively probe the properties of Sn sites for aldol condensation reaction such as the configuration of adsorbates from acetone, its reaction intermediates, affinity, and catalyst deactivation due to the undesirable formation of side products.

Biaglow et al. reported that at coverage below one molecule per active sites, the surface species formed from acetone are stable and acetone has low mobility on H-ZSM-5.[127] At high coverages, the mobility of acetone is increased, leading to the formation of mesityl oxide via the bimolecular condensation reaction. It is noted that the immobility of the mesityl oxide has lower mobility than acetone.[128] At the same time, for acetone, hydrogen-bonded adsorption complex is stable at room temperature, but H-ZSM-5 catalyzes acetone into mesityl oxide at high temperatures such as 100 °C. Interestingly, our

study shows that saturation of Sn BEA with 10^{-3} mbar of acetone exclusively formed mesityl oxide as seen in Figure 0.3. In addition, increasing temperatures up to 400 °C did not completely remove the surface mesityl oxide due to the high affinity to Sn sites. Figure 0.4 exhibited that diverse surface species are present by the interaction of acetone with Sn active sites in the high concentration of acetone (0.1 mbar) in the cell. The deconvolution of these peaks indicates that further condensation of mesityl oxide with acetone occurred to form bigger C9 oxygenates at 300 and 400 °C. It is reported that mesityl oxide is converted over a wide variety of aluminosilicates into aromatics, and cokes at high temperatures above 450 °C.[123] Therefore, mesityl oxide further reacted with neighboring unreacted acetone which is bound to silanol group, leading to the formation of C9 oxygenates, aromatics and cokes, but at relatively lower temperatures than over the Brønsted zeolites.[123] These surface species again exhibited the strong binding to Sn sites and accumulated on the surface as temperature increased up to 400 °C. Therefore, our data suggest that Lewis-acid catalyzed aldol condensation is more prone to catalyst deactivation to the counterpart of Bronsted acid catalyzed aldol condensation.

The deconvolution of the peak for C=O and C=C in IR spectrum (Figure B. 4) shows that the formation of mesityl oxide from acetone is preferred at low temperatures and the formation of the bigger oxygenates increases as temperature increases. Also, after 120 °C, aromatics and cokes were further generated in the absence of acetone that had been bound to silanol group (-Si-OH-), which indicates that the dehydration of intermediates adsorbates such as mesityl oxide is main mechanism of the formation of the dehydrated C9 oxygenates, and cokes. In addition, our data shows that the product formed from the self-aldol condensation of acetone have high affinity to Sn sites, so cannot be easily desorbed

from the catalyst at elevated temperature in the absence of other reactants or solvents. Furthermore, these surface species are prone to form the additional surface species via further aldol condensation of acetone, and undergo dehydration at high temperatures, leading to coke. In the previous studies, cross aldol condensation of acetone with aromatic aldehyde achieved the high conversion and yield with 32, and 90% over Sn BEA at 100 °C.[125] This kinetic studies well align in our date in that Sn BEA preferentially catalyze acetone into mesityl oxide at low temperatures below 120 °C. Therefore, we can postulate the high reaction temperatures induced the catalytic deactivation for Lewis-acid catalyzed aldol condensation of oxygenates.

The spectrum of adsorption of acetone (Figure 0.3) was helpful to postulate the mechanism for self-aldol condensation of acetone. The spectrum included a peak of enol form of acetone at 1579 cm^{-1} and the formation of Si-OH from abstracting α proton of acetone by an oxygen atom. These IR spectrum features indicate that C-C coupling of acetone through self-aldol condensation takes place by formation of enol as an initiation step, instead of one-step condensation mechanism recently proposed elsewhere.[120] Therefore, based on the IR spectrum seen in Figure 0.3 and Figure 0.4, we propose the self-aldol condensation mechanism of C-C coupling over Lewis acid solid catalysts as Scheme 2. Based on the Scheme 2, the framework oxygen atom bound to the Sn site works as Brønsted base and abstracts a α-proton from acetone as a base to generate a metal-enolate adduct and a silanol group prior to the adsorption of second acetone on Sn sites[85]. Then, adsorbed enolate undergoes C-C coupling with keto form of acetone, which can bind to the same metal site with the enol. The further reaction of mesityl oxide produces phorones,

isophorones, aromatics. These chemicals finally form coke when subjected to high temperatures.

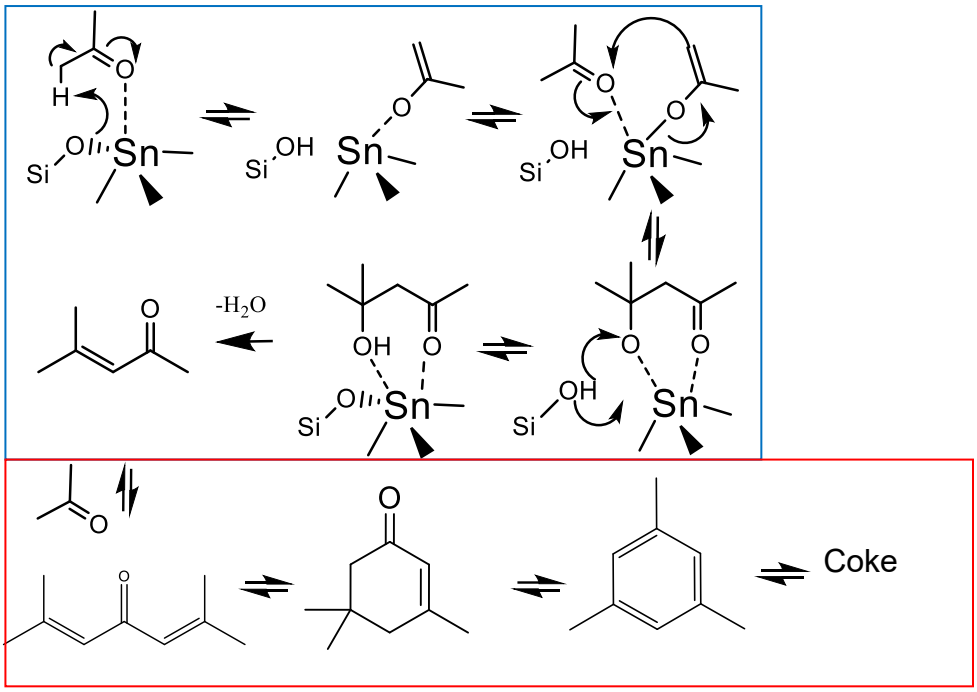

Scheme 0.2. FT-IR spectra of adsorbed hydroxyacetone over Sn BEA followed by TPD

Blue box – low temperature, Red Box- High temperature

Lewis acid sites in hydrophobic zeolites beta topology catalyze glucose to fructose via C2-C1 intramolecular hydride shift. However, Sn BEA synthesized in hydrothermal method is known to be inferior to hydrothermally synthesized Sn BEA. To reveal the origin of less reactivity and design a better catalyst, understanding of the configuration of adsorbates on Sn sites is required during isomerization via 1-2 hydride shift. The Davis group first reported that Sn-Beta yields 31% (wt⁄wt) of fructose from glucose at 383 K in pure water.[85] In the following study, it is shown that framework Sn sites in Sn BEA can catalyze the isomerization of glucose to fructose by a Lewis acid-mediated intramolecular hydride shift in an aqueous solvent.[129] Lewis acid catalyzed 1-2 hydride shift is also

essential to produce lactic acid from trios since dihydroxyacetone converts into glyceraldehyde via 1-2 hydride shift to produce lactic acid.[93, 130-131] Hydroxyacetone which has both carbonyl and α-hydroxyl group would be a good candidate as model compounds to investigate the reaction mechanism for 1-2 hydride shift due to the structural similarities to sugars and trioses.[132]

Our study shows that hydroxyacetone undergoes 1-2 hydride shift to isomerize hydroxyacetone to 2-hydroxypropanal, but further dehydration to form acrolein does not occur in contrast to the formation of mesityl oxide from acetone via self-aldol condensation and subsequent dehydration. We postulate that this inability to dehydrate 2-hydroxypropanal is due to the position of hydroxyl group within the molecule, which is located α-position. In case of mesityl oxide, β-hydroxyl group relative to α-hydroxy group of 2-hydroxypropanal can be easily removed by retro-Michael dehydration.[87] In addition to the formation of the isomerization product, the competitive pathway exists for hydroxyacetone to form enol, which can be either 2-propene-1,2-diol or 1-propene-1,2-diol. However, the peak for υC=C of enol is much smaller than the peak for υC=O of the 2-hydroxypropanal, which indicates that 2-hydroxypropanal formed from isomerization of hydroxyacetone is stabilized on Sn sites more effectively than the enol form of acetone on Sn sites.

Interestingly, 2-hydroxypropanal exhibited a strong affinity to Sn sites, and retained approximately 85 % of the peak intensity up to 400 °C. Even though IR spectra (Figure 0.5) shows propene-diol, 2-hydroxypropanal, and hydroxyacetone were present on the catalyst, the condensation reaction between enol and keto form of hydroxyacetone or 2-

hydroxypropanal was not observed. Also, dihroxyacetone reacted to produce only lactic acid, glyceraldehyde, and small molecules, instead of producing bigger molecules via a C-C coupling.[130, 133-134] This feature further gives insight into the role of α-hydroxyl group of carbonyl compounds that imparts stronger affinity toward Lewis acid sites to oxygenates. This strong affinity is presumably due to the capability of carbonyl compounds with α-hydroxy groups to engage in concerted binding to Sn sites with carbonyl and hydroxyl group in a similar way of chelating formation in homogeneous metal catalyts.[135-136]

1.12.2 The effect of water on the reactions by Sn BEA

Biomass reforming is a complex reaction networks where solvent-solute-catalyst interactions must be considered. In addition, a solvent often compete with a reactant for adsorption of active sites in solid catalyst. Glucose can isomerize into fructose over Sn BEA via a Lewis acid-mediated intramolecular hydride shift in the aqueous solvent, but a change in the solvent to methanol induces Sn sites to epimerize glucose to mannose by Lewis acid-mediated intramolecular carbon shift via the Bilik reaction using isotopically labeled (^{2}H, ^{13}C) glucose.[137] The upgrading biomass-derived oxygenates often uses water as a solvent or produces water as a by-product. However, many kinetics studies found that water can work as a poison, particularly to Lewis acid solid catalysts. The presence of water reduced the activity for Sn BEA for the MPV hydrogenation of cyclohexanone with 2-butanol by more than 80%.[138] Also, the activity for the isomerization of glucose to fructose over Snβ decreased by two orders of magnitude when the solvent changed from methanol to water.[139]

At the microscopic level, this reduced activity of Sn BEA in the presence of water is likely related to a change in the configuration of adsorbed species on active Lewis acid sites. It is well-known that the interaction of solvent molecules with Lewis acids drastically influences catalytic activity. Especially, solvents that exhibit a Lewis base character compete with reactants (Lewis bases) for coordinating with acid sites. The Gutmann's donor number (DN) is a parameter based on the enthalpy change for the coordination of an isolated solvent molecule to a hard Lewis acid ($SbCl_5$) in dichloroethane.[140] It provides a qualitative sense of the relative interaction of polar or nonpolar solvents with Lewis acids. The low DN values typically observed for aprotic nonpolar solvents suggest that they coordinate weakly to hard acid sites, whereas the high values seen for polar solvents suggest that very strong interactions with Lewis acids occur. We believe that water has a high DN value of 18 kJ/mol significantly higher aprotic solvents such as 0.1 for benzene, a representative aprotic solvent, thus suggesting that strong water-Lewis acid interactions can disrupt the interaction between reactants and Sn sites since the DN value for acetone is 17 kJ/mol.[141]

Acetone and mesityl oxide were reported to bind to acid sites strongly .[111-113] Therefore, in our study, saturating the catalyst wafer with water after dosing acetone did not produce any additional distinct adsorbate species at 50 °C. However, the most significant difference between during the TPDs in the presence of water was made. Dosing acetone on Sn BEA produced mesityl oxide, and it further reacted to form bigger oxygenates via C-C coupling and finally coke at the high temperatures in the absence of water. However, water promoted the desorption of adsorbed species as temperature increased, leading to the disappearance of all peaks between 1600 and 1500 cm^{-1}, which

can be attributed to the removal of adsorbed species including the ones formed by reactions of mesityl oxide with acetone. This lack of adsorbed species at high temperatures indicates that even though water does not promote the change in the configuration of both adsorbates formed from acetone, water reduced the strength of Lewis acid Sn sites and prevents mesityl oxide from reacting with acetone to form bigger C9 oxygenates.

Reactants biomass first formed an adduct by coordination of a Lewis acid sites as working as a Lewis base. In the condensed phase reaction, reactants should displace solvent molecules to interact with Lewis acid sites to be reacted fully. Figure 0.6B shows that the adsorption of water before acetone prevents aldol condensation reactions so that acetone can only interact with silanol groups (1693 cm^{-1}) as well as the carbonyl group of weakly physisorbed acetone at (1705 cm^{-1}). This complete blockage of the Sn sites results in desorption of almost all adsorbed species without the formation of significant amounts of coke when the samples is heated to 200 °C.

Overall hetero-catalytic reactions are determined by the relative proportion of rate constant for the association (K_A) reaction, reaction (K_R) and dissociation (K_D) steps.[142] Efficient Lewis acid catalysts can obtain appreciable overall reaction rate by the effective formation of Lewis acid and base complex coupled with marginal inhibition effect of the product.[142] Based on our study, aldol condensation reaction catalyzed by solid Lewis acid catalysts can be easily poisoned by the strong binding to products, which seems to require significantly dilute reaction condition. However, water might be beneficial to promote the desorption of products by increasing K_D constants based on our study. However, the pure aqueous environment can significantly suppress the aldol condensation by decreasing K_A constants.

Interestingly, hydroxyacetone formed 2-hydroypropanal in the presence of pre-adsorbed water 3 min, although carbonyl peak of 2-hydroxypropanal slowly developed compared to the adsorption of hydroxyacetone without the presence of water. This phenomena is due to the competition between water and oxygenates (reactants) for Lewis acid sites often in condensed phase reforming similar to the previous studies.[50] After letting hydroxyacetone fully interact with the catalyst until the spectrum did not change, a carbonyl peak red-shifted from 1667 to 1653 cm^{-1}. Since the water competes for the LA sites with hydroxyacetone, it is unlikely that the electron donation of water to Sn sites would strengthen the interaction of the carbonyl group of hydroxypropanal with Sn sites. Therefore, 2-hydroxypropanal might further transform over Sn sites in the presence of water. To identify the surface species, the adsorption of acrolein on Sn BEA was investigated using IR spectroscopy. Figure B. 9 shows that the spectrum of adsorbed of acrolein exhibited a νC=O mode of the carbonyl group and the νC=C mode of acrolein at 1650 and 1592 cm^{-1}, respectively. The deconvolution of the peaks in the spectrum in Figure B. 9 clearly shows a νC=O of the carbonyl group and νC=C band at 1653 and 1591 cm^{-1}, which can be attributed to acrolein as well as the carbonyl group from hydroxyacetone and the δOH vibration of water. Therefore, it is likely that water promote surface 2-hydroxypropanal to undergo dehydration to acrolein with the aid of water. The Roman-Leshkov group reported a C-C coupling reaction between hydroxyacetone and formaldehyde to produce α-hydroxy-γ-butyrolactone (HBL) over Snβ at 160 °C and suggested the mechanism in which erythrose formed as intermediates from aldol addition of formaldehyde to the Sn-enolate form of dihydroxyacetone undergoes dehydration since the presence of β-hydroxyl and carbonyl group in erythrose makes it highly susceptible to

dehydration a retro-Michael reaction. In the current study, we can speculate that the hydrogen bonding of water to α-hydroxyl group of 2-hydroxypropanal make it better leaving the group, leading to the formation of acrolein.

To investigate the effect of water on the desorption of products, we dosed hydroxyacetone and then saturated the catalyst with H_2O followed by TPD. Reduced strength of LA sites by electron donation from water leads to observing the small portion of unreacted hydroxyacetone of which the carbonyl group at 1687 cm^{-1} just interacts with Sn sites, instead of transformation over Sn sites. When the convoluted peaks between 1550 and 1750 cm^{-1} are deconvoluted, the absence of the νC=O mode of the carbonyl group at 1654 cm^{-1} indicates that 2-hydroxypropanal is readily converted into acrolein when promoted by water. The formation of acrolein in the presence of water supports our hypothesis that water helps 2-hydroxypropyl more susceptible to dehydration via retro-Michael reaction by pulling the electron of a-hydroxyl group of 2-hydroxypropanal. Instead, water directly associates Sn sites to promote the Sn sites to which hydroxyaceotne and 2-hydroxypropanal strongly bound as seen in Figure 0.7.

The hydrolyzed Sn BEA did not produce any significant surface species except the adsorbed acetone. The strong binding of the surface species to active sites are a common problem of the catalyst deactivations. Dosing 1 mbar of acetone into the IR cell which has the Sn BEA catalyst wafer showed that surface species which is catalyzed by Lewis acid sites accumulated on the surface, instead of desorption. This high affinity can be reduced in the presence of spectator surface species which does not involve in the reaction pathway but can interact with the active sites by the competitive adsorption.

1.12.3 Tuning the strength of the Lewis acid site by incorporating metals (VI) into beta zeolite topology

Metal centers incorporated into the structure of the zeolite have different strength of Lewis acid and intrinsic catalytic performance for specific reactions. Ti-, Sn- and Zr-BEA are active catalysts for the Meerwein–Ponndorf–Verley reduction of cyclohexanone with 2-butanol but exhibits different activities.[143] Also, Sn BEA showed the highest activity for glucose-fructose isomerization[82] and conversion of sugars into lactic acid or alkyl lactates than Ti- and Zr BEA. However, Hf- and Zr- BEA has a higher selectivity for the C-C coupling of acetone with aromatic aldehydes via aldol condensation than Sn BEA.[125] To reveal the origin of these difference in the reactivities of heteroatom doped beta zeolites, the IR spectra of pyridine adsorption was used to correlate the frequencies of adsorbed pyridine on different Lewis acid sites (i.e., Ti-, Zr-, Nb-, Ta-, Sn-, Ga-, and Al-beta) with the Lewis acid strength, but exhibited the limited reliability due to a narrow range of peak frequencies from 1445 to 1454 cm^{-1}.[100] Since the magnetic shielding in NMR spectroscopy is sensitive to the local electronic environment about the nucleus, changes in the chemical shift for a particular acid-base pair can be used to rank the Lewis acidic sites of zeolites.[144-146] The Roman group found that ^{15}N chemical shift observed can be used as a scale for Lewis acidity that exhibits a linear correlation with Mulliken electronegativities based on magic angle spinning (MAS) nuclear magnetic resonance (NMR) of ^{15}N pyridine adsorbed on M-Beta zeolites.[146]

The strength of interaction between the acid−base pair is proportional to orbital overlap and inversely proportional to its HOMO−LUMO energy difference.[147] LUMO energies are difficult to obtain experimentally but exhibiting a linear relationship with

electron affinity.[147] In the same way, the HOMO energies correlate with ionization potential.[146] The extent of strength between acid and base depends on the HOMO−LUMO gap.[146] Electron affinity, and Mulliken electronegativity exhibits a linear relationship with the experimental determined ^{15}N isotopic chemical shift values.[146]

Based on the Based on Hard−soft acid-base theory (HSAB) uses chemical hardness, polarizable acids, and bases as soft and nonpolarizable acids and bases as hard.[105] The HSAB concept is used to explain deviations from a pure electronegativity analysis.For example, thiocyanate, SCN-, can form a bonding through either its sulfur or nitrogen. When it bonds to a soft acid such as Hg^{2+}, it bonds through sulfur, but when it bonds to less polarizable meals such as Zn^{2+}, it bonds through nitrogen. The HSAB theory suggests that hard acids prefer to bind with hard bases and soft acids prefer to bind with soft bases. Pearson developed a quantitative measure of the concept of hard and soft acid and defined the absolute hardness as half the difference between the ionization energy and the electron affinity.[148]

In our study, the value of calculated Mulliken electronegativity of W BEA is similar to the one of Sn BEA. W BEA exhibited the negligible activity for aldol condensation reaction for acetone and isomerization of hydroxyacetone. Mo BEA has a comparable value for calculated hardness (Table) has a negligible activity for aldol condensation reaction of acetone but catalyzes hydroxyacetone into 2-hydroxypropanal, but with lower activity than Sn BEA. Therefore, our data indicate that hardness is a reasonable parameter to describe for Lewis-catalyzed reactions by metal-substituted beta zeolites compared to Mulliken electronegativity. However, the conclusion could not explain the inactivity for aldol condensation of acetone.

When considering the mechanism of aldol condensation reaction described in Scheme 0.2, the keto and enol form of acetone is needed to associate with Sn for C-C-C coupling after the formation of enol via tautomerization of acetone. Therefore, substituted-metal sites need to provide enough surface area which for keto and enol form of acetone simultaneously can bind to. When periodic V group (i.e., Nb and Ta) transition metals are substituted into zeolite BEA, Nb and Ta exist in a +5 oxidation state and were modeled with a M=O functional group in DFT calculation.[103, 146] Therefore, in our study, Mo and W which is the most stable in a +6 oxidation state is most likely to exist as +6 state in the BEA topology. Table B. 1 shows that the ionic radius of W and Mo is smaller than Sn by 25%.

Also, cross aldol condensation reaction of acetone with aldehyde showed a trend where yield and selectivity decrease in the order Zr-, Hf- and Sn BEA, and ionic radius decreased in the same order Zr-, Hf- and Sn BEA. The superior reactivity of Zr- and Hf BEA zeolites to Sn BEA was in the study by the different type of orbital to participate as a frontal orbital for Lewis acid-Lewis base interactions. The d-block transition metals Hf and Zr possess similar electronic structures when inserted in the zeolite framework and can be expected to show same catalytic activity, while the p-block element Sn exhibits different bonding characteristics and charge distribution through the site because of its antibonding σ* LUMO. This difference in the type of the frontal orbital was explained for superior reactivity of Zr- and Hf BEA to the counterpart of Sn BEA. However, Ti BEA which has the d-block transition metals as Hf and Zr exhibited a negligible conversion (2% percent) of acetone and benzaldehyde into benzalacetone. However, Ti BEA has also approximately 28 % smaller size of metal in the BEA topology compared to Zr- Hf BEA. Therefore, it is

highly likely that ionic radius would be an essential parameter for C-C coupling for production of bigger oxygenates in which carbonyl group and β-hydroxyl group of the product oxygenates such as mesityl oxide simultaneously bind.

1.13 Conclusion

In this article, we present a method to study the active sites of heteroatom-doped zeolites using the probe molecules: acetone and hydroxyacetone. The formation of adsorbates from simple C2 oxygenates: acetone and hydroxyacetone on Sn BEA is investigated using FTIR spectroscopy in the presence and absence of H_2O vapor. Acetone is exclusively converted into mesityl oxide in the low amount of acetone saturation over Sn BEA. Increasing concentration inside the pore of the zeolites promotes acetone to further react with mesityl oxide to form bigger oxygenates such as phorones, aromatics, and cokes at high temperatures. Hydrated Sn BEA shows negligible activity for aldol condensation of acetone due to losing activity for tautomerization of acetone in the presence of H_2O vapor. However, H_2O is vapor beneficial for minimizing coke formation at high temperatures by the reduced strength of Sn sites by H_2O vapor. Hydroxyacetone is converted into 2-hydroxypropanal over Sn BEA, exhibiting high affinity to Sn sites up to 400 °C. Sn BEA still catalyzes hydroxyacetone into 2-propanal in the presence of H_2O but longer exposure of H_2O vapor while hydroxyacetone is interacting with Sn BEA induced the formed 2-hydroxypropanal to convert into acrolein. Mo and W BEA are synthesized using solid-solid ion exchange method to investigate important parameters such as Mulliken electron affinity, Lewis acid hardness, and radius of metal ions which can control Lewis acid catalyzed the reaction by the zeolites which has metals incorporated into the

structure. For isomerization of hydroxyacetone into 2-hydroxypropanal, which requires the α-hydroxyl group and the carbonyl group of hydroxyacetone of oxygenates, the hardness of Lewis acidity is an influential factor based. However, the size of metal significantly affects aldol condensation reaction where keto and enol form of acetone need bind to active sites simultaneously, leading to the formation of binding of β-hydroxyl group and the carbonyl group of mesityl oxide.

Elucidation of Oxidation State of MoO_3 for Biomass Conversion

1.14 Introduction

The demand for biorefinery to produce transportation fuels and chemicals from lignocellulosic biomass has increased over the last decade in global efforts to lower the carbon footprint. Heterogeneously catalyzed processes in condensed phase such as methanol and water will be likely to play an important role in the biorefineries due to facile separation and stability at high temperatures. Among many viable heterogeneous catalysts, molybdenum oxide recently gained significant attention since it catalyzes many important reactions for biomass conversion including sugar epimerization[149] and conversion of sugars into alkyl lactates at moderate temperatures (100 °C) in combination with Lewis acidic zeolite Sn-MFI. Especially, in the latter study, physically mixed MoO_3 exclusively promoted retro-aldol condensation reactions of sugars into C3 oxygenates since glucose cannot transport into near Sn sites which are located inside the pore of MFI due to the size of glucose.

MoO_3 is a reducible metal oxide which has the capability to exchange oxygen in a relatively easy way. Therefore, they are found in various types of stoichiometry, ranging from full stoichiometric MoO_3, which has a wide bandgap to conducting reduced oxides in the form of $MoO_{3-x}(2<x<3)$ with significantly reduced band gap.[150-151] The reducibility of MoO_3 induces fundamental importance for the chemical reactions, which often follows the Mars and Van Krevelen mechanism where the oxide surface is directly involved via its most reactive oxygen atoms on the catalyst surface.[151-152] An organic substance often reacts with these reactive sites at the oxide surface. During this step, a weakly bound surface O

atom is often imparted to the reactant forming the oxygenated compound, leaving behind an oxygen vacancy on the surface.

Orazov and Davis have reported that yields of 75% in the trioses dihydroxyacetone (DHA) and glyceraldehyde (GLA) in alcoholic solvents at 80 °C.[153] In the following DFT study, the open-chain fructose molecule can undergo retro-aldol fragmentation at the position and suggested the mechanism.[154] Fructose is initially promoted by deprotonation of the β-OH group. This leads to the electron density redistribution and subsequent C-C bond scission, leading to the formation of glyceraldehyde and an enolate intermediate. However, the experimental and DFT studies did not take account of the effect of an alcohol solvent, which can readily affect the oxidation state of MoO_3 due to its high capabilities as an oxidizing agent. For example, ethanol MoO_3 showed very high selectivity to acetaldehyde with a negligible amount of ethane at 200 °C, but MoO_2 shows the same selectivity (48.4 %) and acetaldehyde (48.5 %) at 200 °C.[155] Therefore, it is possible that even at low temperatures used for lactic acid production such as 80 °C to minimize the side products during the reaction, the alcoholic solvent used for lactic acid production from fructose can chemically react with MoO_3.

When considering the high reducibility of α-MoO_3, It is highly likely that that α-MoO_3 can undergo structural changes during reactions and subsequent formation of oxygen vacancy. However, little is known, however, on how the nature and extent of the transformation of α-MoO_3 due to these oxygen vacancies affect catalytic reactivity and reaction pathway for biomass conversion in the condensed phase. This insight will be

critical to design catalysts to tune the active sites and determine the operational conditions to maximize the yield and selectivity for certain reactions.

1.15 Experimental Method

1.15.1 Materials

Ethanol (>99.5%), acetaldehyde (>98%), molybdenum oxide (α-MoO_3) (>99.95%), potassium bromide (FTIR grade, >99%) were purchased from Sigma Aldrich.

1.15.2 FT-IR spectroscopy

Molybdenum oxide(α-MoO_3) was pressed into a self-supported wafer and loaded into a transmission vacuum chamber. The sample was activated at 450 °C for 1 h under high vacuum conditions and was cooled down to the room temperature. A background spectrum was collected. Ethanol or acetaldehyde was introduced into the chamber as vapors at 0.1 mbar through a leak valve. A spectrum was collected at 10 sec, 1 min, 5 min after the reactant adsorption. After 30 min, 0.7 mbar of ethanol or acetaldehyde was further introduced into the IR chamber and a spectrum was collected after 1 hr.

A different procedure was used for α-MoO_3 which is treated with methanol. After the preparation of α-MoO_3into the IR chamber and subsequent activation at 450 °C for 1 h under high vacuum condition, methanol was dosed at 0.1 mbar into the IR chamber and made contact with α-MoO_3 catalyst wafer for 1 h. Then, the same procedure was repeated as the untreated α-MoO_3 with methanol.

All spectra were collected using a Nicolet 8700 FTIR spectrometer with an MCT/A detector. For each spectrum, 64 scans were recorded at a resolution of 4 cm^{-1}. All spectra were collected using a Nicolet 8700 FTIR spectrometer with an MCT/A detector. Thermo Fischer Scientific Inc. Grams 9.1 software was used to process the collected spectra

1.16 Results and discussion

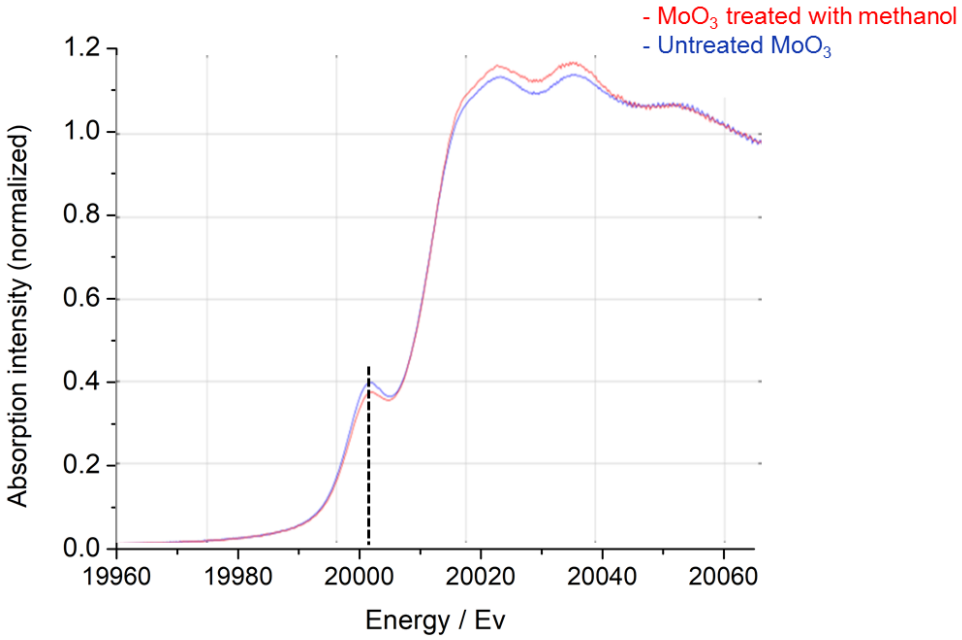

Figure 0.1. XANES spectra at the Mo K-edge for the bulk molybdenum oxide (MoO_3) (blue) and reduced molybdenum oxide (MoO_x) with methanol (red).

The high capability of MoO_3 as an oxidizing agent is likely to undergo the structural change by interacting with alcohol reagents, which are often used as a solvent for biomass conversion. XANES spectra sensitive to the symmetry of the local structure of the X-ray absorbing atom (Mo) are used to investigate the change in the oxidation state after treating MoO_3 with methanol. Figure 0.1 shows the Mo K-edge XANES spectra of MoO_3 and

partially reduced MoO_x with methanol at room temperature. A weak peak appeared in both MoO_3, and MoO_x samples in the pre-edge region (20005–20010 eV) is assigned to a 1s → 4d quadrupole transition.[156-157] This dipole-forbidden transition became possible owing to the central position of Mo^{6+} ion in the distorted octahedron of MoO_3.[156] Also, for MoO_3 containing Mo^{6+}, the pre-edge peak is observed with a lower value of energy than the absorption edge of Mo as seen Figure 0.1. Even though both MoO_3 and MoO_x have the pre-edge peak, but the peak intensity for reduced MoO_x with methanol exhibited a noticeable decrease in the peak intensity. This result indicates that since the decrease in the peak intensity of pre-edge peak is relatively small, the surface of MoO_3 is reduced with methanol, leading to the oxygen vacancy at room temperature.

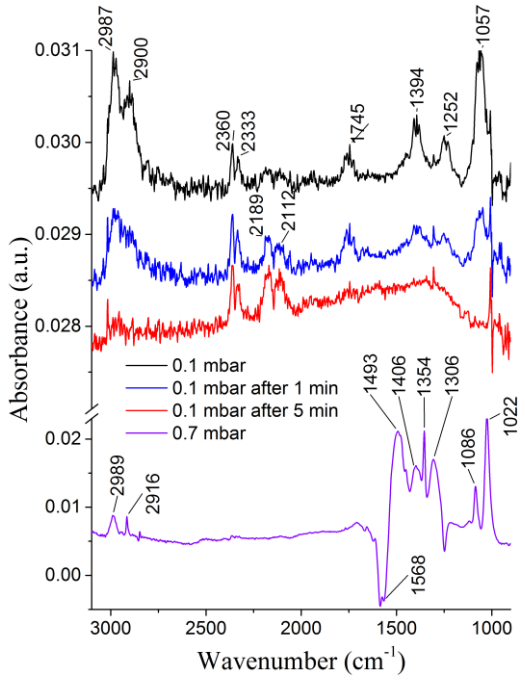

Figure 0.2. IR spectra of surface species formed from ethanol on MoO_3 at room temperature

To elucidate the impact of the formation of oxygen vacancies on the adsorption and reaction of oxygenates, we studied the surface chemistry of ethanol and acetaldehyde on a MoO_3 wafer by in-situ FTIR spectroscopy after activation in vacuum at 450 °C. When 0.1 mbar of ethanol were introduced into the cell at room temperature, the first IR spectrum at 10 s (Figure 0.2) contained characteristic bands for νCH (2987-2900 cm^{-1}), δCH (1252 and 1394 cm^{-1}), and νCO (1057 cm^{-1}).[158] These bands are consistent with the formation of chemisorbed ethanolate species.[59, 159] The additional peak at 1745 cm^{-1} is attributed to the νCO vibration of an aldehyde group indicating that some of the adsorbed ethanol was dehydrogenated.[155] Lastly, the doublet of peaks at 2360 and 2333 cm^{-1} is assigned to CO_2 in the gas phase. The observation of gaseous CO_2 indicated that ethanol reacted with surface oxygen atoms forming CO_2 (and H_2 or H_2O), leading to partially reduced MoO_3. In the spectrum after 1 min (Figure 0.2), all bands associated with the ethanolate species had lost intensity, and two additional peaks at 2189 and 2112 cm^{-1} were observed. They are tentatively attributed to physisorbed CO_2.[160] The reaction progressed so that after 5 min only the bands attributed to CO_2 were left (Figure 0.2). At the same time, the pressure in the cell had increased to 0.17 mbar, which indicates that ethanol decomposed into H_2O, CO_2, and acetaldehyde. The formation of CO_2 from interacting of ethanol with MoO_3 at HV indicates that acetaldehyde can be oxidized into CO_2 with the surface oxygen of MoO_3. When more ethanol was admitted into the cell, MoO_x, eventually reached an oxidation state that was stable under the given reaction conditions. The negative band at 1568 cm^{-1} provides additional evidence for the formation of a partially reduced phase, leading to the change in structure (Figure 0.2).[161] After this point, stable surface species were observed. The bands were significantly sharper than the ones observed after the first exposure to

ethanol (Figure 0.2). The observation of two well-resolved C-O stretching bands at 1086 and 1022 cm^{-1} is attributed for the formation of two distinct ethanolate species on different surface sites.[159] In agreement with this, the C-H stretching region (2800-3000 cm^{-1}) clearly contained multiple well-resolved contributions. The IR spectra of saturated MoO_3 with methanol did not shows noticeable CO_2 bands. The absence of CO_2 indicates that once surface MoO_3 is completely reduced, MoO_x lose activity for ethanol decomposition.

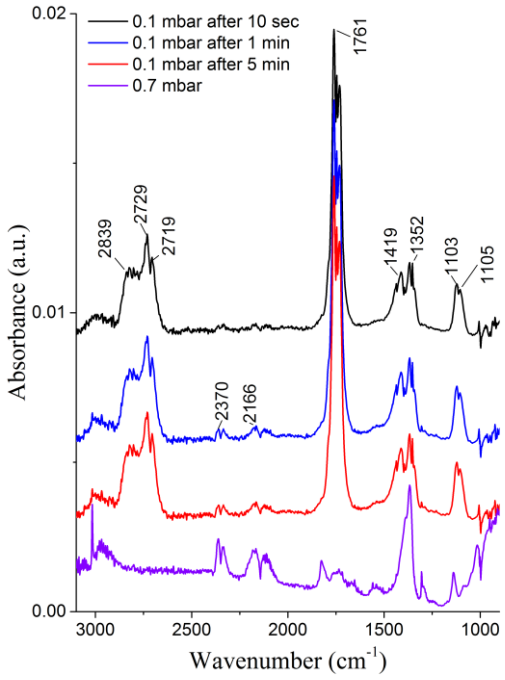

Figure 0.3. IR spectra of surface species formed from acetaldehyde on MoO_3 at room temperature

When 0.1 mbar of acetaldehyde was introduced into the IR cell, the IR spectrum in Figure 0.3 after 10 sec exhibited various characteristic bands which included νCH (2839-2729 cm^{-1}), νCO (1761 cm^{-1}), δCH (1419 cm^{-1}), CH rocking mode (1352 cm^{-1}), and νCC (1103 cm^{-1}).[59] These vibrational modes can be attributed to various modes of

acetaldehyde.[162] The characteristic peaks for gaseous CO_2 (2370 and 2166 cm^{-1}) were observed after 1min of exposure of acetaldehyde and the intensity slightly increased after 5 min even though the intensity of CO_2 peak is much lower than the counterpart in ethanol oxidation at the same timescale. Considering the immediate formation of CO_2 upon introduction of ethanol (Figure 0.1), the delayed formation of CO_2 and its low intensity compared to ethanol oxidation indicates that acetaldehyde oxidation is much slower than ethanol oxidation. Interestingly, when acetaldehyde was introduced into the IR cell at 0.7 mbar for 1 hour, the various modes of acetaldehyde were significantly reduced. At the same time, the intensity of peaks of gaseous CO_2 increased. The reduced intensity of bands for acetaldehyde and the increased peak intensity for CO_2 indicates that even though acetaldehyde was converted slower than ethanol by MoO_3, acetaldehyde was fully converted into oxygenates such as methane, acetic acid, and CO_2 in the same way of ethanol oxidation. MoO_3 catalyze the oxidation of ethanol faster than acetaldehyde, which indicates that dehydrogenation step is a relatively faster step compared to oxidation of acetaldehyde. This might be due to the easiness of formation of water by abstracting two hydrogen atoms from ethanol. MoO3 can catalyze acetaldehyde in the two different pathway: decomposition into CO2 using the oxygen on the surface and the conversion into propylene by a removal of oxygen of acetaldehyde by oxygen vacancies. The latter reaction pathway usually requires high reaction temperature and H_2 presence to keep creating the oxygen vacancies. [163]

An important consideration for the conversion of oxygenates over reducible metal oxides is that the formation of oxygen vacancies can significantly affect the activity and product selectivity of a catalyst, requiring a strict control of the oxidation state of the

catalyst.[164] For example, molybdenum trioxides (MoO_3) catalyzes acetaldehyde from ethanol with high selectivity, but reduced molybdenum oxide (MoO_2) produced ethane and acetaldehyde with significantly decreased conversion of acetaldehyde at 575 K.[155] In another study, HDO reaction of oxygenates such as acetone and cyclohexanone requires the presence of H_2 to keep the oxidation state of Mo, which prevents catalytic deactivation 673K.[165] The depletion of oxygen on MoO_3 would affect the decomposition of oxygenates at room temperature.

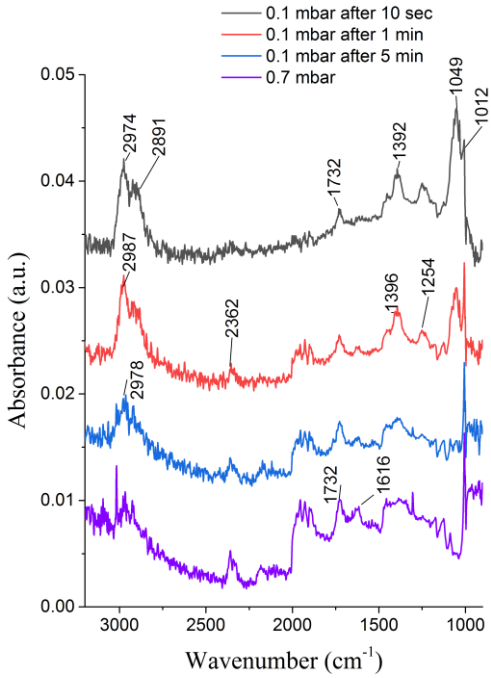

Figure 0.4. IR spectra of surface species formed from ethanol on reduced MoO_x at room temperature

Significant differences of the rate of ethanol decomposition were observed when MoO_3 was partially reduced by exposure to methanol. To probe the effect of reduction of MoO_3 on the reactivity and reaction pathway of ethanol, the MoO_3 sample was activated

in vacuum at 450 °C and reduced with 1 mbar of methanol for 1 hour at room temperature. Then, ethanol was introduced into the cell. Figure 0.4 shows that first IR spectrum taken after 10 s upon the introduction of ethanol contained characteristic bands for νCH (2987-2900 cm^{-1}), δCH (1252 and 1394 cm^{-1}). Also, the characteristic carbonyl band for νCO (1732 cm^{-1}) was observed due to the formation of acetaldehyde. The noticeable difference was observed in the range of characteristic bands for CO_2. Previously, ethanol over MoO_3 immediately reacted upon introduction of ethanol, leading to the formation of CO_2. However, the characteristic band for CO_2 was missing in the spectrum at 0.1 sec. In the spectrum after 1 min (Figure), characteristics bands for the ethanolate species remained on the surface, and bands for CO_2 (2363 cm^{-1}) started to form. After 5 min, the peak of ethanol was slightly reduced to the ones in the spectra at 1 min, and the pressure in the cell had increased to 0.12 mbar. Even when ethanol pressure was increased to 0.17 mbar, there was not significant increase in both the intensity of CO_2 and the characteristic bands for acetaldehyde. Interestingly, we could not observe the significant change in IR spectrum due to the structural change of reduced MoO_3, which indicates that acetaldehyde does not decompose well by using oxygen on the surface even though some of the CO .

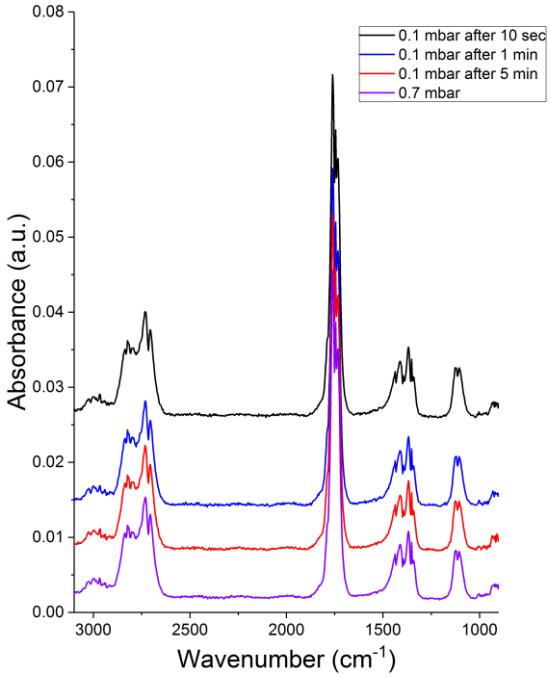

Figure 0.5. IR spectra of surface species formed from acetaldehyde on reduced MoOx at room temperature

Again to investigate the reactivity of acetaldehyde over reduced MoO_3, the MoO_3 sample was activated in a vacuum cell for FT-IR spectroscopy at 450 °C and reduced with 1 mbar of methanol for 1 hour before dosing acetaldehyde. All of the spectra contained the characteristic bands for acetaldehyde and modes of CO_2 was not observed. This inactivity of acetaldehyde indicates that oxidation state of MoO_3 affects the reactivity of acetaldehyde.

The redox properties molybdenum oxide catalyzes the oxidation of an olefin to aldehydes and ketones.[166] The activity of these catalysts is often explained by way of a Mars-van Krevelen mechanism, in which an oxygen atom located at the surface of the catalyst reacts with the olefinic compound to yield an oxygenated product plus an oxygen

vacancy site.[167] In particular, these catalysts are applied to upgrade bio-oils in HDO process where small oxygenates can be converted into the value-added products by way of a reverse Mars-van Krevelen mechanism. Reduced MoO_3 can remove of the oxygen atom from oxygenates upon the adsorption on the vacancy site, and the vacancy sites can be regenerated in the presence H_2, leading to the formation of H_2O. In the same study, propylene can be produced with high selectivity from acetone. In our study, acetaldehyde which has similar structure as acetone exhibited high reactivity over MoO_3 even though the rate of decomposition is slower than the decomposition of ethanol. However, reduced methanol does not have any reactivity for the acetaldehyde conversion into propylene at room temperature. HDO of acrolein on MoO_3 to propylene is thermodynamically favorable only after 593 K. Furthermore, HDO reaction of oxygenates such as acetone to produce propylene was studied at 673 K, which is much higher than the current temperature studied. However, unreduced MoO_3 This is mainly due to the low temperature when acetaldehyde. The inactivity for acetaldehyde over reduced MoO_3 indirectly indicates that the HDO reaction of acetaldehyde requires the presence of H_2.

In our study, the redox properties of molybdenum affect the oxidation of oxygenates at room temperatures. The ethanol oxidation over reduced molybdenum oxide with methanol was not as efficient as untreated molybdenum oxide. In the recent study, DFT calculation suggested that the reaction follows the classic mechanism of C-C bond activation by proton abstraction from the β-OH group of the sugar and resulting enolate intermediate is activated by charge delocalization through coordination of the carbonyl group of the sugar to a Lewis acidic Mo atom.[154] However, abstraction of hydrogen of hydroxyl group in ethanol resulted in reduced molybdenum by observing the formation of

CO_2 and lost activity after continuous exposure of ethanol at longer time. Our result can be milestone to start to consider the redox properties of MoO_3 for realistic DFT calculation for sugar conversion in methanol solvent.

Also, even though tandem catalysts comprised of Sn MFI and molybdenum oxide catalyzed glucose to lactic acid at lower temperatures than Sn MFI itself by lowering the activation energy of retro-aldol reaction, which is a limiting reaction step.[153] However, the reaction was conducted in methanol solvent so there would be a high chance that the catalyst deactivation would occur due to change in the surface oxidation state. In our study, both acetaldehyde and ethanol exhibited the limited activity for the oxidation due to the formation of oxygen vacancies of MoO_3. This indicates that reduction of MoO_3 occurs at room temperature, and we need to provide the source of oxygen to maintain the catalyst activity for biomass-derived oxygenates are processed in an alcohol solvent.

1.17 Conclusion

α-MoO_3 are known to have an activity for C-C bond cleavage of oxygenates via retro-aldol reactions in the condensed phase but easily tend to lose the activity for the reaction. We found that α-MoO_3 has high activity for the decomposition of ethanol and acetaldehyde which are used as model compounds to mimic the functionalities of biomass-derived oxygenates. However, α-MoO_3 is easily reduced by the depletion of surface O atoms of α-MoO_3 during the decomposition. IR spectroscopy and XANES revealed that the only surface of the catalysts was reduced and the reduced α-MoO_3 exhibited the different reaction path, instead of the full decomposition of ethanol and acetaldehyde into CO_2 due to the absence of O atoms on the surface.

Future work and recommendations

1.18 Recommendations for Chapter 2

In our study, regardless types of sugar and polyols, CO_B is more susceptible to WGS reaction. This result suggests that supported Pt particle with a higher density of terrace sites will be beneficial for CO_B formation. It is well established that the ratio of the terrace to edge/kinks sites highly depends on the size of Pt particles and it is well-studied that CO_B more preferentially binds to the terrace sites.[64, 168] Thus, the future work should focus on the correlation between the particle size of Pt and the ratio of CO_B to CO_L to maximize the CO oxidation via WGS reaction.

1.19 Recommendations for Chapter 3

Sn BEA readily catalyzes acetone to form bigger oxygenates such as mesityl oxide via aldol condensation reaction. Low amount of acetone exclusively formed mesityl oxide due to the absence of neighboring acetone, which prevents mesityl oxide from further reacting with acetone to form C9 oxygenates including phorones, isophorones at low temperatures and aromatics and cokes at high temperatures. The observation of the fast formation of mesityl oxide at HV suggests that Lewis-catalyzed aldol condensation by Sn BEA would be more active than Bronsted catalyzed aldol condensation reaction by aluminosilicates.[126] Our data suggest the strong binding can easily poison aldol condensation reaction catalyzed by solid Lewis acid catalysts to products, which seems to require significantly dilute reaction condition. H_2O present inside the pore of zeolites blocks acetone from interacting with active sites, leading to the total shut down of keto-

enol tautomerization, the initial step for C-C coupling. This is most likely to the reduced strength of Sn by H_2O adsorption, but H_2O significantly prevent active sites from being deactivated by mesityl oxide which was missing at high temperatures in the presence of H_2O. In short, water might be beneficial to promote the desorption of products by increasing K_D constants based on our study. However, the pure aqueous environment can significantly suppress the aldol condensation by decreasing K_A constants. This observation leads to the formation of the postulate that small amount of water can be beneficial to reduce the binding strength of the formed products from aldol condensation reaction and Sn sites.

Future work should include the kinetic studies of the conversion of acetone in the absence and presence of H_2O to investigate the inhibiting and promotional effect of water by correlation H_2O content in the feed stream with selectivity for mesityl oxide and the onset of the catalyst deactivation. In addition, operando IR spectroscopy can provide a tool to correlate types of adsorbates with product distribution of aldol condensation reaction of oxygenates.

1.20 Recommendations for Chapter 4

In our study, the redox properties of molybdenum affect the oxidation of oxygenates at room temperatures. The ethanol oxidation over reduced molybdenum oxide with methanol was not as efficient as untreated molybdenum oxide.

Glycolaldehyde is the organic compound with the formula $HOCH_2$-CHO. It is a 2-carbon monosaccharide that contains both an aldehyde group and a hydroxyl group. Using this simplest sugar-related molecule provides a tool to mimic the isomerization or

epimerization occurring on the molybdenum surface. Since the glycoaldehyde exists in a solid state, the next study should consider ex-situ impregnation method[12, 49-50] where one monolayer of the oxygenate in solution mixed with water and methanol is deposited based on the surface area experimentally obtained N_2 physisorption. In addition, the future study should investigate the adsorption of glyceraldehyde (glyceral), a triose monosaccharide with chemical formula $C_3H_6O_3$, which undergoes the retro-aldol condensation reaction. The proposed study will elucidate the effect of the presence and absence of oxygen vacancies on retro-aldol condensation and isomerization of sugar over MoO_3.

In the recent study, DFT calculation suggested that the reaction follows the classic mechanism of C-C bond activation by proton abstraction from the β-OH group of the sugar and resulting enolate intermediate is activated by charge delocalization through coordination of the sugar's carbonyl group to a Lewis acidic Mo atom.[154] However, abstraction of hydrogen of the hydroxyl group in ethanol resulted in reduced molybdenum by observing the formation of CO_2 and lost activity after continuous exposure to ethanol at longer time. Therefore, the consideration of oxygen vacancies will enable more realistic DFT calculation for sugar conversion in methanol solvent.

Lastly, even though tandem catalysts comprised of Sn MFI and molybdenum oxide catalyzed glucose to lactic acid at lower temperatures than Sn MFI itself by lowering the activation energy of retro-aldol reaction, which is a limiting reaction step.[153] However, the reaction was conducted in methanol solvent so there would be a high chance that the catalyst deactivation would occur due to change in the surface oxidation state. To maintain the catalyst activity, our data suggest that oxygen source in the feed stream would provide a source to fill up the vacancies that would be caused by methanol solvent.

Appendix A: Supplementary Information for Chapter 2

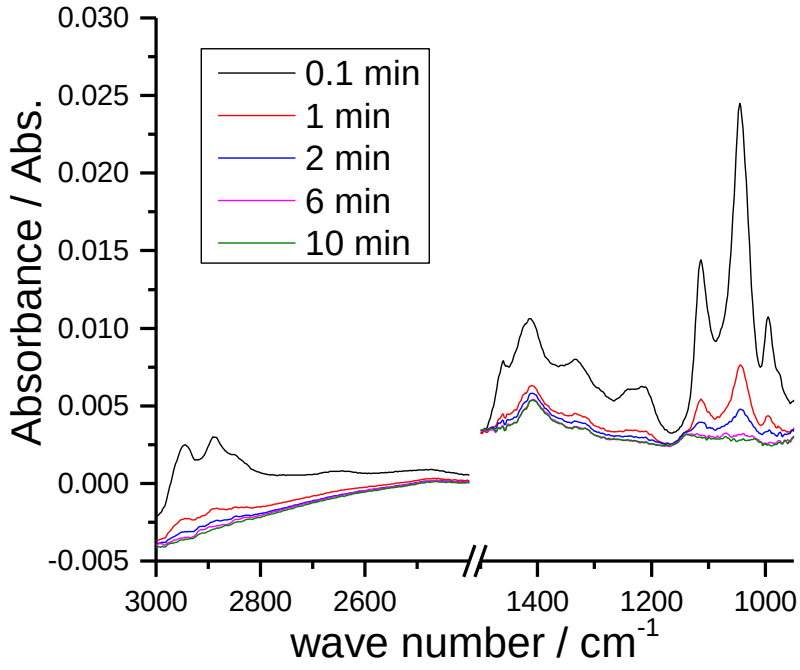

Figure A. 1. ATR-IR spectra of catalyst during 1st H_2O flow period during APR of glycerol

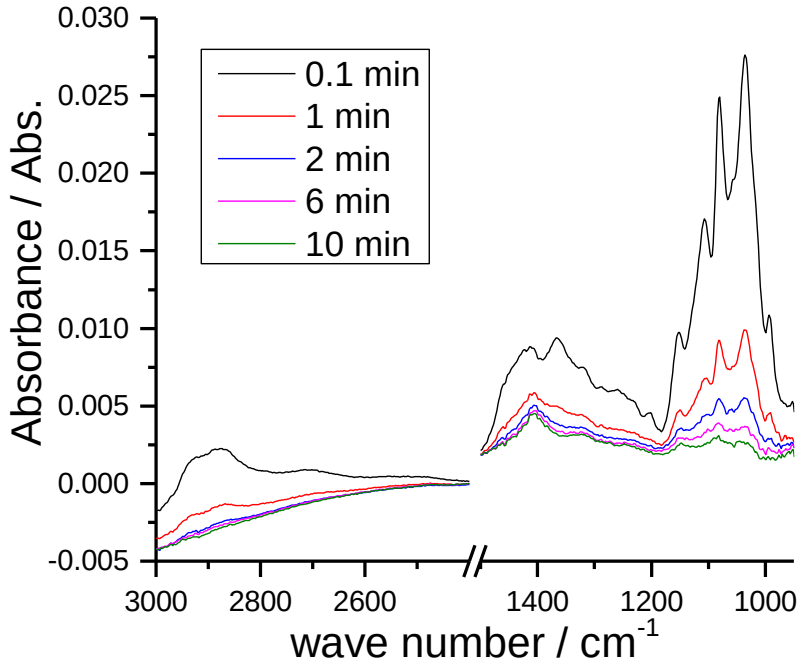

Figure A. 2. ATR-IR spectra of catalyst during 1st H_2O flow period during APR of glucose

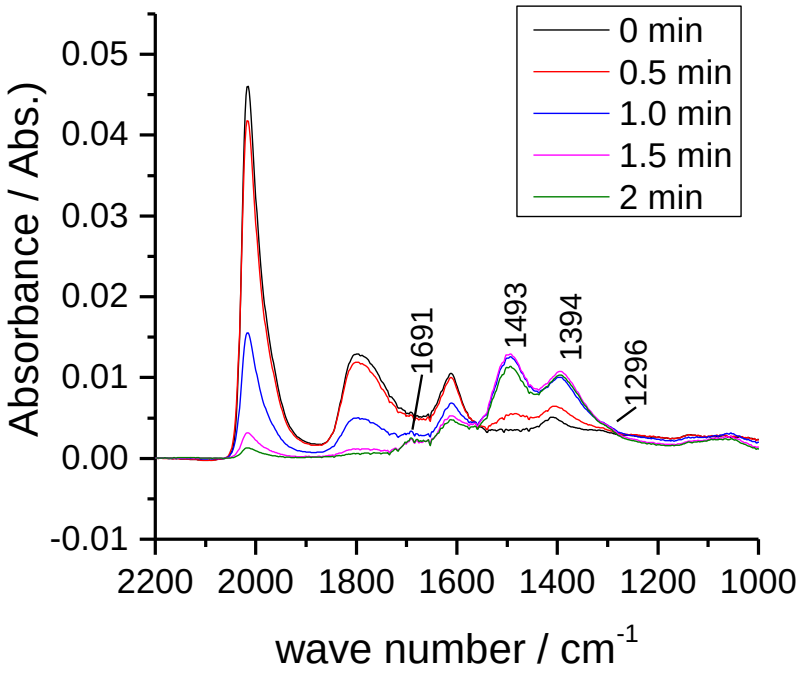

Figure A. 3. ATR-IR spectra of catalyst collected during the first 2 min of 1st O_2 flow period during APR of glycerol

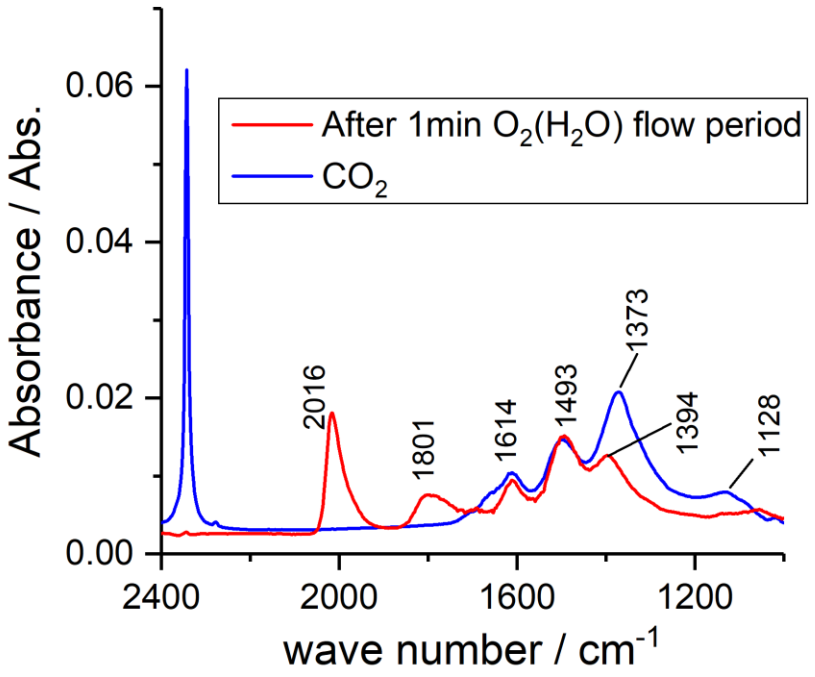

Figure A. 4. ATR-IR spectra of catalyst collected at 1 min of 1st O_2 flow period during APR of glycerol versus spectra collected $CO_2(H_2O)$ flowed over the Pt/γ-Al_2O_3 catalyst bed

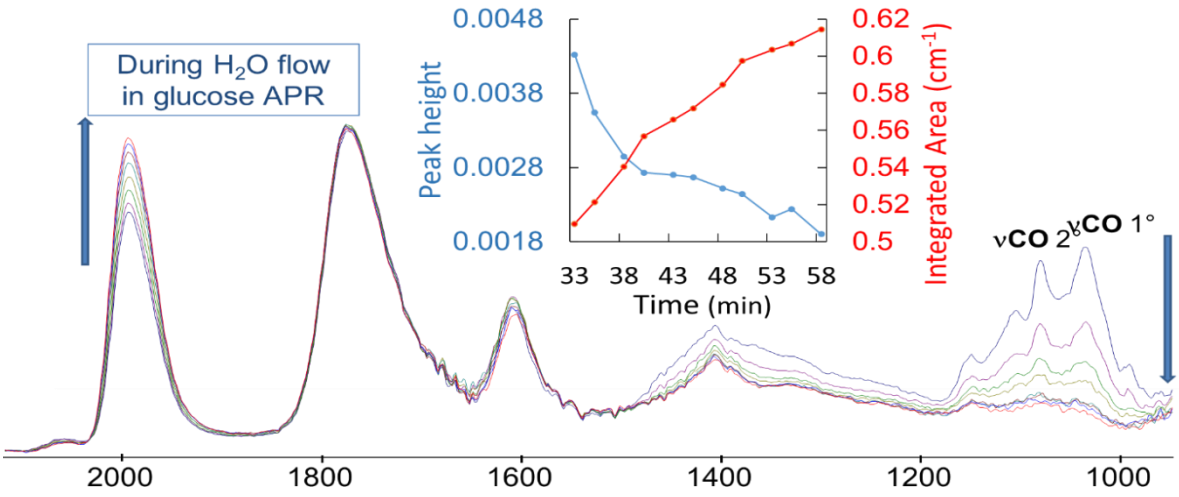

Figure A. 5. IR spectra taken during IR spectra taken during. 1st H_2O flow period after 1st aqueous glucose flow period over the catalyst (Pt/γ-Al_2O_3) bed

Table A. 1. The peak frequency of CO_L and CO_B at the start and end of aqueous reactant flow period.

	Temperature (°C)	CO_L/ cm^{-1}			CO_B/ cm^{-1}		
		1/2 (min)	30 (min)	Δ/cm^{-1}	1/2 (min)	30 (min)	Δ/cm^{-1}
Glycerol	24	2004	2015	11	1775	1802	27
	50	2008	2017	9	1771	1791	20
	72	2011	2020	9	1774	1804	30
Sorbitol	24	1998	2007	9	1771	1777	6
	50	2001	2010	9	1771	1780	9
	72	2005	2014	9	1772	1793	21
Glucose	24	1982	1994	12	1745	1770	25
	50	1998	2007	9	1765	1780	15
	72	2000	2019	19	1773	1804	31

Appendix B: Supplementary Information for Chapter 3

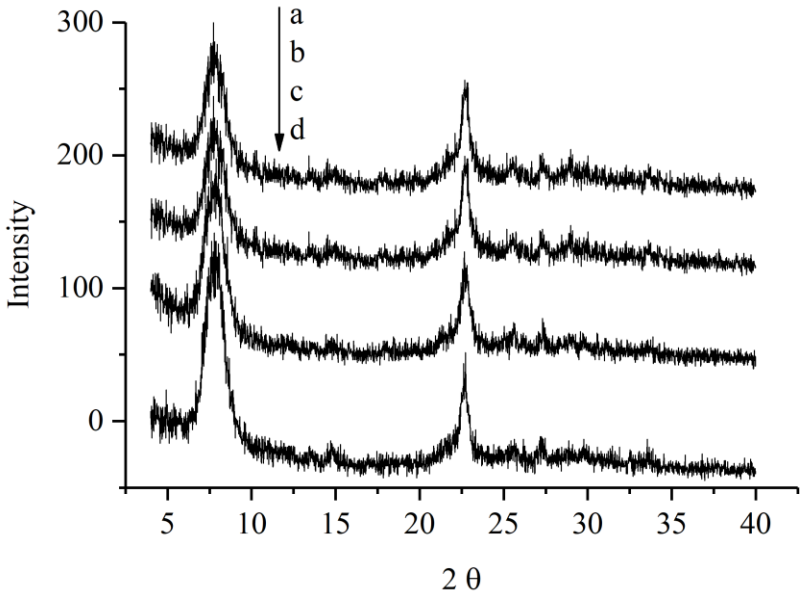

Figure B. 1. XRD of series of dealuminated beta zeolites (a) dealuminated BEA (b) W BEA (c) Mo BEA (d) Sn BEA

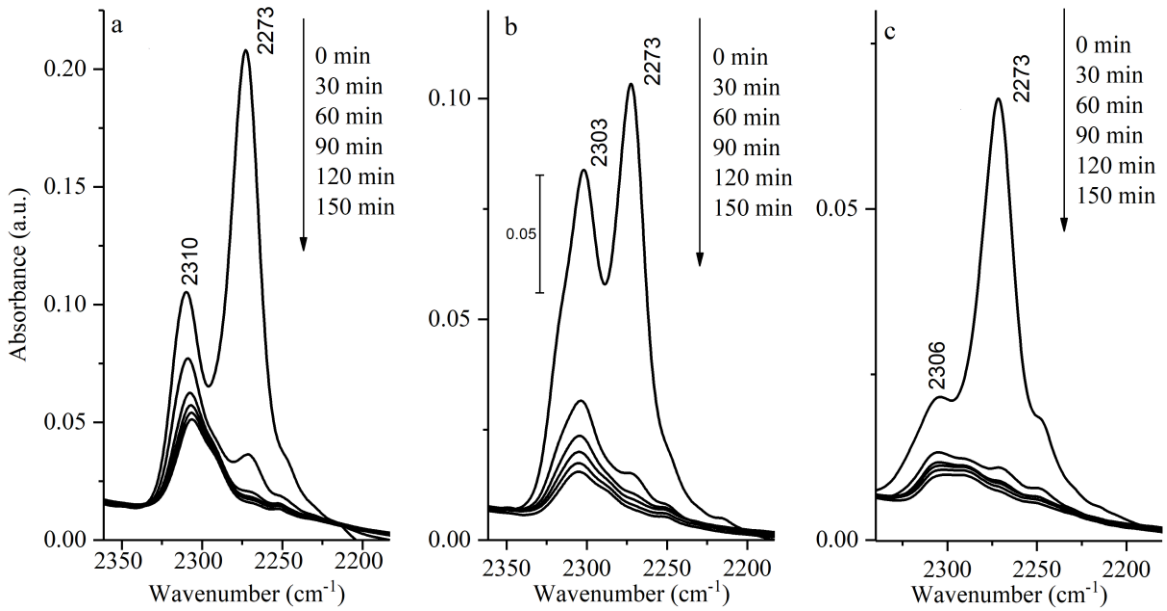

Figure B. 1. FT-IR of deuterated acetonitrile desorbing from (a) Sn BEA (b) Mo BEA (c) (b) W BEA

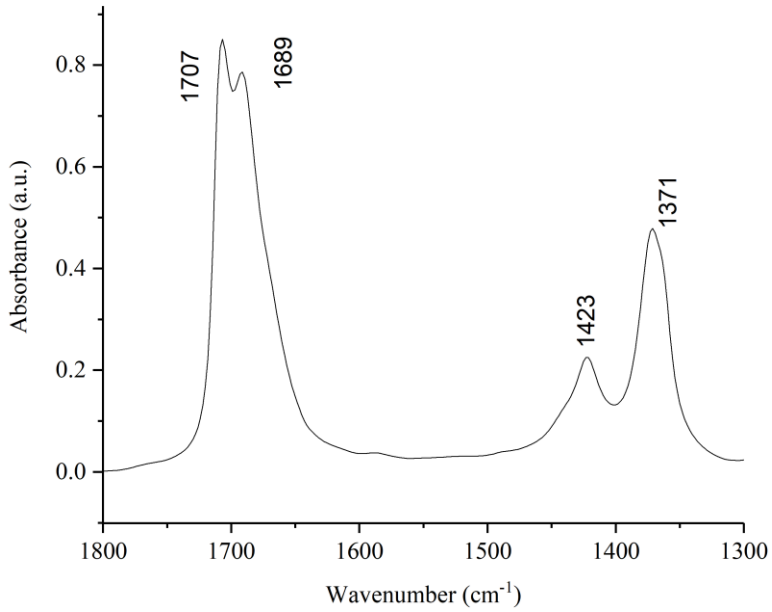

Figure B. 2. FT-IR spectra of adsorption of acetone on dealuminated BEA at the saturation of 0.1 mbar of acetone

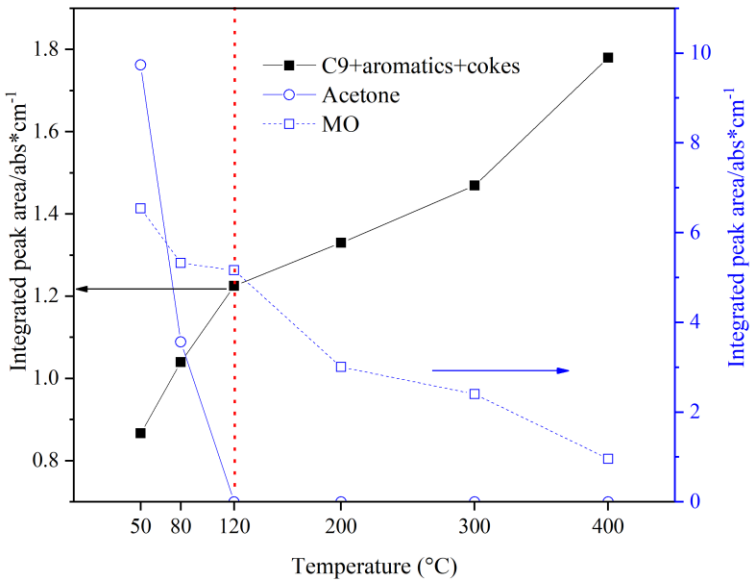

Figure B. 3. FT-IR Variation of the integrated absorbance of surface species formed from adsorbed acetone on Sn BEA during increasing temperatures

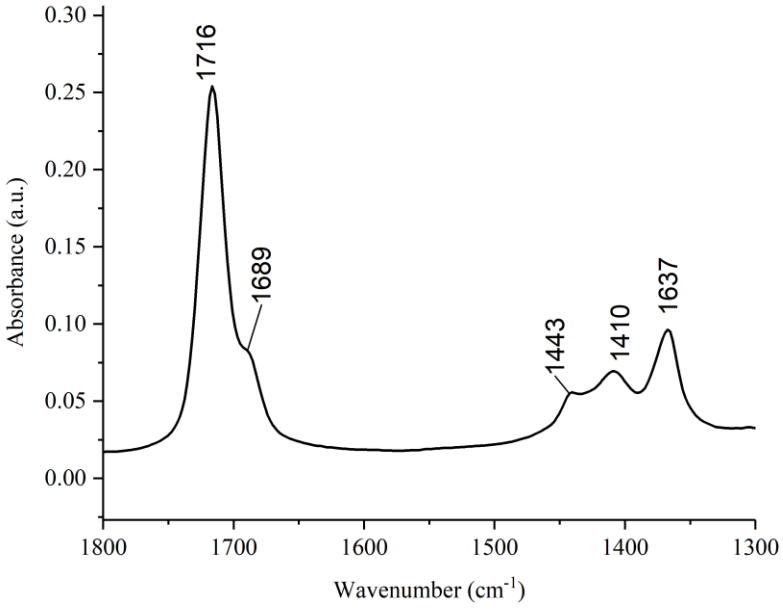

Figure B. 4. FT-IR spectra of adsorption of acetone on dealuminated BEA at the saturation of 0.1 mbar of hydroxyacetone

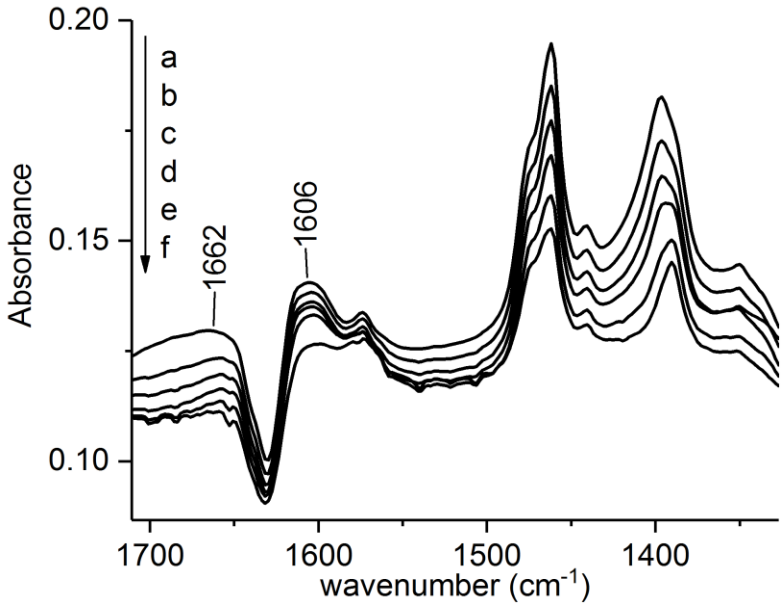

Figure B. 5. FT-IR spectra of adsorbed 1-propanol on Sn BEA at (a) 50 °C HV (b) 80 °C (c) 120 °C HV (d) 200 °C HV (e) 300 °C HV (f) 400 °C HV

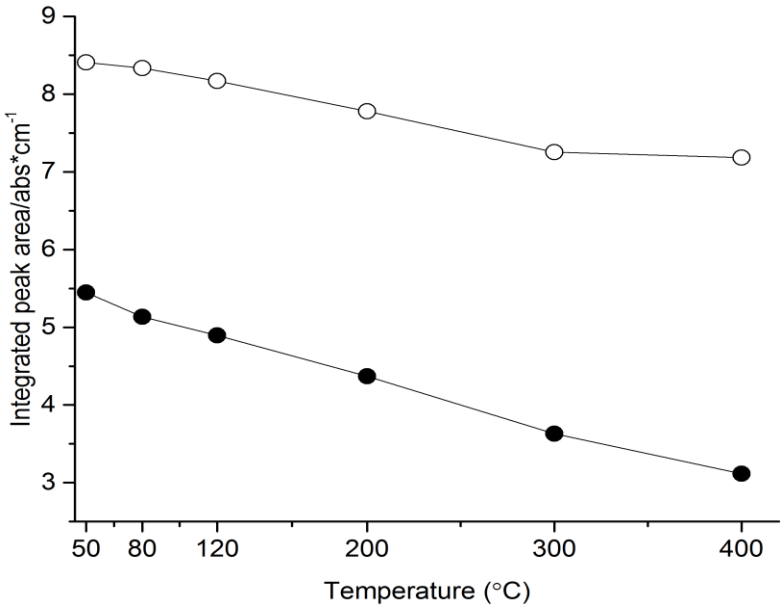

Figure B. 6. FT-IR Variation of the integrated absorbance of νC=O of hydroxyacetone (●) and 2-hydroxypropanal(○) adsorbed on Sn BEA during increasing temperatures

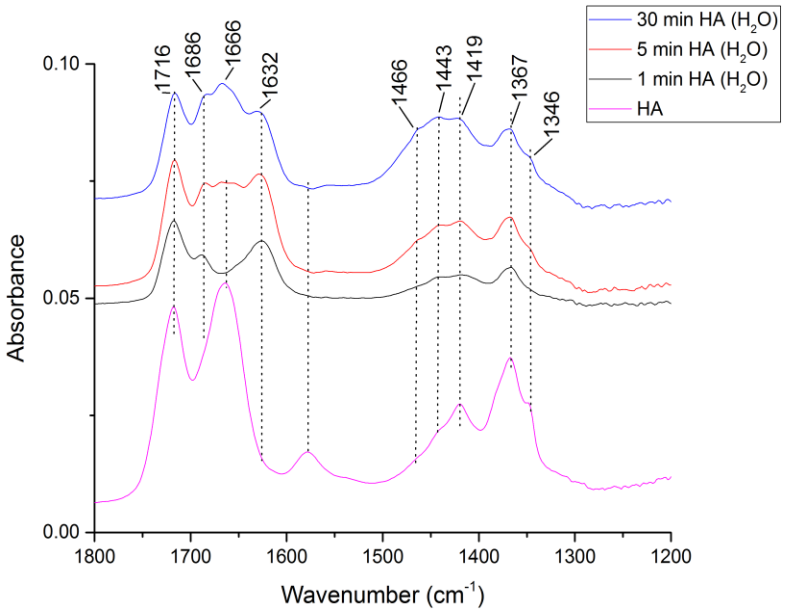

Figure B. 7. FT-IR spectrum of evolution of adsorbed hydroxyacetone on Sn BEA in the presence of 1 mbar of H_2O vapor

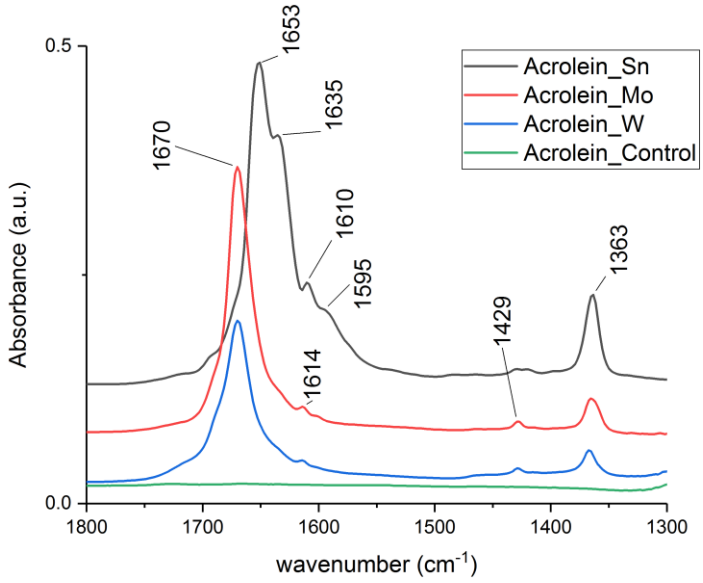

Figure B. 8. FT-IR spectrum of adsorbed of acrolein on (a) Sn BEA, (b) Mo BEA, (c) W BEA, and (d) dealuminated BEA

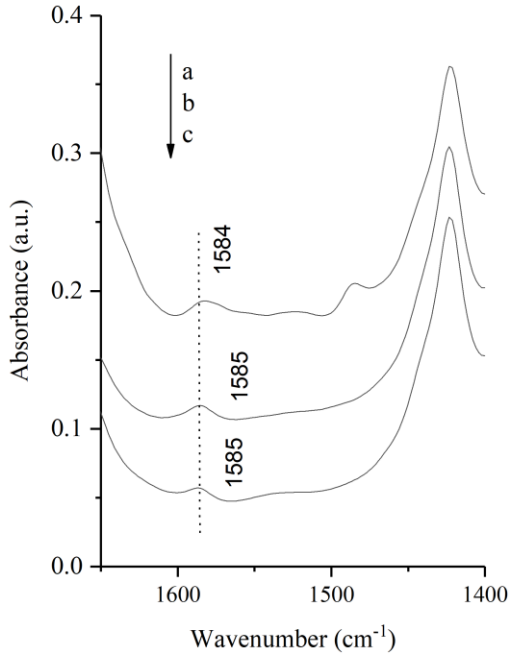

Figure B. 9. FT-IR spectra of Sn, Mo and W BEA subject to 0.1 mbar of acetone for 1 hr before desorption

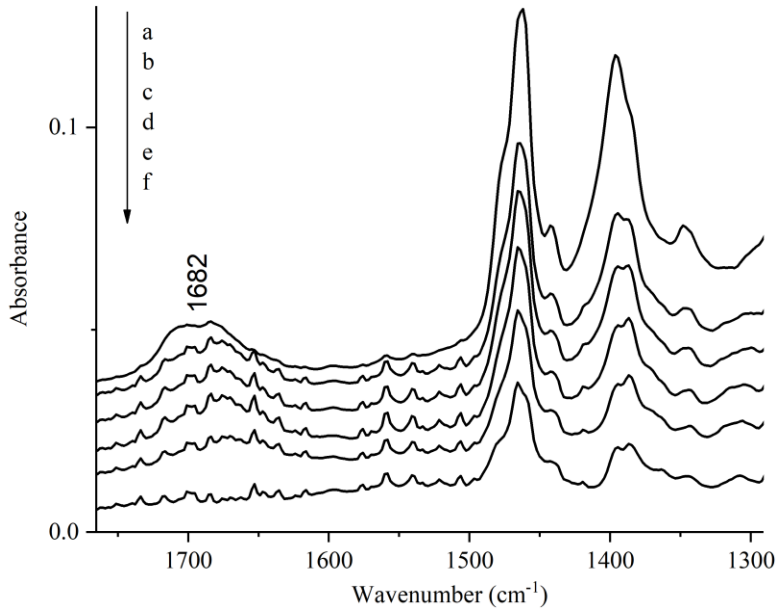

Figure B. 10. FT-IR spectra of adsorbed 1-propanol on Mo BEA at (a) 50 °C HV (b) 80 °C (c) 120 °C HV (d) 200 °C HV (e) 300 °C HV (f) 400 °C HV

Table B. 1. Values of Mulliken Electronegativity, Hardness and Ionic radius

Sample	Mulliken Electro-negativity (eV)	Hardness (eV)	Ionic radius (Å)
Sn BEA	415	294	0.55
Mo BEA	362	290	0.42 (6+) 0.66 (4+)
W BEA	424	345	0.41 (6+) 0.65 (4+)

References

1. Huber, G. W.; Iborra, S.; Corma, A., Synthesis of transportation fuels from biomass: chemistry, catalysts, and engineering. *Chemical reviews* **2006,** *106* (9), 4044-98.

2. Caratzoulas, S.; Davis, M. E.; Gorte, R. J.; Gounder, R.; Lobo, R. F.; Nikolakis, V.; Sandler, S. I.; Snyder, M. A.; Tsapatsis, M.; Vlachos, D. G., Challenges of and Insights into Acid-Catalyzed Transformations of Sugars. *The Journal of Physical Chemistry C* **2014,** *118* (40), 22815-22833.

3. Perlack, R. D.; Wright, L. L.; Turhollow, A.; Graham, R. L.; Stokes, B.; Erbach, D. C., Biomass as Feedstock for a Bioenergy and Bioproducts Industry: The Technical

Feasibility of a Billion-Ton Annual Supply. DOE, Ed. Oak Ridge National Laboratory: Oak Ridge, TN, 2005.

4. Huber, G. W.; Dumesic, J. A., An overview of aqueous-phase catalytic processes for production of hydrogen and alkanes in a biorefinery. *Catalysis Today* **2006,** *111* (1-2), 119-132.

5. Lin, Y.-C.; Huber, G. W., The critical role of heterogeneous catalysis in lignocellulosic biomass conversion. *Energy Environ. Sci.* **2009,** *2* (1), 68-80.

6. Hill, J.; Nelson, E.; Tilman, D.; Polasky, S.; Tiffany, D., Environmental, economic, and energetic costs and benefits of biodiesel and ethanol biofuels. *Proceedings of the National Academy of Sciences of the United States of America* **2006,** *103* (30), 11206-10.

7. Evans, R. J.; Milne, T. A.; Soltys, M. N., Direct mass-spectrometric studies of the pyrolysis of carbonaceous fuels. *J Anal Appl Pyrol* **1986,** *9* (3), 207-236.

8. Chheda, J. N.; Huber, G. W.; Dumesic, J. A., Liquid-phase catalytic processing of biomass-derived oxygenated hydrocarbons to fuels and chemicals. *Angewandte Chemie* **2007,** *46* (38), 7164-83.

9. Werpy, T.; Petersen, G.; Aden, A.; Bozell, J.; Holladay, J.; White, J.; Manheim, A., Top Value Added Chemicals From Biomass: Volume 1—Results of Screening for Potential

Candidates from Sugars and Synthesis Gas. DOE, Ed. Golden, 2004; Vol. 1, pp 1-76.

10. Foster, A. J.; Lobo, R. F., Identifying reaction intermediates and catalytic active sites through in situ characterization techniques. *Chemical Society reviews* **2010,** *39* (12), 4783-93.

11. Andanson, J.-M.; Baiker, A., Exploring catalytic solid/liquid interfaces by in situ attenuated total reflection infrared spectroscopy. *Chemical Society reviews* **2010,** *39* (12), 4571-4584.

12. Foo, G. S.; Wei, D.; Sholl, D. S.; Sievers, C., Role of Lewis and Brønsted Acid Sites in the Dehydration of Glycerol over Niobia. *ACS Catalysis* **2014,** *4* (9), 3180-3192.

13. Copeland, J. R.; Foo, G. S.; Harrison, L. A.; Sievers, C., In situ ATR-IR study on aqueous phase reforming reactions of glycerol over a Pt/γ-Al_2O_3 catalyst. *Catalysis Today* **2013,** *205*, 49-59.

14. Roy, S.; Bakhmutsky, K.; Mahmoud, E.; Lobo, R. F.; Gorte, R. J., Probing Lewis Acid Sites in Sn-Beta Zeolite. *ACS Catalysis* **2013,** *3* (4), 573-580.

15. Mojet, B. L.; Ebbesen, S. D.; Lefferts, L., Light at the interface: the potential of attenuated total reflection infrared spectroscopy for understanding heterogeneous catalysis in water. *Chemical Society reviews* **2010,** *39* (12), 4643-55.

16. Ferri, D.; Baiker, A., Advances in Infrared Spectroscopy of Catalytic Solid–Liquid Interfaces: The Case of Selective Alcohol Oxidation. *Topics in Catalysis* **2009,** *52* (10), 1323-1333.

17. Ortiz-Hernandez, I.; Williams, C. T., In Situ Investigation of Solid−Liquid Catalytic Interfaces by Attenuated Total Reflection Infrared Spectroscopy. *Langmuir : the ACS journal of surfaces and colloids* **2003,** *19* (7), 2956-2962.

18. He, R.; Davda, R. R.; Dumesic, J. A., In situ ATR-IR spectroscopic and reaction kinetics studies of water-gas shift and methanol reforming on Pt/Al_2O_3 catalysts in vapor and liquid phases. *J Phys Chem B* **2005,** *109* (7), 2810-20.

19. Schmidt, L. D.; Dauenhauer, P. J., Chemical engineering: hybrid routes to biofuels. *Nature* **2007,** *447* (7147), 914-5.

20. Shabaker, J., Aqueous-phase reforming of methanol and ethylene glycol over alumina-supported platinum catalysts. *Journal of Catalysis* **2003,** *215* (2), 344-352.

21. Huber, G. W.; Shabaker, J. W.; Dumesic, J. A., Raney Ni-Sn catalyst for H_2 production from biomass-derived hydrocarbons. *Science* **2003,** *300* (5628), 2075-7.

22. Davda, R. R.; Shabaker, J. W.; Huber, G. W.; Cortright, R. D.; Dumesic, J. A., Aqueous-phase reforming of ethylene glycol on silica-supported metal catalysts. *Applied Catalysis B: Environmental* **2003,** *43* (1), 13-26.

23. Davda, R. R.; Dumesic, J. A., Renewable hydrogen by aqueous-phase reforming of glucose. *Chemical communications* **2004,** (1), 36-7.

24. Davda, R. R.; Shabaker, J. W.; Huber, G. W.; Cortright, R. D.; Dumesic, J. A., A review of catalytic issues and process conditions for renewable hydrogen and alkanes by aqueous-phase reforming of oxygenated hydrocarbons over supported metal catalysts. *Applied Catalysis B: Environmental* **2005,** *56* (1-2), 171-186.

25. Cortright, R. D.; Davda, R. R.; Dumesic, J. A., Hydrogen from catalytic reforming of biomass-derived hydrocarbons in liquid water. *Nature* **2002,** *418* (6901), 964-7.

26. Li, N.; Huber, G. W., Aqueous-phase hydrodeoxygenation of sorbitol with Pt/SiO_2–Al_2O_3: Identification of reaction intermediates. *Journal of Catalysis* **2010,** *270* (1), 48-59.

27. Wawrzetz, A.; Peng, B.; Hrabar, A.; Jentys, A.; Lemonidou, A. A.; Lercher, J. A., Towards understanding the bifunctional hydrodeoxygenation and aqueous phase reforming of glycerol. *Journal of Catalysis* **2010,** *269* (2), 411-420.

28. Gu, X.-K.; Liu, B.; Greeley, J., First-Principles Study of Structure Sensitivity of Ethylene Glycol Conversion on Platinum. *ACS Catalysis* **2015,** *5* (4), 2623-2631.

29. Shabaker, J. W.; Huber, G. W.; Dumesic, J. A., Aqueous-phase reforming of oxygenated hydrocarbons over Sn-modified Ni catalysts. *Journal of Catalysis* **2004,** *222* (1), 180-191.

30. Shabaker, J. W.; Huber, G. W.; Davda, R. R.; Cortright, R. D.; Dumesic, J. A., Aqueous-Phase Reforming of Ethylene Glycol Over Supported Platinum Catalysts. *Catalysis Letters* **2003,** *88* (1), 1-8.

31. Luo, N.; Fu, X.; Cao, F.; Xiao, T.; Edwards, P. P., Glycerol aqueous phase reforming for hydrogen generation over Pt catalyst – Effect of catalyst composition and reaction conditions. *Fuel* **2008,** *87* (17-18), 3483-3489.

32. Campbell, C. T.; Ertl, G.; Kuipers, H.; Segner, J., A molecular beam study of the catalytic oxidation of CO on a Pt(111) surface. *The Journal of Chemical Physics* **1980,** *73* (11), 5862-5873.

33. Stampfl, C.; Scheffler, M., Anomalous Behavior of Ru for Catalytic Oxidation: A Theoretical Study of the Catalytic ReactionCO+12O2→CO2. *Physical Review Letters* **1997,** *78* (8), 1500-1503.

34. Wovchko, E. A.; Yates, J. T., Activation of O_2 on a Photochemically Generated RhISite on an Al_2O_3 Surface: Low-Temperature O_2 Dissociation and CO Oxidation. *Journal of the American Chemical Society* **1998,** *120* (40), 10523-10527.

35. Bergeld, J.; Kasemo, B.; Chakarov, D. V., CO oxidation on Pt(111) promoted by coadsorbed H2O. *Surface Science* **2001,** *495* (3), L815-L820.

36. Hendriksen, B. L. M.; Frenken, J. W. M., CO oxidation on Pt(110): Scanning tunneling microscopy inside a high-pressure flow reactor. *Physical Review Letters* **2002,** *89* (4).

37. Alavi, A.; Hu, P.; Deutsch, T.; Silvestrelli, P. L.; Hutter, J., CO Oxidation on Pt(111): AnAb InitioDensity Functional Theory Study. *Physical Review Letters* **1998,** *80* (16), 3650-3653.

38. Akerlund, C.; Zoric, I.; Kasemo, B., A collision induced reaction: CO_2 production on O_2 and CO covered Pt(111). *Journal of Chemical Physics* **1996,** *104* (18), 7359-7362.

39. Mhadeshwar, A. B.; Vlachos, D. G., Microkinetic Modeling for Water-Promoted CO Oxidation, Water−Gas Shift, and Preferential Oxidation of CO on Pt. *The Journal of Physical Chemistry B* **2004,** *108* (39), 15246-15258.

40. Gong, X.-Q.; Hu, P.; Raval, R., The catalytic role of water in CO oxidation. *The Journal of Chemical Physics* **2003,** *119* (12), 6324-6334.

41. Sievers, C.; Noda, Y.; Qi, L.; Albuquerque, E. M.; Rioux, R. M.; Scott, S. L., Phenomena Affecting Catalytic Reactions at Solid–Liquid Interfaces. *ACS Catalysis* **2016,** *6* (12), 8286-8307.

42. Ebbesen, S. D.; Mojet, B. L.; Lefferts, L., The influence of water and pH on adsorption and oxidation of CO on Pd/Al_2O_3—an investigation by attenuated total reflection infrared spectroscopy. *Phys. Chem. Chem. Phys.* **2009,** *11* (4), 641-649.

43. Ebbesen, S. D.; Mojet, B. L.; Lefferts, L., In situ ATR-IR study of CO adsorption and oxidation over Pt/Al_2O_3 in gas and aqueous phase: Promotion effects by water and pH. *Journal of Catalysis* **2007,** *246* (1), 66-73.

44. Rasko, J.; Kiss, J., Adsorption and surface reactions of acetaldehyde on alumina-supported noble metal catalysts. *Catalysis Letters* **2005,** *101* (1-2), 71-77.

45. Silva, A. M.; Costa, L. O. O.; Barandas, A. P. M. G.; Borges, L. E. P.; Mattos, L. V.; Noronha, F. B., Effect of the metal nature on the reaction mechanism of the partial oxidation of ethanol over CeO_2-supported Pt and Rh catalysts. *Catalysis Today* **2008,** *133-135*, 755-761.

46. El-Maazawi, M.; Finken, A. N.; Nair, A. B.; Grassian, V. H., Adsorption and Photocatalytic Oxidation of Acetone on TiO_2: An in Situ Transmission FT-IR Study. *Journal of Catalysis* **2000,** *191* (1), 138-146.

47. Takanabe, K.; Aika, K.; Seshan, K.; Lefferts, L., Sustainable hydrogen from bio-oil—Steam reforming of acetic acid as a model oxygenate. *Journal of Catalysis* **2004,** *227* (1), 101-108.

48. Yee, A.; Morrison, S. J.; Idriss, H., A Study of the Reactions of Ethanol on CeO_2 and Pd/CeO_2 by Steady State Reactions, Temperature Programmed Desorption, and In Situ FT-IR. *Journal of Catalysis* **1999,** *186* (2), 279-295.

49. Copeland, J. R.; Shi, X. R.; Sholl, D. S.; Sievers, C., Surface interactions of C and C(3) polyols with gamma-Al_2O_3 and the role of coadsorbed water. *Langmuir : the ACS journal of surfaces and colloids* **2013,** *29* (2), 581-93.

50. Copeland, J. R.; Santillan, I. A.; Schimming, S. M.; Ewbank, J. L.; Sievers, C., Surface Interactions of Glycerol with Acidic and Basic Metal Oxides. *The Journal of Physical Chemistry C* **2013,** *117* (41), 21413-21425.

51. Zope, B. N.; Davis, R. J., Inhibition of gold and platinum catalysts by reactive intermediates produced in the selective oxidation of alcohols in liquid water. *Green Chemistry* **2011,** *13* (12), 3484-3491.

52. Brunauer, S.; Emmett, P. H.; Teller, E., Adsorption of Gases in Multimolecular Layers. *Journal of the American Chemical Society* **1938,** *60* (2), 309-319.

53. Barrett, E. P.; Joyner, L. G.; Halenda, P. P., The Determination of Pore Volume and Area Distributions in Porous Substances. I. Computations from Nitrogen Isotherms. *Journal of the American Chemical Society* **1951,** *73* (1), 373-380.

54. Datka, J.; Turek, A. M.; Jehng, J. M.; Wachs, I. E., Acidic Properties of Supported Niobium Oxide Catalysts - an Infrared-Spectroscopy Investigation. *J. Catal.* **1992,** *135* (1), 186-199.

55. Wefers, K.; Misra, C., *Oxides and hydroxides of aluminum*. 2 ed.; Alcoa Research Laboratories: 1987; p 92.

56. Holleman, A. F.; Wiberg, E., *Inorganic Chemistry*. 34 ed.; Academic Press: Berlin, 2001; p 1884.

57. Zaki, M. I.; Hasan, M. A.; Al-Sagheer, F. A.; Pasupulety, L., In situ FTIR spectra of pyridine adsorbed on SiO_2–Al_2O_3, TiO_2, ZrO_2 and CeO_2: general considerations for the identification of acid sites on surfaces of finely divided metal oxides. *Colloids and Surfaces A: Physicochemical and Engineering Aspects* **2001,** *190* (3), 261-274.

58. Bourane, A.; Dulaurent, O.; Bianchi, D., Heats of Adsorption of Linear and Multibound Adsorbed CO Species on a Pt/Al_2O_3 Catalyst Using in Situ Infrared Spectroscopy under Adsorption Equilibrium. *Journal of Catalysis* **2000,** *196* (1), 115-125.

59. Colthup, N. B.; Daly, L. H.; Wiberley, S. E., *Introduction to Infrared and Raman Spectroscopy*. Academic Press: 1990; p 547.

60. McManus, J. R.; Salciccioli, M.; Yu, W.; Vlachos, D. G.; Chen, J. G.; Vohs, J. M., Correlating the Surface Chemistry of C2 and C3 Aldoses with a C6 Sugar: Reaction of

Glucose, Glyceraldehyde, and Glycolaldehyde on Pd(111). *The Journal of Physical Chemistry C* **2012,** *116* (35), 18891-18898.

61. Ravenelle, R. M.; Schüβler, F.; D'Amico, A.; Danilina, N.; van Bokhoven, J. A.; Lercher, J. A.; Jones, C. W.; Sievers, C., Stability of Zeolites in Hot Liquid Water. *The Journal of Physical Chemistry C* **2010,** *114* (46), 19582-19595.

62. Lercher, J. A., Acid-Base Properties of Al2o3-Mgo Oxides .1. Infrared Study of Adsorption of Acetone. *Zeitschrift Fur Physikalische Chemie-Wiesbaden* **1982,** *129* (2), 209-218.

63. Liu, B.; Greeley, J., Decomposition Pathways of Glycerol via C-H, O-H, and C-C Bond Scission on Pt(111): A Density Functional Theory Study. *J. Phys. Chem. C* **2011,** *115* (40), 19702-19709.

64. Bourane, A.; Derrouiche, S.; Bianchi, D., Impact of Pt dispersion on the elementary steps of CO oxidation by O2 over Pt/Al_2O_3 catalysts. *Journal of Catalysis* **2004,** *228* (2), 288-297.

65. Hanawa, H.; Kunimatsu, K.; Uchida, H.; Watanabe, M., In situ ATR-FTIR study of bulk CO oxidation on a polycrystalline Pt electrode. *Electrochimica Acta* **2009,** *54* (26), 6276-6285.

66. Kim, C. S.; Korzeniewski, C.; Tornquist, W. J., Site-Specific Coadsorption at Pt(335) as Probed by Infrared-Spectroscopy - Structural Alterations in the Co Adlayer under Aqueous Electrochemical Conditions. *Journal of Chemical Physics* **1994,** *100* (1), 628-630.

67. Trinh, Q. T.; Chethana, B. K.; Mushrif, S. H., Adsorption and Reactivity of Cellulosic Aldoses on Transition Metals. *The Journal of Physical Chemistry C* **2015,** *119* (30), 17137-17145.

68. Yu, W.; Barteau, M. A.; Chen, J. G., Glycolaldehyde as a probe molecule for biomass derivatives: reaction of C-OH and C horizontal lineO functional groups on monolayer Ni surfaces. *Journal of the American Chemical Society* **2011,** *133* (50), 20528-35.

69. Yu, W.; Barteau, M. A.; Chen, J. G., Glycolaldehyde as a Probe Molecule for Biomass Derivatives: Reaction of C—OH and C═O Functional Groups on Monolayer Ni Surfaces. *Journal of the American Chemical Society* **2011,** *133* (50), 20528-20535.

70. Pekoz, R.; Worner, S.; Ghiringhelli, L. M.; Donadio, D., Trends in the Adsorption and Dissociation of Water Clusters on Flat and Stepped Metallic Surfaces. *J. Phys. Chem. C* **2014,** *118* (51), 29990-29998.

71. Ladas, S.; Poppa, H.; Boudart, M., The adsorption and catalytic oxidation of carbon monoxide on evaporated palladium particles. *Surface Science* **1981,** *102* (1), 151-171.

72. Allian, A. D.; Takanabe, K.; Fujdala, K. L.; Hao, X.; Truex, T. J.; Cai, J.; Buda, C.; Neurock, M.; Iglesia, E., Chemisorption of CO and mechanism of CO oxidation on supported platinum nanoclusters. *Journal of the American Chemical Society* **2011,** *133* (12), 4498-517.

73. Kim, C. S.; Korzeniewski, C.; Tornquist, W. J., Site specific co-adsorption at Pt(335) as probed by infrared spectroscopy: Structural alterations in the CO adlayer under aqueous electrochemical conditions. *The Journal of Chemical Physics* **1994,** *100* (1), 628-630.

74. Bordiga, S.; Bonino, F.; Damin, A.; Lamberti, C., Reactivity of Ti(IV) species hosted in TS-1 towards H_2O_2-H_2O solutions investigated by ab initio cluster and periodic approaches combined with experimental XANES and EXAFS data: a review and new highlights. *Phys Chem Chem Phys* **2007,** *9* (35), 4854-78.

75. de Clippel, F.; Dusselier, M.; Van Rompaey, R.; Vanelderen, P.; Dijkmans, J.; Makshina, E.; Giebeler, L.; Oswald, S.; Baron, G. V.; Denayer, J. F.; Pescarmona, P. P.; Jacobs, P. A.; Sels, B. F., Fast and selective sugar conversion to alkyl lactate and lactic acid with bifunctional carbon-silica catalysts. *Journal of the American Chemical Society* **2012,** *134* (24), 10089-101.

76. Lewis, J. D.; Van de Vyver, S.; Crisci, A. J.; Gunther, W. R.; Michaelis, V. K.; Griffin, R. G.; Roman-Leshkov, Y., A continuous flow strategy for the coupled transfer hydrogenation and etherification of 5-(hydroxymethyl)furfural using Lewis acid zeolites. *ChemSusChem* **2014,** *7* (8), 2255-65.

77. Corma, A.; Renz, M., A general method for the preparation of ethers using water-resistant solid lewis acids. *Angewandte Chemie* **2007,** *46* (1-2), 298-300.

78. Jae, J.; Mahmoud, E.; Lobo, R. F.; Vlachos, D. G., Cascade of Liquid-Phase Catalytic Transfer Hydrogenation and Etherification of 5-Hydroxymethylfurfural to Potential Biodiesel Components over Lewis Acid Zeolites. *Chemcatchem* **2014,** *6* (2), 508-513.

79. Corma, A.; Nemeth, L. T.; Renz, M.; Valencia, S., Sn-zeolite beta as a heterogeneous chemoselective catalyst for Baeyer-Villiger oxidations. *Nature* **2001,** *412* (6845), 423-5.

80. Renz, M.; Blasco, T.; Corma, A.; Fornes, V.; Jensen, R.; Nemeth, L., Selective and shape-selective Baeyer-Villiger oxidations of aromatic aldehydes and cyclic ketones with Sn-beta zeolites and H2O2. *Chemistry* **2002,** *8* (20), 4708-17.

81. Hammond, C.; Conrad, S.; Hermans, I., Simple and scalable preparation of highly active Lewis acidic Sn-beta. *Angewandte Chemie* **2012,** *51* (47), 11736-9.

82. Moliner, M.; Roman-Leshkov, Y.; Davis, M. E., Tin-containing zeolites are highly active catalysts for the isomerization of glucose in water. *Proceedings of the National Academy of Sciences of the United States of America* **2010,** *107* (14), 6164-8.

83. Gunther, W. R.; Wang, Y.; Ji, Y.; Michaelis, V. K.; Hunt, S. T.; Griffin, R. G.; Roman-Leshkov, Y., Sn-Beta zeolites with borate salts catalyse the epimerization of carbohydrates via an intramolecular carbon shift. *Nature communications* **2012,** *3,* 1109.

84. Bermejo-Deval, R.; Orazov, M.; Gounder, R.; Hwang, S.-J.; Davis, M. E., Active Sites in Sn-Beta for Glucose Isomerization to Fructose and Epimerization to Mannose. *ACS Catalysis* **2014,** *4* (7), 2288-2297.

85. Bermejo-Deval, R.; Assary, R. S.; Nikolla, E.; Moliner, M.; Roman-Leshkov, Y.; Hwang, S. J.; Palsdottir, A.; Silverman, D.; Lobo, R. F.; Curtiss, L. A.; Davis, M. E., Metalloenzyme-like catalyzed isomerizations of sugars by Lewis acid zeolites. *Proceedings of the National Academy of Sciences of the United States of America* **2012,** *109* (25), 9727-32.

86. Choudhary, V.; Caratzoulas, S.; Vlachos, D. G., Insights into the isomerization of xylose to xylulose and lyxose by a Lewis acid catalyst. *Carbohydr Res* **2013,** *368* (Supplement C), 89-95.

87. Van de Vyver, S.; Odermatt, C.; Romero, K.; Prasomsri, T.; Román-Leshkov, Y., Solid Lewis Acids Catalyze the Carbon–Carbon Coupling between Carbohydrates and Formaldehyde. *ACS Catalysis* **2015,** *5* (2), 972-977.

88. Pacheco, J. J.; Davis, M. E., Synthesis of terephthalic acid via Diels-Alder reactions with ethylene and oxidized variants of 5-hydroxymethylfurfural. *Proceedings of the National Academy of Sciences of the United States of America* **2014,** *111* (23), 8363-7.

89. Dusselier, M.; Van Wouwe, P.; De Smet, S.; De Clercq, R.; Verbelen, L.; Van Puyvelde, P.; Du Prez, F. E.; Sels, B. F., Toward Functional Polyester Building Blocks from Renewable Glycolaldehyde with Sn Cascade Catalysis. *ACS Catalysis* **2013,** *3* (8), 1786-1800.

90. Wang, Y.; Lewis, J. D.; Román-Leshkov, Y., Synthesis of Itaconic Acid Ester Analogues via Self-Aldol Condensation of Ethyl Pyruvate Catalyzed by Hafnium BEA Zeolites. *ACS Catalysis* **2016,** *6* (5), 2739-2744.

91. Van de Vyver, S.; Román-Leshkov, Y., Metalloenzymartige Zeolithe als Lewis-Säure-Katalysatoren für die C-C-Bindungsbildung. *Angewandte Chemie* **2015,** *127* (43), 12736-12744.

92. Müller, P.; Wolf, P.; Hermans, I., Insights into the Complexity of Heterogeneous Liquid-Phase Catalysis: Case Study on the Cyclization of Citronellal. *ACS Catalysis* **2016,** *6* (5), 2760-2769.

93. Taarning, E.; Saravanamurugan, S.; Holm, M. S.; Xiong, J.; West, R. M.; Christensen, C. H., Zeolite-catalyzed isomerization of triose sugars. *ChemSusChem* **2009,** *2* (7), 625-7.

94. Holm, M. S.; Saravanamurugan, S.; Taarning, E., Conversion of sugars to lactic acid derivatives using heterogeneous zeotype catalysts. *Science* **2010,** *328* (5978), 602-5.

95. Holm, M. S.; Pagán-Torres, Y. J.; Saravanamurugan, S.; Riisager, A.; Dumesic, J. A.; Taarning, E., Sn-Beta catalysed conversion of hemicellulosic sugars. *Green Chemistry* **2012,** *14* (3), 702-706.

96. Boronat, M.; Concepcion, P.; Corma, A.; Renz, M.; Valencia, S., Determination of the catalytically active oxidation Lewis acid sites in Sn-beta zeolites, and their optimisation by the combination of theoretical and experimental studies. *Journal of Catalysis* **2005,** *234* (1), 111-118.

97. Boronat, M.; Corma, A.; Renz, M., Mechanism of the Meerwein-Ponndorf-Verley-Oppenauer (MPVO) redox equilibrium on Sn- and Zr-beta zeolite catalysts. *J Phys Chem B* **2006,** *110* (42), 21168-74.

98. Gorte, R. J.; White, D., Interactions of chemical species with acid sites in zeolites. *Topics in Catalysis* **1997,** *4* (1/2), 57-69.

99. Gorte, R. J., What do we know about the acidity of solid acids? *Catalysis Letters* **1999,** *62* (1), 1-13.

100. Tang, B.; Dai, W.; Wu, G.; Guan, N.; Li, L.; Hunger, M., Improved Postsynthesis Strategy to Sn-Beta Zeolites as Lewis Acid Catalysts for the Ring-Opening Hydration of Epoxides. *ACS Catalysis* **2014,** *4* (8), 2801-2810.

101. de la Torre, O.; Renz, M.; Corma, A., Biomass to chemicals: Rearrangement of β-pinene epoxide into myrtanal with well-defined single-site substituted molecular sieves as reusable solid Lewis-acid catalysts. *Appl Catal A Gen* **2010,** *380* (1-2), 165-171.

102. Corma, A.; Xamena, F. X. L. I.; Prestipino, C.; Renz, M.; Valencia, S., Water Resistant, Catalytically Active Nb and Ta Isolated Lewis Acid Sites, Homogeneously Distributed by Direct Synthesis in a Beta Zeolite. *J. Phys. Chem. C* **2009,** *113* (26), 11306-11315.

103. Bregante, D. T.; Flaherty, D. W., Periodic Trends in Olefin Epoxidation over Group IV and V Framework-Substituted Zeolite Catalysts: A Kinetic and Spectroscopic Study. *Journal of the American Chemical Society* **2017,** *139* (20), 6888-6898.

104. Boronat, M.; Corma, A.; Renz, M.; Viruela, P. M., Predicting the activity of single isolated Lewis acid sites in solid catalysts. *Chemistry* **2006,** *12* (27), 7067-77.

105. Pearson, R. G., Hard and Soft Acids and Bases. *Journal of the American Chemical Society* **1963,** *85* (22), 3533-3539.

106. Nguyen, H.; Nikolakis, V.; Vlachos, D. G., Mechanistic Insights into Lewis Acid Metal Salt-Catalyzed Glucose Chemistry in Aqueous Solution. *ACS Catalysis* **2016,** *6* (3), 1497-1504.

107. Angyal, S. J., A short note on the epimerization of aldoses. *Carbohydrate Research* **1997,** *300* (3), 279-281.

108. Wolf, P.; Valla, M.; Nunez-Zarur, F.; Comas-Vives, A.; Rossini, A. J.; Firth, C.; Kallas, H.; Lesage, A.; Emsley, L.; Coperet, C.; Hermans, I., Correlating Synthetic Methods, Morphology, Atomic-Level Structure, and Catalytic Activity of Sn-beta Catalysts. *Acs Catalysis* **2016,** *6* (7), 4047-4063.

109. Simperler, A.; Bell, R. G.; Foster, M. D.; Gray, A. E.; Lewis, D. W.; Anderson, M. W., Probing the Acid Strength of Brønsted Acidic Zeolites with Acetonitrile: An Atomistic and Quantum Chemical Study. *The Journal of Physical Chemistry B* **2004,** *108* (22), 7152-7161.

110. Dijkmans, J.; Demol, J.; Houthoofd, K.; Huang, S.; Pontikes, Y.; Sels, B., Post-synthesis Snβ: An exploration of synthesis parameters and catalysis. *Journal of Catalysis* **2015,** *330*, 545-557.

111. Zaki, M. I.; Hasan, M. A.; Al-Sagheer, F. A.; Pasupulety, L., Surface Chemistry of Acetone on Metal Oxides: IR Observation of Acetone Adsorption and Consequent Surface Reactions on Silica−Alumina versus Silica and Alumina. *Langmuir : the ACS journal of surfaces and colloids* **2000,** *16* (2), 430-436.

112. Panov, A. G.; Fripiat, J. J., Acetone Condensation Reaction on Acid Catalysts. *Journal of Catalysis* **1998,** *178* (1), 188-197.

113. Panov, A.; Fripiat, J. J., An Infrared Spectroscopic Study of Acetone and Mesityl Oxide Adsorption on Acid Catalyst. *Langmuir : the ACS journal of surfaces and colloids* **1998,** *14* (14), 3788-3796.

114. Di Cosimo, J. I.; Apesteguía, C. R., Study of the catalyst deactivation in the base-catalyzed oligomerization of acetone. *Journal of Molecular Catalysis A: Chemical* **1998,** *130* (1-2), 177-185.

115. Hanson, B. E.; Wieserman, L. F.; Wagner, G. W.; Kaufman, R. A., Identification of acetone enolate on γ-alumina: implications for the oligomerization and polymerization of adsorbed acetone. *Langmuir : the ACS journal of surfaces and colloids* **1987,** *3* (4), 549-555.

116. Busca, G.; Lorenzelli, V., Infrared study of the reactivity of acetone and hexachloroacetone adsorbed on haematite. *Journal of the Chemical Society, Faraday Transactions 1: Physical Chemistry in Condensed Phases* **1982,** *78* (10), 2911-2919.

117. Herrmann, S.; Iglesia, E., Elementary steps in acetone condensation reactions catalyzed by aluminosilicates with diverse void structures. *Journal of Catalysis* **2017,** *346*, 134-153.

118. Zaki, M. I.; Hasan, M. A.; Al-Sagheer, F. A.; Pasupulety, L., Surface Chemistry of Acetone on Metal Oxides: IR Observation of Acetone Adsorption and Consequent Surface

Reactions on Silica−Alumina versus Silica and Alumina. *Langmuir : the ACS journal of surfaces and colloids* **2000,** *16* (2), 430-436.

119. Anton, A. B.; Avery, N. R.; Toby, B. H.; Weinberg, W. H., Adsorption of acetone both on the clean ruthenium(001) surface and on the ruthenium(001) surface modified chemically by the presence of an ordered oxygen adatom overlayer. *Journal of the American Chemical Society* **1986,** *108* (4), 684-694.

120. Palagin, D.; Sushkevich, V. L.; Ivanova, I. I., C–C Coupling Catalyzed by Zeolites: Is Enolization the Only Possible Pathway for Aldol Condensation? *The Journal of Physical Chemistry C* **2016,** *120* (41), 23566-23575.

121. Kubelková, L.; Čejka, J.; Nováková, J., Surface reactivity of ZSM-5 zeolites in interaction with ketones at ambient temperature (a FT-i.r. study). *Zeolites* **1991,** *11* (1), 48-53.

122. Xu, T.; Munson, E. J.; Haw, J. F., Toward a Systematic Chemistry of Organic-Reactions in Zeolites: in-Situ NMR-Studies of Ketones. *Journal of the American Chemical Society* **1994,** *116* (5), 1962-1972.

123. Xu, T.; Munson, E. J.; Haw, J. F., Toward a Systematic Chemistry of Organic-Reactions in Zeolites - in-Situ Nmr-Studies of Ketones. *Journal of the American Chemical Society* **1994,** *116* (5), 1962-1972.

124. Yaylayan, V. A.; Harty-Majors, S.; Ismail, A. A., Monitoring carbonyl-amine reaction and enolization of 1-hydroxy-2-propanone (Acetol) by FTIR spectroscopy. *J Agric Food Chem* **1999,** *47* (6), 2335-40.

125. Lewis, J. D.; Van de Vyver, S.; Roman-Leshkov, Y., Acid-Base Pairs in Lewis Acidic Zeolites Promote Direct Aldol Reactions by Soft Enolization. *Angewandte Chemie* **2015,** *54* (34), 9835-8.

126. Herrmann, S.; Iglesia, E., Elementary steps in acetone condensation reactions catalyzed by aluminosilicates with diverse void structures. *Journal of Catalysis* **2017,** *346* (Supplement C), 134-153.

127. Biaglow, A., A 13C NMR Study of the Condensation Chemistry of Acetone and Acetaldehyde Adsorbed at the Brønsted Acid Sites in H-ZSM-5. *Journal of Catalysis* **1995,** *151* (2), 373-384.

128. Biaglow, A. I.; Gorte, R. J.; Kokotailo, G. T.; White, D., A Probe of Brønsted Site Acidity in Zeolites: 13C Chemical Shift of Acetone. *Journal of Catalysis* **1994,** *148* (2), 779-786.

129. Roman-Leshkov, Y.; Moliner, M.; Labinger, J. A.; Davis, M. E., Mechanism of glucose isomerization using a solid Lewis acid catalyst in water. *Angewandte Chemie* **2010,** *49* (47), 8954-7.

130. Li, L.; Stroobants, C.; Lin, K.; Jacobs, P. A.; Sels, B. F.; Pescarmona, P. P., Selective conversion of trioses to lactates over Lewis acid heterogeneous catalysts. *Green Chemistry* **2011,** *13* (5), 1175-1181.

131. Hayashi, Y.; Sasaki, Y., Tin-catalyzed conversion of trioses to alkyl lactates in alcohol solution. *Chemical communications* **2005,** (21), 2716-8.

132. Sun, J.; So, S.; da Silva, G., The gas phase aldose-ketone isomerization mechanism: Direct interconversion of the model hydroxycarbonyls 2-hydroxypropanal and hydroxyacetone. *Int. J. Quantum Chem.* **2017,** *117* (20), 5.

133. Taarning, E.; Saravanamurugan, S.; Holm, M. S.; Xiong, J. M.; West, R. M.; Christensen, C. H., Zeolite-Catalyzed Isomerization of Triose Sugars. *ChemSusChem* **2009,** *2* (7), 625-627.

134. Hayashi, Y.; Sasaki, Y., Tin-catalyzed conversion of trioses to alkyl lactates in alcohol solution. *Chemical communications* **2005,** (21), 2716-2718.

135. Leitereg, T. J.; Cram, D. J., Studies in stereochemistry. XXXVIII. Open-chain vs. cyclic models for 1,3-asymmetric induction in addition reactions. *Journal of the American Chemical Society* **1968,** *90* (15), 4019-4026.

136. Frenking, G.; Köhler, K. F.; Reetz, M. T., On the origin of π-facial diastereoselectivity in nucleophilic additions to chiral carbonyl compounds 3. Rotational profiles of 2-methoxypropanal and 2-N,N-dimethylaminopropanal. *Tetrahedron* **1993,** *49* (19), 3971-3982.

137. Bermejo-Deval, R.; Gounder, R.; Davis, M. E., Framework and Extraframework Tin Sites in Zeolite Beta React Glucose Differently. *ACS Catalysis* **2012,** *2* (12), 2705-2713.

138. Corma, A.; Domine, M. E.; Valencia, S., Water-resistant solid Lewis acid catalysts: Meerwein–Ponndorf–Verley and Oppenauer reactions catalyzed by tin-beta zeolite. *Journal of Catalysis* **2003,** *215* (2), 294-304.

139. Gounder, R.; Davis, M. E., Monosaccharide and disaccharide isomerization over Lewis acid sites in hydrophobic and hydrophilic molecular sieves. *Journal of Catalysis* **2013,** *308*, 176-188.

140. Reichardt, C., *Solvents and Solvent Effects in Organic Chemistry*. **1988**.

141. Gutmann, V., Empirical parameters for donor and acceptor properties of solvents. *Electrochimica Acta* **1976,** *21* (9), 661-670.

142. Nakon, R.; Rechani, P. R.; Angelici, R. J., Copper(II) complex catalysis of amino acid ester hydrolysis. A correlation with complex stability. *Journal of the American Chemical Society* **1974,** *96* (7), 2117-20.

143. Zhu, Y.; Chuah, G.; Jaenicke, S., Chemo- and regioselective Meerwein–Ponndorf–Verley and Oppenauer reactions catalyzed by Al-free Zr-zeolite beta. *Journal of Catalysis* **2004,** *227* (1), 1-10.

144. Laurence, C.; Graton, J.; Gal, J.-F., An Overview of Lewis Basicity and Affinity Scales. *Journal of Chemical Education* **2011,** *88* (12), 1651-1657.

145. Li, G.; Pidko, E. A.; Hensen, E. J. M., Synergy between Lewis acid sites and hydroxyl groups for the isomerization of glucose to fructose over Sn-containing zeolites: a theoretical perspective. *Catal. Sci. Technol.* **2014,** *4* (8), 2241-2250.

146. Gunther, W. R.; Michaelis, V. K.; Griffin, R. G.; Roman-Leshkov, Y., Interrogating the Lewis Acidity of Metal Sites in Beta Zeolites with (15)N Pyridine Adsorption Coupled with MAS NMR Spectroscopy. *J Phys Chem C Nanomater Interfaces* **2016,** *120* (50), 28533-28544.

147. Zhan, C.-G.; Nichols, J. A.; Dixon, D. A., Ionization Potential, Electron Affinity, Electronegativity, Hardness, and Electron Excitation Energy: Molecular Properties from Density Functional Theory Orbital Energies. *The Journal of Physical Chemistry A* **2003,** *107* (20), 4184-4195.

148. Pearson, R. G., Absolute electronegativity and hardness: application to inorganic chemistry. *Inorganic Chemistry* **1988,** *27* (4), 734-740.

149. Ju, F.; VanderVelde, D.; Nikolla, E., Molybdenum-Based Polyoxometalates as Highly Active and Selective Catalysts for the Epimerization of Aldoses. *ACS Catalysis* **2014,** *4* (5), 1358-1364.

150. Wiberg, E.; Wiberg, N.; Holleman, A. F., *Inorganic Chemistry*. Academic Press: New York, NY., 2001.

151. Ruiz Puigdollers, A.; Schlexer, P.; Tosoni, S.; Pacchioni, G., Increasing Oxide Reducibility: The Role of Metal/Oxide Interfaces in the Formation of Oxygen Vacancies. *ACS Catalysis* **2017,** *7* (10), 6493-6513.

152. Mars, P.; van Krevelen, D. W., Oxidations carried out by means of vanadium oxide catalysts. *Chem Eng Sci* **1954,** *3*, 41-59.

153. Orazov, M.; Davis, M. E., Tandem catalysis for the production of alkyl lactates from ketohexoses at moderate temperatures. *Proceedings of the National Academy of Sciences of the United States of America* **2015,** *112* (38), 11777-82.

154. Miliordos, E.; Caratzoulas, S.; Vlachos, D. G., A periodic-DFT study of retro-aldol fragmentation of fuctose on MoO 3. *Appl Catal A Gen* **2017,** *530*, 75-82.

155. Nakamura, Y.; Murayama, T.; Ueda, W., Reduced Vanadium and Molybdenum Oxides Catalyze the Equivalent Formation of Ethane and Acetaldehyde from Ethanol. *Chemcatchem* **2014,** *6* (3), 741-744.

156. Bart, J. C. J., Near-Edge X-Ray Absorption-Spectroscopy in Catalysis. *Advances in Catalysis* **1986,** *34*, 203-296.

157. Okamoto, Y.; Oshima, N.; Kobayashi, Y.; Terasaki, O.; Kodaira, T.; Kubota, T., Structure of intrazeolite molybdenum oxide clusters and their catalysis of the oxidation of ethyl alcohol. *Phys Chem Chem Phys* **2002,** *4* (12), 2852-2862.

158. Colthup, N. B.; Daly, L. H.; Wiberley, S. E., *Introduction to Infrared and Raman spectroscopy*. Academic Press Inc.: San Diego, 1990.

159. Zhang, W.; Oyama, S. T., In SituLaser Raman Studies of Intermediates in the Catalytic Oxidation of Ethanol over Supported Molybdenum Oxide. *The Journal of Physical Chemistry* **1996,** *100* (25), 10759-10767.

160. Cheng, Z. H.; Yasukawa, A.; Kandori, K.; Ishikawa, T., FTIR Study of Adsorption of CO2on Nonstoichiometric Calcium Hydroxyapatite. *Langmuir : the ACS journal of surfaces and colloids* **1998,** *14* (23), 6681-6686.

161. Li, T.; Beidaghi, M.; Xiao, X.; Huang, L.; Hu, Z.; Sun, W.; Chen, X.; Gogotsi, Y.; Zhou, J., Ethanol reduced molybdenum trioxide for Li-ion capacitors. *Nano Energy* **2016,** *26* (Supplement C), 100-107.

162. Evans, J. C.; Bernstein, H. J., The Vibrational Spectra of Acetaldehyde and Acetaldehyde-D1. *Canadian Journal of Chemistry-Revue Canadienne De Chimie* **1956,** *34* (8), 1083-1092.

163. Siaj, M.; Reed, C.; Oyama, S. T.; Scott, S. L.; McBreen, P. H., Dissociation of acetaldehyde on beta-Mo2C to yield ethylidene and oxo surface groups: a possible pathway for active site formation in heterogeneous olefin metathesis. *Journal of the American Chemical Society* **2004,** *126* (31), 9514-5.

164. Thielemann, J. P.; Hess, C., Structure of silica-supported molybdenum oxide studied by in situ spectroscopy under reactive and non-reactive conditions. *Journal of Catalysis* **2012,** *288* (Supplement C), 124-126.

165. Prasomsri, T.; Nimmanwudipong, T.; Román-Leshkov, Y., Effective hydrodeoxygenation of biomass-derived oxygenates into unsaturated hydrocarbons by MoO3 using low H2 pressures. *Energy & Environmental Science* **2013,** *6* (6), 1732-1738.

166. Tan, S., Catalytic oxidation of olefin over oxide catalysts containing molybdenum III. Oxidation of olefin to ketone over Co3O4$z.sbnd;MoO3 and SnO2$z.sbnd;MoO3 catalysts. *Journal of Catalysis* **1970,** *17* (2), 132-142.

167. Mars, P.; van Krevelen, D. W., Oxidations carried out by means of vanadium oxide catalysts. *Chem Eng Sci* **1954,** *3* (Supplement 1), 41-59.

168. Kunimatsu, K.; Sato, T.; Uchida, H.; Watanabe, M., Role of terrace/step edge sites in CO adsorption/oxidation on a polycrystalline Pt electrode studied by in situ ATR-FTIR method. *Electrochimica Acta* **2008,** *53* (21), 6104-6110.